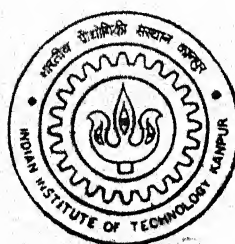


# **CORROSION BEHAVIOUR OF SINTERED METALLIC ALLOYS**

by  
**Mayadhar Debata**

TH  
MME/2009/M  
D35c



**DEPARTMENT OF MATERIALS AND METALLURGICAL ENGINEERING  
INDIAN INSTITUTE OF TECHNOLOGY KANPUR**

**November, 2000**

16 FEB 2001/MME  
CENTRAL : 150000  
I. I. T. KANPUR  
No. **A133079**



A133079



## Certificate

This is to certify that the thesis entitled “Corrosion Behaviour of Sintered Metallic Alloys ” Submitted by Mayadhar Debata(Roll No. 9820604) has been carried out under my supervision and to the best of my knowledge has not been submitted elsewhere for degree.

A handwritten signature in cursive script, followed by a horizontal line and the date "15-11-2012".

**Dr. G. S. Upadhyaya**

Professor  
Department of Materials and Metallurgical Engineering  
Indian Institute of Technology  
Kanpur, India.

## Acknowledgments

I wish to express my deep gratitude to Prof. G.S. Upadhyaya under whose guidance and supervision, the present work is carried out. His invaluable guidance and perpetual encouragement throughout the present research are deeply acknowledged.

I am thankful to Dr. Mungole and Mr. Soni for their help while needed during the experimental work.

I am grateful to my lab mates Pradyot Datta, Dhaval Rao and Ranjan for their valuable suggestions and felicity remarks in every possible step. I am also grateful to kartik, Adi, Rana, Bisu, Prabhanjan, Venumadhav, Ansuman, Biranchi, Suprem, Chandan, Santosh, Vivek, Bingo, Sisodia and Jain for maintaining a lively atmosphere in Hall-V, and also making my stay at IIT Kanpur the most memorable one.

I must acknowledge the solid support provided by my loving parents and my sisters.

At last but not the least, I extend my special thanks to all the staff of MME and ACMS, who helped me at many occasions.

**Mayadhar Debata**



# CONTENTS

	Page No.
List of Tables	i
List of Figures	iii
Abstract	vii
<b>Chapter 1 Literature Review</b>	<b>1</b>
1.1. Introduction	1
1.2. Polarization Technique and its significance	3
1.2.1. Potentiodynamic Polarization method	4
1.2.2. Characteristics of a Polarization Curve	4
1.2.3. Determination of Corrosion Rate	5
1.3. Review on the investigated alloy systems	6
1.3.1. Al- and Cu- based alloys	7
1.3.2. Ferrous alloys and Ferro-TiC	10
1.3.3. Superalloys	11
1.3.4. Boride based cermets	12
1.4. Scope of the Present Work	13
<b>Chapter 2 Experimental Procedure</b>	<b>14</b>
2.1. Details of the investigated alloys	14
2.1.1. Al- and Cu- based alloys	14
2.1.2. Ferrous alloys and Ferro-TiC	14
2.1.3. Superalloys	15
2.1.4. Boride based cermets	15
2.2. Specimen Preparation prior to Corrosion Testing	15
2.3. Electrolyte Solution Preparation	16
2.4. Potentiostat Instrument Details	16
2.5. Corrosion Testing	17
2.5.1. Anodic Polarization	17
2.5.2. Weight Loss Experiment	18
2.6. Microstructural Studies	19
2.6.1. Optical Microscopy	19
2.6.2. Scanning Electron Microscopy	19
2.7. X-Ray Diffraction Studies	19

<b>Chapter 3</b>	<b>Results</b>	<b>21</b>
3.1.	Al- and Cu- based alloys	21
3.1.1.	Corrosion in H <sub>2</sub> SO <sub>4</sub> medium	21
3.1.1.1.	Anodic Polarization studies	21
3.1.1.2.	Weight Loss Experiment	22
3.1.1.3.	X-ray diffraction Studies	22
3.1.1.4.	Optical and SEM studies	22
3.1.2.	Corrosion in 0.6N NaCl	23
3.1.2.1.	Anodic Polarization studies	23
3.1.2.2.	X-ray diffraction Studies	23
3.1.2.3.	Optical and SEM studies	23
3.2.	Ferrous alloys and Ferro-TiC	24
3.2.1.	Corrosion in H <sub>2</sub> SO <sub>4</sub> medium	24
3.2.1.1.	Anodic Polarization studies	24
3.2.1.2.	Weight Loss Experiment	24
3.2.1.3.	X-ray diffraction Studies	25
3.2.1.4.	Optical and SEM studies	25
3.2.2.	Corrosion in 0.6N NaCl	25
3.2.2.1.	Anodic Polarization studies	25
3.2.2.2.	X-ray diffraction Studies	25
3.2.2.3.	Optical and SEM studies	26
3.3.	Superalloys	26
3.3.1.	Corrosion in H <sub>2</sub> SO <sub>4</sub> medium	26
3.3.1.1.	Anodic Polarization studies	26
3.3.1.2.	Weight Loss Experiment	27
3.3.1.3.	X-ray diffraction Studies	27
3.3.1.4.	SEM studies	27
3.3.2.	Corrosion in 0.6N NaCl	27
3.3.2.1.	Anodic Polarization studies	27
3.3.2.2.	X-ray diffraction Studies	27
3.3.2.3.	SEM studies	27
3.4.	Boride based cermets	28
3.4.1.	Corrosion in H <sub>2</sub> SO <sub>4</sub> medium	28
3.4.1.1.	Anodic Polarization studies	28
3.4.1.2.	X-ray diffraction Studies	28
3.4.1.3.	Optical and SEM studies	28
3.4.2.	Corrosion in 0.6N NaCl	29

<b>Chapter 4</b>	<b>Discussion</b>	<b>30</b>
4.1.	Corrosion in H <sub>2</sub> SO <sub>4</sub> medium	30
4.1.1.	Al- and Cu- based alloys	30
4.1.2.	Ferrous alloys and Ferro-TiC	31
4.1.3.	Superalloys	32
4.1.4.	Boride based cermets	33
4.2.	Corrosion in 0.6N NaCl solution	33
4.2.1.	Al- and Cu- based alloys	34
4.2.2.	Ferrous alloys and Ferro-TiC	34
4.2.3.	Superalloys	35
4.2.4.	Boride based cermets	35
<b>Chapter 5</b>	<b>Conclusions</b>	<b>36</b>
<b>References</b>		<b>38</b>

## List of Tables

Table 1.1	Nominal Chemical Content of different Al alloys, wt. % [15].
Table 1.2	Corrosion Rate Comparison [15]. (Two Week Test)
Table 2.1	Chemical compositions and density data for Al- and Cu- based alloys.
Table 2.2	Chemical compositions of sintered ferrous alloys with density and porosity data.
Table 2.3	Chemical compositions and density data for Fe- and Ni- base superalloys.
Table 2.4	Chemical composition of the ternary boride based cermet with sintered density and porosity data.
Table 3.1	Anodic polarization characteristics of Al- and Cu- based alloys in $H_2SO_4$ medium.
Table 3.2	Results of wt. loss experiment for Al- and Cu- based alloys.
Table 3.3	Lattice parameter (nm) variation of the matrix element of as-received and corroded alloys in different media.
Table 3.4	Anodic polarization characteristics of Al- and Cu- based alloys in 0.6N NaCl solution.
Table 3.5	Anodic polarization characteristics of ferrous alloys in $H_2SO_4$ medium
Table 3.6	Results of wt. loss experiment for Tool Steels.
Table 3.7	Lattice parameter (nm) variation of the matrix element of as-received and corroded ferrous alloys in different media.

Table 3.8	Anodic polarization characteristics of ferrous alloys in 0.6N NaCl solution.
Table 3.9	Anodic polarization characteristics of the superalloys in H <sub>2</sub> SO <sub>4</sub> medium.
Table 3.10	Lattice parameter (nm) variation of the matrix element of as-received and corroded superalloys in different media.
Table 3.11	Anodic polarization characteristics of the superalloys in 0.6N NaCl solution.
Table 3.12	Anodic polarization characteristics of ternary boride based cermet in H <sub>2</sub> SO <sub>4</sub> medium.
Table 3.13	Lattice parameter (nm) of ternary boride in as-sintered and corroded conditions in 5N H <sub>2</sub> SO <sub>4</sub> .
Table 3.14	Anodic polarization characteristics of ternary boride based cermet in 0.6N NaCl.

## List of Figures

- Figure 1.1 Idealized polarization curve.
- Figure 1.2 Action of sulphuric acid of various concentrations on commercial- purity aluminium [8].
- Figure 1.3 Effect of acid concentration on the corrosion rate of iron completely immersed in aqueous solution of sulfuric acid at room temperature [19].
- Figure 2.1 Typical electrochemical polarization cell illustrating locations for working and auxiliary electrodes, and associated cell components.
- Figure 2.2 Photograph showing the electrochemical polarization cell used in the present investigation.
- Figure 3.1 Some typical anodic polarization curves of RS 7091 aluminium alloy in  $H_2SO_4$  of various concentrations.
- Figure 3.2 Some typical anodic polarization curves of DISPAL in  $H_2SO_4$  of various concentrations.
- Figure 3.3 Some typical anodic polarization curves of ODS copper in  $H_2SO_4$  of various concentrations.
- Figure 3.4 Corrosion rate variation of RS 7091 aluminium, DISPAL and ODS copper alloys with respect to  $H_2SO_4$  concentration.
- Figure 3.5 Plots obtained for RS 7091 aluminium, DISPAL and ODS copper alloys from wt. loss experiment:
- (a) wt. loss per unit area vs. exposure time
  - (b) Corrosion rate vs. exposure time
- Figure 3.6 Optical micrographs of the as-received alloys:
- (a) RS 7091 aluminium
  - (b) DISPAL
  - (c) ODS copper

- Figure 3.7 SEM micrographs of the corroded surfaces of different alloys tested in 2N  $\text{H}_2\text{SO}_4$ :
- (a)– (b) RS 7091 aluminium alloy at different magnifications
  - (c) DISPAL (d) ODS copper
- Figure 3.8 Anodic polarization curves of RS 7091 aluminium, DISPAL and ODS copper alloys in 0.6N NaCl solution.
- Figure 3.9 SEM micrographs of the corroded surfaces of alloys tested in 0.6N NaCl solution:
- (a) – (b) RS 7091 aluminium at different magnifications
  - (c) – (d) DISPAL at different magnifications
  - (e) – (f) ODS copper at different magnifications
- Figure 3.10 Some typical anodic polarization curves of Fe-0.5C steel in  $\text{H}_2\text{SO}_4$  of various concentrations.
- Figure 3.11 Some typical anodic polarization curves of Fe-5Cu-0.5C steel in  $\text{H}_2\text{SO}_4$  of various concentrations.
- Figure 3.12 Some typical anodic polarization curves of ASP 23 tool steel in  $\text{H}_2\text{SO}_4$  of various concentrations.
- Figure 3.13 Some typical anodic polarization curves of ASP 30 tool steel in  $\text{H}_2\text{SO}_4$  of various concentrations.
- Figure 3.14 Some typical anodic polarization curves of Ferro-TiC in  $\text{H}_2\text{SO}_4$  of various concentrations.
- Figure 3.15 Corrosion rate variation of different ferrous alloys with respect to  $\text{H}_2\text{SO}_4$  concentration.
- Figure 3.16 Plots obtained for ASP 23 and ASP 30 tool steels from wt. loss experiment:
- (a) wt. loss per unit area vs. exposure time
  - (b) Corrosion rate vs. exposure time

Figure 3.17 Optical micrographs of the as-received ferrous alloys:

- (a) Fe-0.5C                      (b) Fe-5Cu-0.5C      (c) ASP 23
- (d) ASP 30                      (e) Ferro-TiC

Figure 3.18 SEM micrographs of the corroded surfaces of ferrous alloys tested in 5N H<sub>2</sub>SO<sub>4</sub>:

- (a) Fe-0.5C                      (b) Fe-5Cu-0.5C
- (c) – (d) ASP 23 at different magnifications
- (e) – (f) ASP 30 at different magnifications

Figure 3.19 Anodic polarization curves of Fe-0.5C and Fe-5Cu-0.5C steels in 0.6N NaCl solution.

Figure 3.20 Anodic polarization curves of ASP 23 and ASP 30 tool steels along with Ferro-TiC in 0.6N NaCl solution.

Figure 3.21 SEM micrographs of the corroded surfaces of various alloys tested in 0.6N NaCl solution:

- (a) – (b) Fe-0.5C at different magnifications
- (c) – (d) Fe-5Cu-0.5C at different magnifications
- (e) – (f) ASP 23 at different magnifications
- (g) – (h) ASP 30 at different magnifications
- (i) Ferro-TiC

Figure 3.22 Some typical anodic polarization curves of Fe-base superalloy MA 956 in H<sub>2</sub>SO<sub>4</sub> of various concentrations.

Figure 3.23 Some typical anodic polarization curves of Ni-base superalloy MA 754 in H<sub>2</sub>SO<sub>4</sub> of various concentrations.

Figure 3.24 Corrosion rate variation of Fe- and Ni- base superalloys with respect to H<sub>2</sub>SO<sub>4</sub> concentration.



Figure 3.25 SEM micrographs of the corroded surfaces of both the superalloys tested in 2N H<sub>2</sub>SO<sub>4</sub>:

- (a) Fe-base superalloy MA 956
- (b) – (c) Ni-base superalloy MA 754 at different magnifications

Figure 3.26 Anodic polarization curves of Fe- and Ni- base superalloys in 0.6N NaCl solution.

Figure 3.27 SEM micrographs of the corroded surfaces of both the superalloys tested in 0.6N NaCl solution:

- (a) –(b) Fe-base superalloy at different magnifications
- (c) –(d) Ni-base superalloy at different magnifications

Figure 3.28 Anodic polarization curves for hydrogen sintered boride based cermet corresponding to different H<sub>2</sub>SO<sub>4</sub> concentrations.

Figure 3.29 Anodic polarization curves for vacuum sintered boride based cermet corresponding to different H<sub>2</sub>SO<sub>4</sub> concentrations.

Figure 3.30 Corrosion rate variation of boride based cermets (sintered in hydrogen and vacuum respectively) with respect to H<sub>2</sub>SO<sub>4</sub> concentration.

Figure 3.31 Optical micrographs of boride based cermets:

- (a) sintered in hydrogen (as-polished)
- (b) sintered in vacuum (as-etched)

Figure 3.32 Anodic polarization curves of boride based cermets (sintered in hydrogen and vacuum respectively) in 0.6N NaCl solution.

Figure 3.33 SEM micrographs of corroded surfaces of cermets sintered in different atmospheres:

- (a)–(b) Hydrogen
- (c) Vacuum

## ABSTRACT

Sintering is an important technique to consolidate metal and alloy powders into net shape complicated parts. Parts prepared by conventional sintering do contain residual porosities, the variation in which may cause different responses under corrosive atmospheres. In the present study fully dense P/M alloys based on aluminium, copper, iron and nickel have been selected. These were prepared after hot consolidating sintered preforms. The uniformity in microstructure in P/M products is a well established feature.

In the present investigation NaCl solution and  $\text{H}_2\text{SO}_4$  of different concentrations have been selected. Potentiodynamic plots establish good correlations in corrosion responses. The study of X-ray diffraction, optical microscopy and scanning electron microscopy of the as-received and corroded alloys is being done.

In 0.6N NaCl solution, RS 7091 aluminium alloy which is produced by rapid solidification route, is found to exhibit good corrosion resistance as compared to dispersion strengthened alloys, viz. DISPAL and ODS copper. This is attributed to the extension of solid solubility through rapid solidification. The low alloy steel Fe-5Cu-0.5C is attacked more rapidly in both  $\text{H}_2\text{SO}_4$  and NaCl media than the plain carbon steel Fe-0.5C. ASP 30 tool steel is more corrosion resistant than ASP 23 tool steel in both the media, which has been attributed to the presence of cobalt (8.5 wt. %) in the former. A relatively high corrosion rate obtained for Ferro-TiC cermet is associated to the attack of the corrosive medium on the steel binder phase. The superalloys MA 956 and MA 754 were found to be good corrosion resistant in both the media. Porosity plays a vital role in dictating the corrosion behaviour, which is seen in the case of boride based cermets.

# Chapter –1

## Literature Review

### 1.1. Introduction:

One attraction of powder metallurgy (P/M) is the ability to fabricate high quality complex parts to close tolerances in an economical manner. In essence, P/M takes a metal powder with specific attributes of size, shape, and packing, then converts into a strong, precise, high performance shape. Key steps include the shaping of the powder and subsequent thermal bonding of the particles by sintering.

Many attributes contribute to the success of P/M. First are the many applications which rely on the economical production of complex parts. Components for the automotive industry represent good examples of this area and their production is a large P/M activity. There are also unique property or microstructure justifications for using P/M approaches. Some examples include porous metals, oxide dispersion strengthened alloys, cermets (ceramic-metal composites), and cemented carbides. The inability to fabricate these unique microstructures by other techniques has contributed a large part to the growth of P/M.

Interest in superalloy P/M processing is due to several reasons [1]. First, advanced superalloys are prone to severe macrosegregation, which exhibit successful ingot breakdown. Conceptually, powder metallurgy offers a method for overcoming this problem. Furthermore, there is the possibility that P/M

processing may offer improved economics through near-net shapes and fewer processing steps than required for ingot technology.

The rapid solidification aspect of P/M has led to several new materials involving new compositions, microstructures, or processing routes. Powders produced by rapid solidification have very different structures from materials solidified under equilibrium conditions.

One of the methods by which dispersion strengthening can be achieved is mechanical alloying (MA), where the incorporation of a distribution of small, inert second phase particles throughout the microstructure provide high temperature strength and creep resistance.

The major steps involved in P/M processing are

1. Green Compaction
2. Sintering
3. Post-sintering treatments

The compaction of metal powders has the following major functions [2]:

- To consolidate the powder into desired shapes
- To impact, as much as possible, the desired final dimensions with due consideration for any dimensional changes resulting from sintering
- To give the desired level and type of porosity
- To provide adequate strength for subsequent handling

Die compaction represents the most widely used method and is considered as the 'Conventional' technique.

The type of sintering routes includes solid state sintering, liquid phase sintering and activated sintering. There are two variations of liquid phase

sintering, i.e. normal liquid phase sintering (This is again classified into two categories - transient liquid phase sintering, and persistent liquid phase sintering) and infiltration. A special variant of liquid phase sintering is supersolidus sintering.

Sintered compacts in most cases can be subjected to treatments analogous to those for wrought metals. The compact can be adjusted for surface finish or final dimensions using coining or sizing operations. Another operation may be coating. Other post-sintering treatments for P/M compacts include machining, welding, brazing and surface finishing. These operations are generally dependent on sintered density.

## **1.2. Polarization Technique and its significance:**

The main advantage of electrochemical techniques for studying corrosion over traditional coupon testing is that it allows the rapid determination of the corrosion rate of a sample without requiring long-term testing. Corrosion rate itself can vary with time under a given set of conditions, so electrochemical corrosion measurements only give a snapshot of how the system behaved under those conditions at that point in time. Long term testing is still required if one needs to know how a metal reacts after 12 months in a given test environment. But short-term electrochemical measurements are more than sufficient in many cases, as they allow one to compare the performance of inhibitors or to decide that a given metal is corroding too rapidly under those conditions to be a valid candidate for the application. Polarization experiments are the most commonly used electrochemical methods for assessing corrosion behaviour.

Potential measurements alone indicate the state of a system, not the rate of corrosion, for which purpose the current density is required and the potential-current relationship, i.e. the polarization characteristics, of a system

can be valuable in assessing the propensity for and the rates of various forms of corrosion. The representation of polarization behaviour in the form of the well-known Evans diagram, requiring the determination of the potential-current density relationships for the anodic and cathodic reactions, and their extrapolation to the point of intersection whereby the corrosion potential and current density are defined for the given system, is often used in the laboratory studies but is time-consuming. Like all corrosion test methods it is not universally applicable, being most reliable in the context of general, as opposed to localized, forms of corrosion, in high conductivity electrolytes and where the only electrochemical reactions occupying are the corrosion reactions.

### **1.2.1. Potentiodynamic Polarization Method:**

Polarization measurements are dynamic in the sense that they involve imposing changes in potential and current, but in the forms most extensively used they involve relatively small departures from the open circuit potential. In other instances, particularly in relation to pitting or stress corrosion, potentiodynamic methods are sometimes applicable involving sweeping a relatively wide range of potentials or current densities. Potentiodynamic polarization curves, whilst being less precise than potentiostatic step curves, are produced more rapidly and are useful for comparative purposes.

### **1.2.2. Characteristics of a Polarization Curve:**

Figure 1.1 shows one idealized polarization curve for an active-passive metal. The most useful potentiodynamic polarization cycle is to start with the test electrode cathodically polarized in the fluid of interest. The potential is slowly increased with respect to the reference electrode so that the sample passes through the equilibrium corrosion situation ( $E_{\text{corr}}$ ) and then becomes anodically polarized, i.e. forced to corrode. Due to the large range of current

densities measured, a log plot is used. The resulting cusp in the curve clearly identifies the equilibrium corrosion potential,  $E_{\text{corr}}$ , and facilitates the definition of the equilibrium anodic corrosion current density,  $I_{\text{corr}}$ . When the system is anodically polarized, the sample is forced to corrode and the current density, increases until the build up of corrosion products forms a protective layer on the surface (B) and the sample is passivated. The corrosion rate stops increasing. The potential making the onset of passivity is termed the primary passivation potential and is denoted by  $E_{\text{pp}}$ . If aggressive species, such as chloride ions, are not present, then the end of the passive region of the curve is determined by the onset of transpassive dissolution of the film or the initiation of another anodic reaction, such as oxygen evolution, on the specimen surface (D). The passive film is subjected to pitting corrosion when chloride or another aggressive species is present. The onset of pitting is marked by a sudden increase in the current density (point C) – the potential where this increase occurs is called the pitting potential,  $E_{\text{p}}$ , or the breakdown potential,  $E_{\text{b}}$ . In a polarization curve, such as the one shown in Figure 1.1, the potential provides the driving force for a reaction to occur and the current density (the current/surface area of the specimen) is a measure of the corrosion rate.

### 1.2.3. Determination of Corrosion Rate:

Once  $I_{\text{corr}}$  is known one can obtain a corrosion rate from it by using the following conversion formula [3]:

$$\text{Corrosion Rate} = C (EW/d) (I_{\text{corr}} / A)$$

Where,

EW – the equivalent weight of the sample in g,

A – the sample area in  $\text{cm}^2$ ,

d – density of the sample in g/ml,

C – a conversion constant that is dependent upon the units desired.

The value of C is  $1.287 \times 10^5$  when  $I_{\text{corr}}$  is expressed as a current in amperes and the corrosion rate is desired in milli-inches per year (mpy). On the other hand C is  $3.060 \times 10^4$  when  $I_{\text{corr}}$  is in amperes and corrosion rate is desired in millimeters per year (mmpy). If  $I_{\text{corr}}$  is already expressed as current density, the  $I_{\text{corr}}/A$  term is just replaced by  $I_{\text{corr}}$ .

For alloys, the equivalent weight EW can be calculated using the atomic fraction of each alloying element in an expression such as [4]:

$$\text{Alloy } E.W = \sum_{i=1}^m \frac{f_i M_i}{n_i}$$

Where,

$f_i$  –the atomic fraction of the  $i^{\text{th}}$  component of the alloy,

$M_i$  –the atomic weight of  $i^{\text{th}}$  component element,

$n_i$  –the electron loss required to oxidize the  $i^{\text{th}}$  component element

under the conditions of the corrosion process ( $n_i$  is usually equal to the stable valence of the element),

$m$  –the number of component elements in the alloy

So 
$$\text{Alloy } E.W = \frac{f_1 M_1}{n_1} + \frac{f_2 M_2}{n_2} + \dots \dots \dots \frac{f_i M_i}{n_i}$$

### 1.3. Review on the investigated alloy systems:

The alloys investigated come under the following categories.

- **Al- and Cu- based alloys:**

Rapidly Solidified (RS) Aluminium, Dispersion Strengthened Aluminium (DISPAL), Oxide Dispersion Strengthened (ODS) Copper.



- **Ferrous alloys and Ferro-TiC:**

Plain carbon steel Fe-0.5C, Low alloy steel Fe-5Cu-0.5C, Tool steels ASP 23 and ASP 30, Ferro-TiC cermet.

- **Superalloys:**

ODS Fe-based Superalloy- MA 956

ODS Ni-based Superalloy- MA 754

- **Boride based cermets:**

Mo<sub>2</sub>FeB<sub>2</sub> based cermets sintered in hydrogen and vacuum.

The P/M processing details of these alloys along with their corrosion behaviours are highlighted in following sections.

### **1.3.1. Al- and Cu- based alloys :**

The primary use of the high strength aluminium alloys is in the aerospace industry. These offer high strength and modulus of elasticity with good corrosion resistance, improved fatigue and thermal stability. The application of rapid solidification processing technique to 7XXX series aluminium alloys resulted in the first generation of Alcoa make, corrosion resistant rapidly solidified high strength P/M 7090 and 7091 aluminium alloys, wherein Co, a transition metal with a very limited room temperature solid solubility in aluminium was incorporated in the chemistry of 7XXX series alloys in place of more conventional additions such as Cr, Mn or Zr.

The microstructural refinement (e.g. fine grain size and elimination of coarse intermetallics), chemical uniformity and extended solid solubility inherent in rapid solidification processing and their effect on various properties such as room temperature strength, fracture toughness and stress corrosion cracking has spurred the research activity in the evaluation of various properties of 7090 and 7091 alloys.

Over the years, a wide range of metals and alloys have been strengthened by the dispersion of fine insoluble phases in them. The submicron size dispersoids, which are stable up to the melting point of the metal, maintain the strength of the alloy even at elevated temperatures. The conventional alloys although exhibit high strengths at lower temperatures; there is a rapid fall in strength with increasing temperatures. The ability to retain strength over an extended temperature range is a feature unique to dispersion strengthened alloys. The improvement in the strength of the metals and alloys largely depends on achieving a uniform dispersion of fine particles in the matrix. Such high strength alloys are used in turbine blades, in components of heat exchangers and heat engine tubes, and in nuclear power plants and space applications.

Dispersion strengthened aluminium (DISPAL) was first fabricated by Jangg *et al.* [5] in 1977 by milling together aluminium powder with lamp black in high energy attritor mill followed by cold compaction, heat treatment and hot extrusion at 550 C. The thin film oxide covering aluminium particle gets ruptured due to the deformation and exposes virgin aluminium surface to carbon, to form carbide. The carbide particles comprise of 80 vol. % of total dispersoid and the oxides are the rest. The morphology of the two dispersoids differ from each other such that carbides are acicular in nature (18 – 80 nm in diameter and up to 100 nm length) and the oxides in platelet form (20 – 50 nm in diameter and 10 – 25 Å thick). Such a material has been used as piston heads for engines in high performance racing motorcycles. It is also used as high temperature electrical conductors in sodium battery at operation temperatures above 300 C.

Dispersion strengthened Cu-Al<sub>2</sub>O<sub>3</sub> alloy has been commercially manufactured by SCM (presently OMG America) corporation, USA, under the

name Glid Cop. In this process, a dilute alloy of Cu and Al is atomized and the powder thus obtained is blended with an oxidant which is an intimate mixture of cuprous oxide and a carefully controlled amount of  $\text{Al}_2\text{O}_3$ . Oxidant oxidizes the aluminium present in the alloy and thus forms dispersion strengthened copper. The preform is hot consolidated after reduction treatment. The  $\text{Al}_2\text{O}_3$  content in this grade of ODS copper, ranges from 0.9 – 2.7 vol. %  $\text{Al}_2\text{O}_3$  [6,7].

Literature on corrosion [8] reports a linear behaviour in the wt. loss vs.  $\text{H}_2\text{SO}_4$  concentration for commercially purity aluminium within the concentration range of 40%, i.e., 0 – 15N (Figure 1.2). The early work of Haarr<sup>[9]</sup>, Lyle and Cebulak<sup>[10,11]</sup>, Lyle and Weiss<sup>[12]</sup>, and Otto<sup>[13]</sup> demonstrated improvements in stress corrosion cracking resistance and survival rate for P/M 7XXX alloys containing various amounts of Co as compared to I/M 7075 control specimens, with survival rate increasing with increasing Co content up to 0.8 wt. Percent in 3.5% NaCl solution.

The effects of rapid solidification and alloying on the pitting corrosion resistance of binary and ternary aluminium alloys containing Mg, Ti, Mn, Cr, Fe, Ni, Cu, Zn, Zr, Nb and/or Si in deaerated 0.5N NaCl at room temperature was reported by Yoshika *et al.* [14], who found that rapid solidification significantly ennobled the pitting potential except for alloys containing Mg, Fe, or Zn, and enhanced the open circuit corrosion resistance due to decrease in both anodic and cathodic current densities. This is mainly attributed to the formation of the primary Al solid solution, supersaturated with solute atoms. The precipitation of the second phase is often detrimental for the corrosion resistance, but the extension of the solid solubility by rapid solidification is effective for enhancing the corrosion resistance. Although alloying of aluminium with various elements exhibits different corrosion behaviour, the

extension of the solid solubility through rapid solidification is beneficial in improving the pitting corrosion resistance of aluminium.

Surface corrosion comparisons of some aluminium alloys in 3.5% NaCl solution were done by Shaw [15]. He found that the IN-9021 material is very susceptible to pitting and exhibits a high general corrosion rate, being three times the corrosion rates of 7075 and 2024 alloy. The chemical composition and corrosion rate data of the Al alloys investigated by Shaw are given in Table 1.1 and 1.2 respectively.

### **1.3.2. Ferrous alloys and Ferro-TiC :**

The addition of both copper and carbon in sintered iron offers greater strength and hardness than the addition of either alone. Fe-Cu or Fe-Cu-C steels exhibit transient liquid phase sintering. The most widely used production practices for P/M tool steels use gas atomization and hot isostatic pressing (HIP). Such steels exhibit super solidus liquid phase sintering. Cobalt in such steels does not act as carbide former, but enters into the matrix. Cobalt increases the solidus temperature, thus permitting the use of high austenitizing temperatures to achieve greater solutioning of alloying elements. Furthermore cobalt enhances hot hardness and temper resistance. Steel bonded titanium carbides are the types of cermets, which can be machined and are corrosion, oxidation and wear resistant. One of the attractive properties of steel bonded TiC is that it is heat treatable. Among the steel bonded titanium carbides, Ferro-TiC grades are very common, for which various grades have been developed [2].

A detailed sintering study of Fe-8%Cu, C (> 0.8%) and Fe-Cu-1.0%C (Cu > 6%) premixes was reported by Majima and Mitani [16]. The steel powder premix compacts of Fe-0.5C and Fe-5Cu-0.5C were sintered in hydrogen at 1120 °C for 1 hour. The full details of the process are given

elsewhere [17]. The anti segregation process (ASP) for production of P/M high speed steels is described elsewhere [18]. The Ferro-TiC cermets are generally liquid phase sintered in vacuum in the temperature range of 1350 °C – 1500 °C depending on the steel binder compositions.

Literature [19] reports a linear behaviour in corrosion rate vs.  $\text{H}_2\text{SO}_4$  concentration of iron within the concentration range of 25%, i.e., 0 – 9.5N (Figure 1.3). Literatures [20,21] report the beneficial effect of Cu in reducing the corrosion rates of steels in  $\text{H}_2\text{SO}_4$ .

### **1.3.3. Superalloys :**

Mechanical alloying (MA) provides a means for producing powder metallurgy (P/M) dispersion-strengthened alloys of widely varying compositions with a unique set of properties.

One of the oxide dispersion-strengthened P/M ferritic superalloys reported is MA 956, which composition is based on conventional kanthal. The advantage is its high melting point together with a low density and low thermal expansion, also its excellent oxidation and corrosion resistance. The major dispersoid is  $3 \text{ Y}_2\text{O}_3 \cdot 5 \text{ Al}_2\text{O}_3$  together with some  $\text{Y}_2\text{O}_3$ ,  $\text{Al}_2\text{O}_3$ . There is also some Ti(C, N) which have been found to be situated mainly on the grain boundaries with an average size of 200 nm and an angular shape. The  $\text{Al}_2\text{O}_3$  particles are coarse and occasionally arranged in long stringers. The superalloy MA 754 is basically an ODS Ni-Cr solid solution. The oxide dispersoid is Yttrium aluminate formed by the reaction between added  $\text{Y}_2\text{O}_3$ , excess oxygen in the powder, and a trace of aluminium added to the getter oxygen. The mean particle size and volume fraction of dispersoid in MA 754 are 15 nm and 1.3% respectively. Although introduction of P/M parts into aerospace systems has been limited because of costly and lengthy qualification requirements, significantly P/M part usage has been achieved.

Nutting *et al.* [22], using optical and transmission electron microscopy together with X-ray diffraction, studied grain structures, phase population and the defect structures of MA 956 at several stages of the manufacturing process. The oxidation resistance of the ODS MA 956 is determined by the aluminium content, which is between 4% and 5% by wt. Much more important than the integral aluminium content is the active aluminium portion dissolved in the matrix. These alloys were produced by INCO, UK; using mechanical alloying followed by conventional HIP and hot forging [23].

Literature [24] shows that in a chloride environment nickel is less susceptible for pitting than iron, i.e. it has a higher pitting potential.

#### **1.3.4. Boride based cermets :**

The ternary boride ( $\text{Mo}_2\text{FeB}_2$ ) based hard cermets were first commercially developed in Japan in early eighties. Ternary boride based cermets with varying metal binders were developed by Takagi [25]. Liquid phase sintering provided a route through which full density can be attained. Takagi *et al.* [25] summarized the important criteria for development of boride based cermet as

1. Selection of boride which can coexist with a metal matrix.
2. Prevention of formation of brittle third phase resulting due to chemical reaction between the borides and metal matrix.
3. Formation of liquid phase during the process to aid densification.
4. Restricting grain growth during high temperature sintering.

Different sintering atmospheres, i.e. hydrogen and vacuum were used separately during liquid phase sintering of this cermet at 1245 °C for 30 minutes. Full details of the process are given elsewhere [26].

Nickel additions were made to the system by Takagi *et al.* [27,28] to improve corrosion resistance, transverse rupture strength and hardness. In another investigation, Takagi *et al.* [29] introduced chromium into the system to improve the corrosion properties.

#### **1.4. Scope of the Present Work :**

The residual porosity in the sintered parts affects the mechanical and corrosion resistance properties. The corrosion resistance of P/M products is often inferior to equivalent wrought materials. The lower corrosion resistance results from three factors [30]:

- (i) the presence of pores which give a higher total surface area per unit volume
- (ii) the long term anneals associated with sintering, and
- (iii) the interstitial pickup from the sintering atmosphere.

The present work is an attempt to get information about the corrosion behaviour of the P/M ferrous and non-ferrous alloys in  $H_2SO_4$  solution of different concentrations (0.1N – 5N) and 0.6N NaCl solution. Literature review reveals that not much investigations have been carried out in understanding the corrosion behaviour of the investigated alloys, which possess variable porosities, different dispersoids and alloying additions to evolve unique microstructures. These microstructures, no doubt, have wide influence on the mechanical properties, but the details of their corrosion behaviour are lacking.

Table 1.1 Nominal Chemical Content of different Al alloys, wt. % [15].

<u>Element</u>	<u>Material</u>			
	<u>7075</u>	<u>2024</u>	<u>6061</u>	<u>IN-9021</u>
Si	0.4	0.5	0.6	0.05
Fe	0.5	0.5	0.7	0.02
Cu	1.6	4.3	0.3	4.0
Mn	0.3	0.6	0.15	0.01
Mg	2.5	1.5	1.0	1.5
Cr	0.3	0.1	0.2	0.01
Zn	5.6	0.25	0.25	0.01
Ti	0.2	0.15	0.15	-
O	-	-	-	0.8
C	-	-	-	1.1

Table 1.2 Corrosion Rate Comparison [15].  
(Two Week Test)

<u>Material</u>	<u>Mean Value, mpy</u>	<u>Standard Deviation</u>
7075-T6	6.49	± 0.47
2024-T4	5.49	± 0.65
6061-T6511	2.11	± 0.19
IN9021-T452	17.47	± 6.43



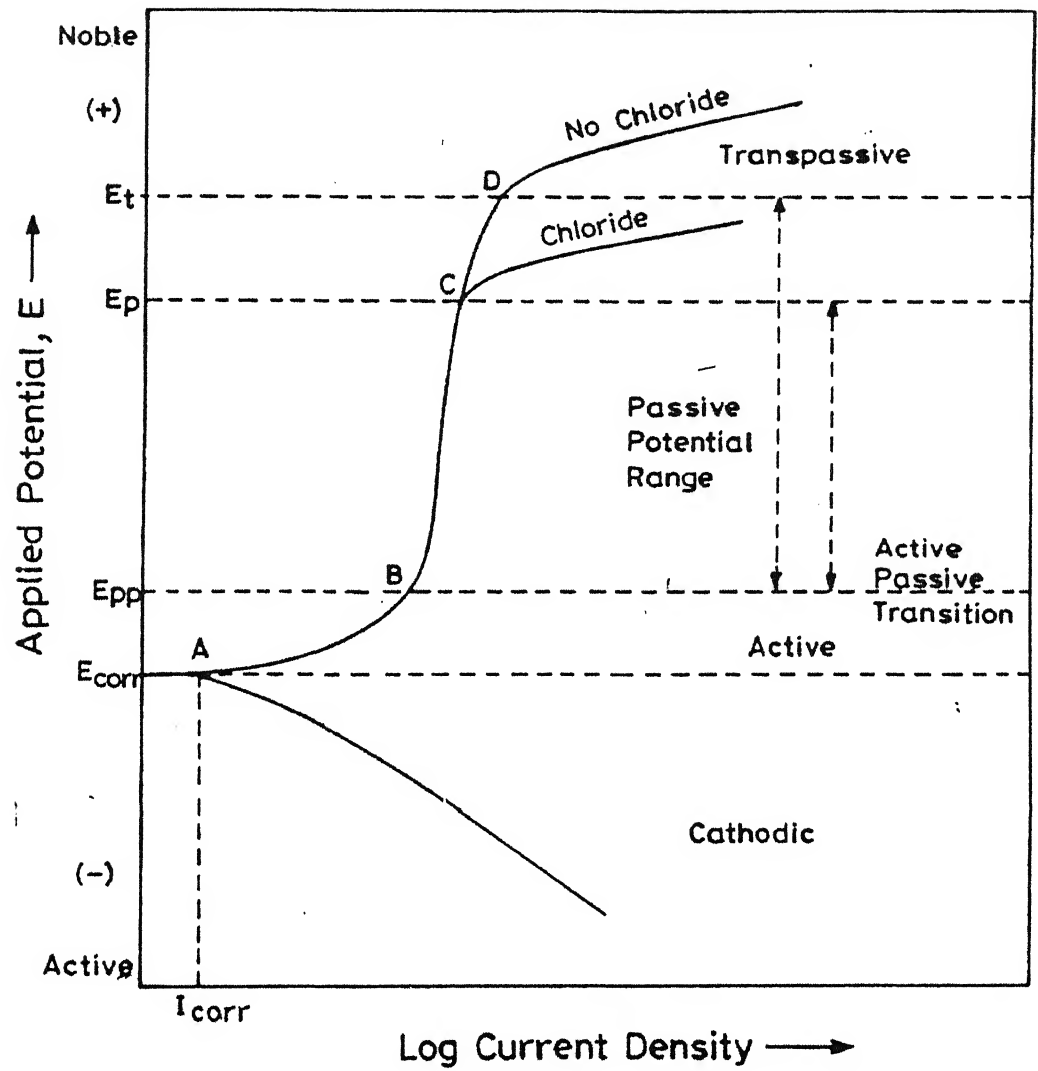


Figure 1.1 Idealized Polarization Curve.

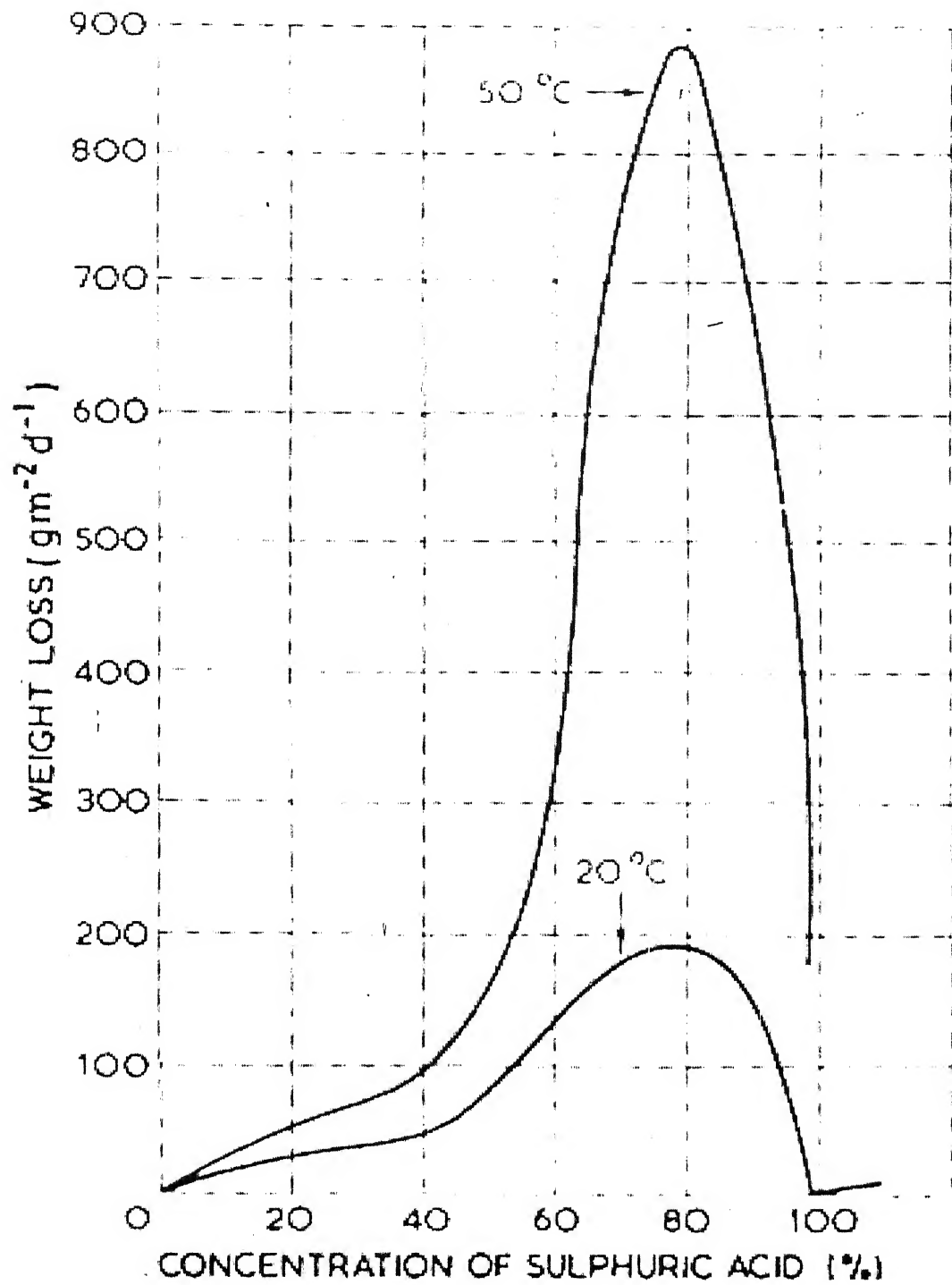


Figure 1.2 Action of sulphuric acid of various concentrations on commercial-purity aluminium [8].

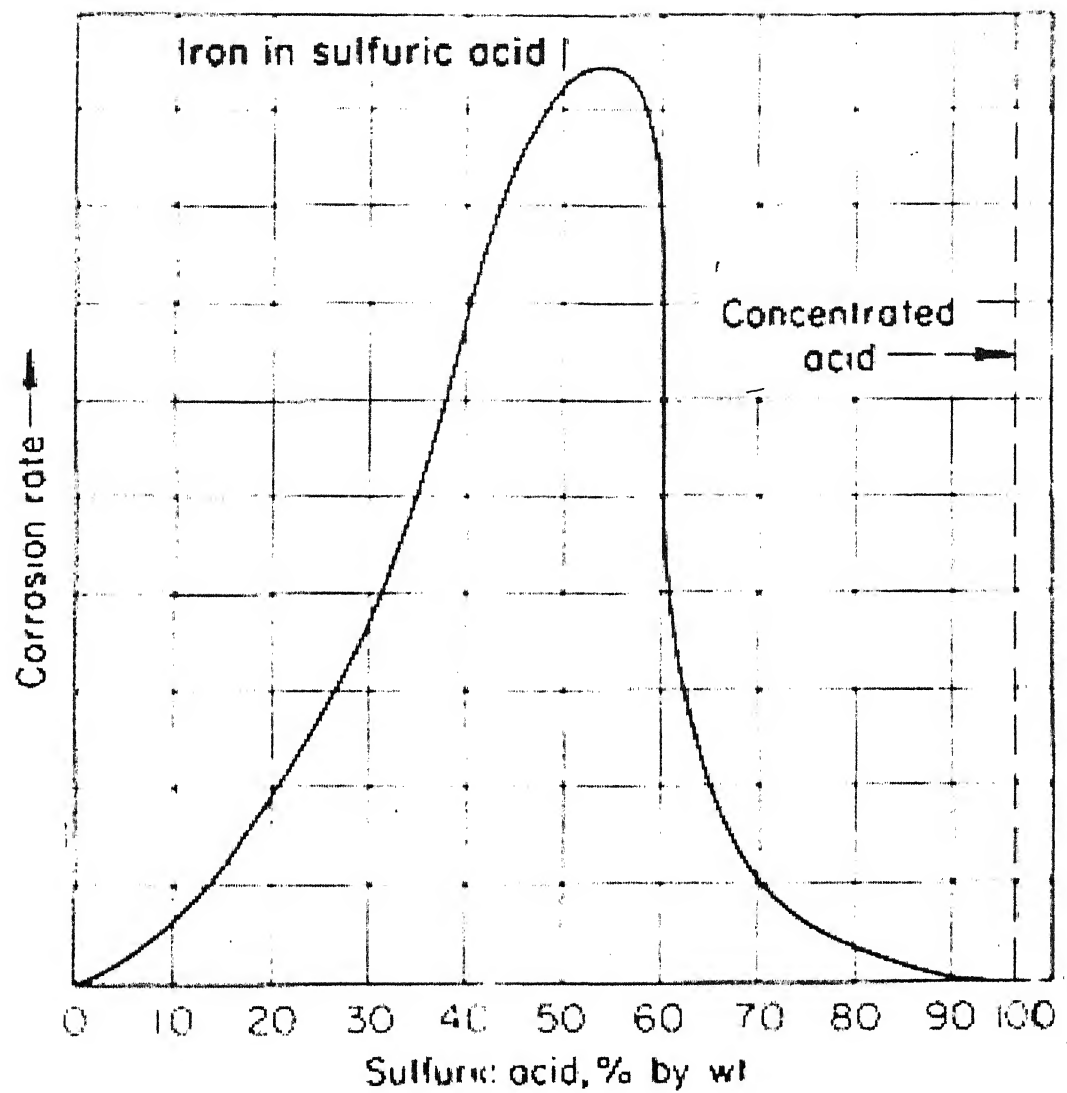


Figure 1.3 Effect of acid concentration on the corrosion rate of iron completely immersed in aqueous solution of sulfuric acid at room temperature [19].

## Chapter - 2

### Experimental Procedure

#### 2.1. Details of the investigated alloys :

##### 2.1.1. Al- and Cu- based alloys :

The chemical compositions and other relevant data of the following three alloys are given in Table 2.1.

- RS Aluminium: The alloy used in the present study was an Alcoa make P/M 7091 aluminium alloy processed by rapid solidification technique followed by hot extrusion. The as-received alloy was in the overaged temper of T7E69.
- DISPAL: This alloy (DISPAL2) was supplied in the form of circular bars of 25mm dia × 300mm length by the manufacturer 'Sintermetallwerk', Krebsoge (Germany).
- ODS Copper: The alloy i.e. alumina dispersed copper (Trade name Glid Cop) was supplied in the form of hot extruded rods of 12.5mm diameter by the manufacturer SCM corporation (Presently OMG America), USA.

##### 2.1.2. Ferrous alloys and Ferro-TiC :

The following alloys were investigated;

- Fe-0.5C and Fe-5Cu-0.5C: These sintered billets were prepared in Powder Metallurgy Lab. of IIT Kanpur. The details are given elsewhere [17].

- ASP 23 and ASP 30: Fully dense ASP 23 and ASP 30 P/M high speed steels were supplied by M/S Associated Swedish Steels AB, Stockholm, Sweden.
- Ferro-TiC: The Ferro-TiC cermet in the form of short bars was supplied by Alloy Technology International, Inc., West Nyack, NY.

The chemical compositions and sintered density data along with porosity data of these alloys are given in Table 2.2.

### **2.1.3. Superalloys :**

The chemical compositions and density data of the superalloys MA 956 and MA 754 are given in Table 2.3. These superalloys were produced by INCO, UK.

### **2.1.4. Boride based cermets :**

The chemical compositions and other relevant data of the cermets sintered in hydrogen and vacuum are given in Table 2.4. These cermets were prepared in Powder Metallurgy Lab. of IIT Kanpur. The details are given elsewhere [26].

## **2.2. Specimen Preparation prior to Corrosion Testing :**

For studying the Corrosion behaviour, a desired surface finish is a must. The cylindrical specimens (diameter 0.8cm - 1.27cm and width 0.3cm - 0.8cm) were first ground flat on a grinding belt and then polished using a series of emery papers up to 1000 grit size. The final wet polishing was subsequently carried out on a polishing wheel using 0.3 $\mu$ m size alumina powder suspension in distilled water. After metallography the samples were re-polished and mounted in epoxy with electrical connections through the rear of the mounts.

## **2.3. Electrolyte Solution Preparation :**

The electrolytes used in the present investigation were  $\text{H}_2\text{SO}_4$  (0.1N - 5N) and 0.6N NaCl solutions.  $\text{H}_2\text{SO}_4$  solution of different concentrations were prepared by diluting the concentrated solution (36.8N, 95 - 98% pure) to the appropriate level with distilled water. The sodium chloride solution corresponding to the artificial sea water (0.6N NaCl or 3.5% NaCl) was prepared by mixing 35gms of NaCl in 1000cc distilled water, followed by shaking and then making up to the level. For each run during corrosion testing, fresh solutions were used.

## **2.4. Potentiostat Instrument Details :**

The EG & G Princeton Applied Research Model 352 Soft Corr<sup>TM</sup> corrosion measurement software is designed to measure and analyze corrosion quickly, easily, and reliably, using a variety of techniques. The potentiostat used in the present work was EG & G PARC VersaStat (Model 253).

The versatile design of the Model 352 software allows one to apply any one of the following

- Scanning Techniques
  - Potentiodynamic Polarization
  - Tafel Plots
  - Linear Polarization (Polarization Resistance)
  - Cyclic Polarization (Pitting Scans)
- Timed Techniques
  - Potentiostatic
  - Galvanostatic
- Potentiokinetic Reactivation
- Galvanic Corrosion

The Model 352 can perform three types of calculations

- QuickCalc Tafel Analysis
- PARCalc Tafel Analysis
- Polarization Resistance Analysis

The QuickCalc routine gives a way to get a quick and rough calculation of the corrosion current and corrosion rate from the experimental data when the data has the classic Tafel plot features. The PARCalc Tafel Analysis routine statistically fits the experimental data to the Stern-Geary Model for a corroding system. The routine automatically selects the data that lies within the Tafel region ( $\pm 250\text{mV}$  with respect to the corrosion potential). It then calculates the corrosion current and corrosion rate (in either millimeters per year or milli-inches per year) and displays the results. The Polarization Resistance routine uses a linear regression analysis to calculate the polarization resistance, and then uses this value to determine the corrosion current and corrosion rate. The routine automatically selects data within  $\pm 20\text{mV}$  with respect to the corrosion potential and then performs the calculations.

The schematic diagram showing the positions of the electrodes is given in Figure 2.1. Photograph of the actual electrochemical polarization cell (which was used during the investigation) is shown in Figure 2.2.

## **2.5. Corrosion Testing :**

### **2.5.1. Potentiodynamic Anodic Polarization :**

Potentiodynamic polarization technique, which is a scanning technique, is generally used to produce a qualitative picture or 'finger print' of a substance in given solution. It also detects any tendency of the substance to passivate. For testing, the samples were subjected as the working electrodes and were connected in an electrical circuit, which allowed impression of an

external voltage and measurement of corrosion current against saturated calomel electrode (SCE). Graphite was used as counter electrode. The scanning rate was 1 mV/s and the testing was carried out at room temperature.

Normally, no calculations are performed on data from a potentiodynamic experiment. However, both the PARCalc and Polarization Resistance Analysis routines can select the appropriate potential regions and perform calculations on the data. Thus it is possible to get both qualitative and quantitative results from a single potentiodynamic plot. The calculation of corrosion rate is based on the expression given in section 1.2.3.

### **2.5.2. Weight Loss Experiment :**

The wt. loss experiment was carried out on seven alloy systems in 1(N) H<sub>2</sub>SO<sub>4</sub> solution for different time intervals. The wt. loss at each interval was determined with the help of an electronic balance after drying each sample. Initial wt., diameter, density and sample area were measured prior to this experiment.

The expression mils per year (mpy) is the most desirable way of expressing corrosion rates. This expression is readily calculated from the weight loss of the metal/alloy specimen during the corrosion test by the formula given below [31]:

$$\text{Corrosion Rate (mpy)} = \frac{534W}{DAT}$$

Where,

W = weight loss; mg

D = density of specimen; g/cm<sup>3</sup>

A = area of specimen; sq. in

T = exposure time; hr



## 2.6. Microstructural Studies :

### 2.6.1. Optical Microscopy :

Optical microscopic examination was carried out on the as-sintered and as-etched alloys using appropriate etchants. The etchants used for various materials are as follows:

<u>Etchant</u>	<u>Alloy</u>
FeCl <sub>3</sub> solution	ODS Copper, Fe-0.5C and Fe-5Cu-0.5C
Nital (2% HNO <sub>3</sub> solution)	ASP 23 and ASP 30
Keller's Reagent	RS Aluminium and DISPAL

For observing boride grain morphology clearly, a boride colouring PPP reagent was used as etchant. The composition of PPP reagent is as follows [32]:

10g - K<sub>3</sub> [Fe (CN)<sub>6</sub>],  
1g - K<sub>4</sub> [Fe (CN)<sub>6</sub>].3H<sub>2</sub>O,  
30g - KOH,  
100g - H<sub>2</sub>O,

In case of Ferro-TiC cermet, the as-polished alloy surface revealed the microstructure.

### 2.6.2. Scanning Electron Microscopy :

The scanning micrographs of the corroded surfaces of the alloys (in both H<sub>2</sub>SO<sub>4</sub> and NaCl media) were obtained by using JEOL, JSM - 840 A Scanning electron microscope.

## 2.7. X- Ray Diffraction Studies :

The X- ray diffraction study of as-received and corroded surfaces of the alloys (in both H<sub>2</sub>SO<sub>4</sub> and NaCl media) was carried out on Rich Seifert & Co.,

Germany make, ISO Debyelex - 2002 diffractometer using  $\text{Cu}_{k\alpha}$  radiation (wavelength,  $\lambda$  for  $\text{Cu}_{k\alpha}$  radiation is 1.541838 Angstrom).

The inter-planer spacing ( $d_{hkl}$ ) of various phases was calculated using Bragg's law [33],

$$d_{h,k,l} = \frac{\lambda}{2 \sin \theta_{h,k,l}} \text{ \AA}$$

Where,

$\lambda$  = wavelength of X- ray radiation used, in angstroms;

$\theta_{hkl}$  = Bragg angle of the (h k l ) diffracting planes, in degrees;

Indexing of X- ray diffraction patterns were done by going through the powder diffraction data files.

The value of a, for cubic systems deduced from each measured  $\theta$  is plotted against the corresponding value of  $\frac{1}{2} \left[ \frac{\cos^2 \theta}{\theta} + \frac{\cos^2 \theta}{\sin \theta} \right]$ . The point where the best straight line, through the experimental points, cuts the vertical axis, is the value of the lattice parameter.

To calculate the lattice parameter of alloys belonging to tetragonal systems viz. Boride, the following relation is used [34]:

$$\sin^2 \theta = \lambda^2 (h^2 + k^2 + l^2) / 4a^2 + \lambda^2 l^2 / 4c^2$$

While the value of 'a' is calculated from (h k 0) type planes, the value of 'c' obtained from (0 0 l) planes. Now the values of 'a' and 'c' deduced from each measured ' $\theta$ ' is plotted against the corresponding value of  $\frac{1}{2} \left[ \frac{\cos^2 \theta}{\theta} + \frac{\cos^2 \theta}{\sin \theta} \right]$  separately. The point where the best straight line, through the experimental points, cuts the vertical axis gives the values 'a' and 'c'.

Table 2.1 Chemical compositions and density data for Al- and Cu- based alloys.

Alloy	Density (gcm <sup>-3</sup> )	Nominal composition
RS 7091 aluminium	2.81	Zn    Mg    Cu    Co    O    Fe    Si    Al 5.7-7.1   2.0-3.0   1.1-1.8   0.2-0.6   0.2-0.5   0.15   0.12   bal (wt. %)
DISPAL	2.66	Al <sub>4</sub> C <sub>3</sub> Al <sub>2</sub> O <sub>3</sub> Al 9.0        5.0        bal (vol. %)
ODS copper	8.96	Al <sub>2</sub> O <sub>3</sub> Cu 0.9        99.1    (vol. %)

Table 2.2 Chemical compositions of sintered ferrous alloys with density and porosity data.

Alloy	Density (gcm <sup>-3</sup> )	Porosity (%)	Nominal composition
Fe-0.5C	6.56	17	C    Cu    Fe 0.5    0    bal (wt. %)
Fe-5Cu- 0.5C	6.50	18	C    Cu    Fe 0.5    5.0    bal (wt. %)
ASP 23	8.54	0	C    Si    Mn    Cr    Mo    W    Co    V    Fe 1.27   0.3   0.3   4.2   5.0   6.4   -   3.1   bal (wt. %)
ASP 30	8.63	0	C    Si    Mn    Cr    Mo    W    Co    V    Fe 1.27   0.3   0.3   4.2   5.0   6.4   8.5   3.1   bal (wt. %)
Ferro- TiC	6.34	0	TiC                      Tool steel binder C    Cr    Mo    Fe 45 (vol. %)   0.8   10.0   3.0   bal (wt. %)

Table 2.3 Chemical compositions and density data for Fe- and Ni- base superalloys.

Alloy	Density (gcm <sup>-3</sup> )	Nominal composition: wt %							
Fe-base superalloy (MA 956)	7.51	C	Si	Cu	Mn	Cr	Ti	Al	
		0.024	0.12	0.04	0.07	19.10	0.34	4.31	
		Co	Ni	P	S	N	Y <sub>2</sub> O <sub>3</sub>	Fe	
		0.02	0.24	0.005	0.004	0.028	0.48	bal	
Ni-base superalloy (MA 754)	8.30	C	Fe	Cr	Ti	Al	S	P	
		0.07	1.11	19.93	0.51	0.36	0.002	0.38	
		Y <sub>2</sub> O <sub>3</sub>	Ni						
		0.59	bal						

Table 2.4 Chemical composition of the ternary boride based cermet with sintered density and porosity data.

Composition (wt %)	Fe	Ni	Mo	Cr	B
	39.3	2.8	42.7	10.2	5
Sintered density (gcm <sup>-3</sup> )	6.22	(Hydrogen sintered)			
	8.27	(Vacuum sintered)			
% porosity	16.7	(Hydrogen sintered)			
	0.3	(Vacuum sintered)			

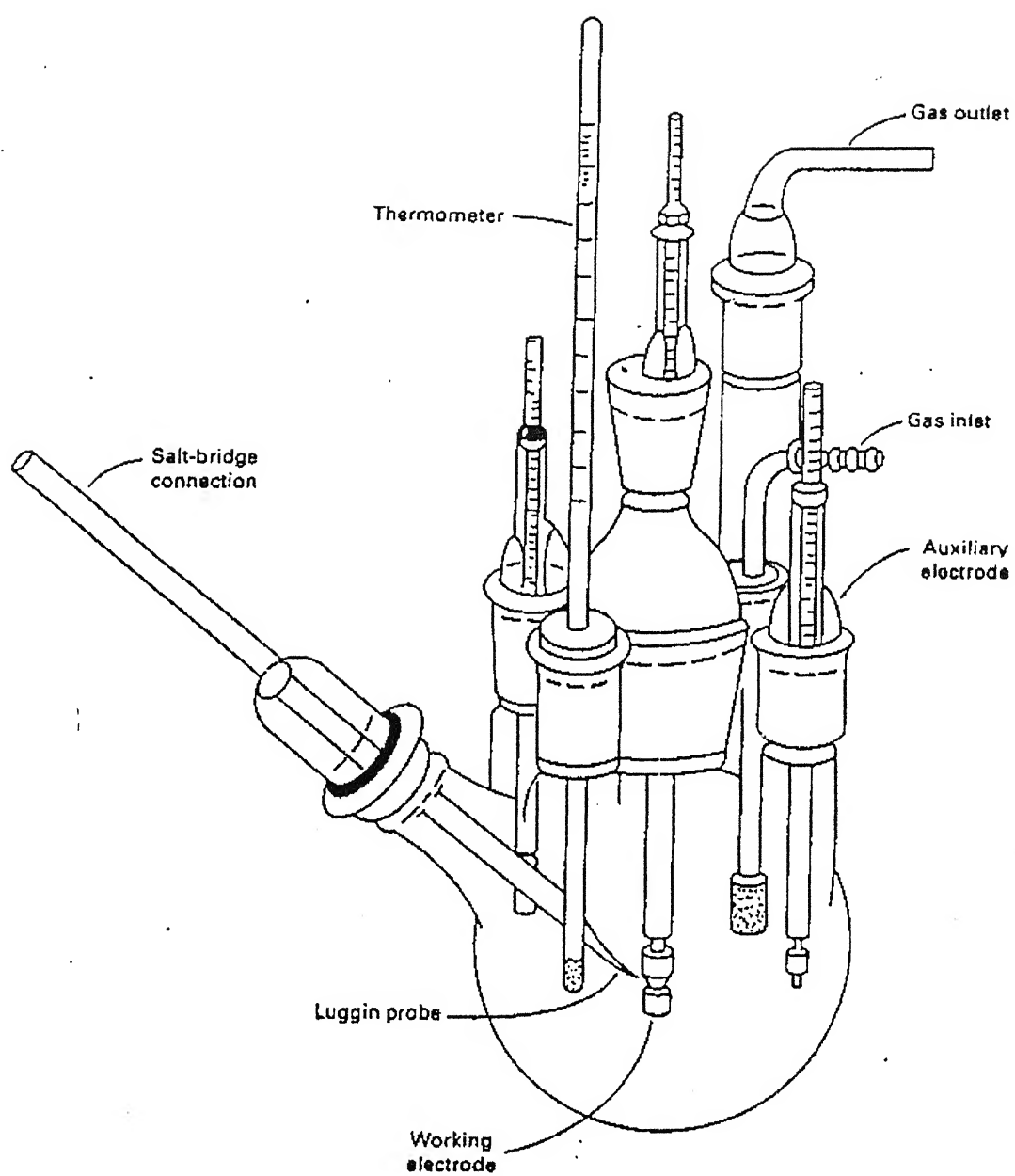


Figure 2.1 Typical electrochemical polarization cell illustrating locations for working and auxiliary electrodes, and associated cell components.

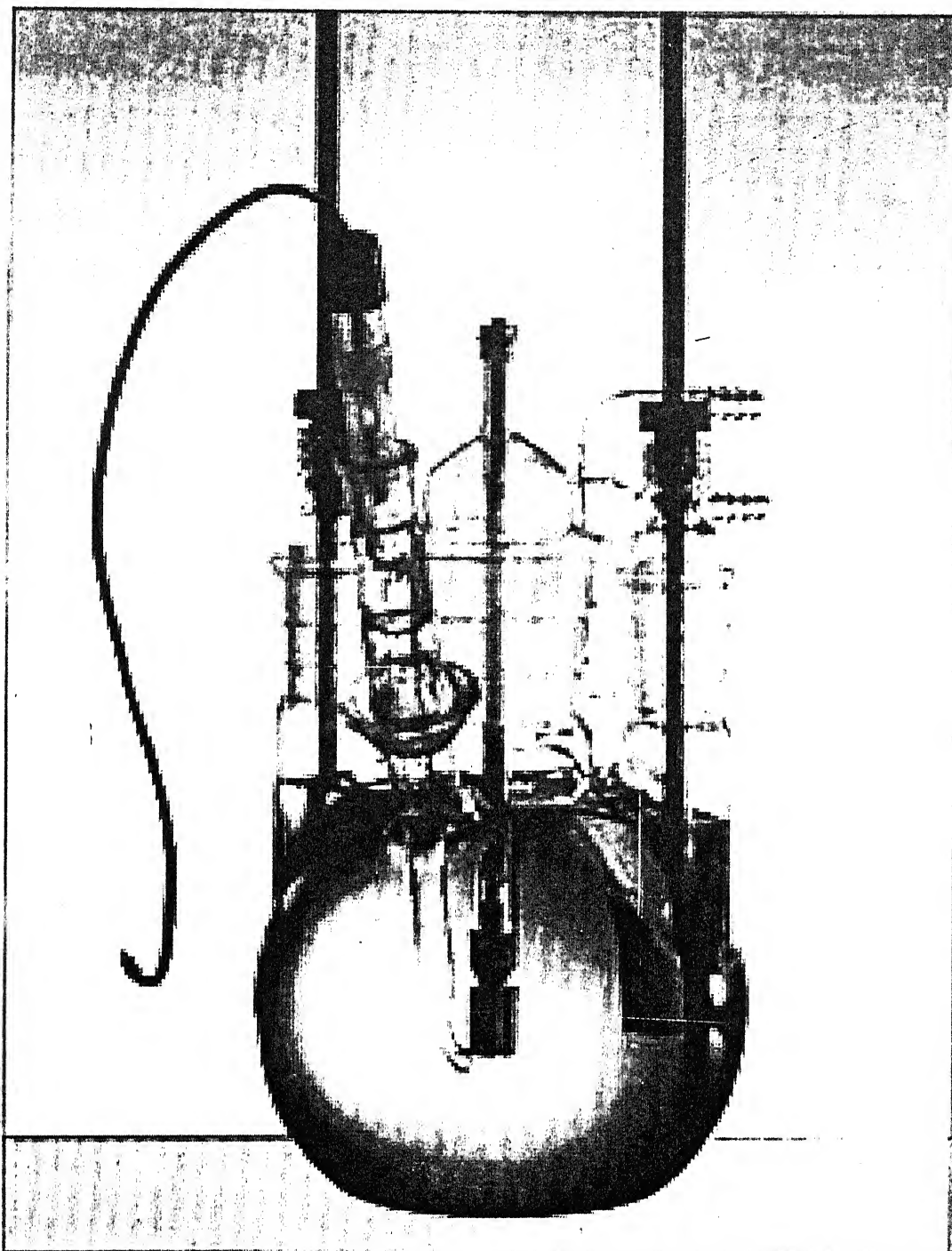


Figure 2.2      Photograph showing the electrochemical polarization cell used  
in the present investigation.

## Chapter – 3

### Results

This chapter is divided into four sections according to alloy systems investigated.

#### 3.1. Al- and Cu- based alloys:

##### 3.1.1. Corrosion in $H_2SO_4$ medium:

###### 3.1.1.1. Anodic Polarization studies:

Results of potentiodynamic polarization studies, carried out on the alloys in  $H_2SO_4$  media are presented in Figures 3.1-3.3 and Table 3.1. In case of RS aluminium there is a decrease in  $E_{corr}$  value with respect to  $H_2SO_4$  concentration, DISPAL shows this trend after 1N, whereas there is no regular trend in the variation of  $E_{corr}$  in case of ODS copper. For RS aluminium and ODS copper, decrease in  $I_{corr}$  value corresponds to 3N, and for DISPAL it is 2N, followed by an increase in  $I_{corr}$  value, though slightly in RS aluminium.

Figure 3.1 shows some typical anodic polarization curves of RS-aluminium in various  $H_2SO_4$  concentrations. The curves for 1N and 5N are quite similar; showing active, pre-passive, and passive regions, while the curve for 0.1N shows only active and passive regions. Figure 3.2 shows the anodic polarization curves of DISPAL. In this case the curves for 0.1N and 5N are quite similar, showing active, pre-passive, and passive regions, while the curve for 1N shows active and passive regions along with transpassive and secondary passive regions. Figure 3.3 shows the anodic polarization curves of ODS copper. The curves corresponding to 0.1N and 1N concentrations show active

and passive regions, while the curve for 5N concentration shows active, pre-passive, passive, transpassive and secondary passive regions. For the sake of convenience, corrosion rates of all the alloys with respect to  $\text{H}_2\text{SO}_4$  concentration are plotted in Figure 3.4 from the data given in Table 3.1. The trend is similar to the variation of  $I_{\text{corr}}$  value with the  $\text{H}_2\text{SO}_4$  concentration.

### **3.1.1.2. Weight Loss Experiment:**

Figure 3.5 (a) shows the plot of wt. loss per unit area vs. exposure time for the three alloys subjected to 1N  $\text{H}_2\text{SO}_4$ . It is evident that there is an increase in wt. loss with time for all the cases. From the data given in Table 3.2 the corrosion rates of these alloys are plotted in Figure 3.5 (b). The trend in corrosion rate variation is as follows:

RS aluminium > DISPAL > ODS copper

It is interesting to note that except ODS copper, the corrosion rate changes slowly after 360 hrs exposure.

### **3.1.1.3. X-ray diffraction studies:**

Due to the formation of relatively very thin oxide film at the surface of the alloys, no characteristic peaks for corresponding oxides were obtained. X-ray study was able to detect only the base elements. The lattice parameters for the base elements aluminium and copper of as-received and corroded surfaces of these three alloys are given in Table 3.3.

### **3.1.1.4. Optical and SEM studies:**

The optical micrographs of the as-etched surfaces of all the alloys are shown in Figure 3.6. RS aluminium alloy exhibits a pancake grain structure. DISPAL shows an exceedingly small matrix grain size, the dispersoids of carbide and oxide could not be resolved. The  $\text{Al}_2\text{O}_3$  particle size in DISPAL is too fine to be resolved by optical microscope.



The SEM micrographs of the corroded surfaces of all the alloys are shown in Figure 3.7. There is no significant change in the surface of RS aluminium alloy after the corrosion test. The surface of DISPAL is severely affected by  $H_2SO_4$  followed by ODS copper.

### **3.1.2. Corrosion in 0.6N NaCl:**

#### **3.1.2.1. Anodic Polarization studies:**

Results of potentiodynamic anodic polarization studies, carried out on all alloys in 0.6N NaCl solution are presented in Figure 3.8 and Table 3.4. The curve of RS aluminium shows active and passive regions. The additional features of the curve for DISPAL are pre-passive and transpassive regions and for ODS copper it is the pre-passive region. The trend in corrosion rate variation is as follows:

DISPAL > ODS copper > RS aluminium

#### **3.1.2.2. X-ray diffraction studies:**

The lattice parameters for the base elements aluminium and copper of as-received and corroded surfaces of these three alloys are given in Table 3.3.

#### **3.1.2.3. Optical and SEM studies:**

The SEM micrographs of the corroded surfaces of different alloys are shown in Figure 3.9. In case of RS aluminium and ODS copper lesser degree of corrosion is felt. However, in case of DISPAL, corrosion pits on the surface are observed.

## **3.2. Ferrous alloys and Ferro-TiC:**

### **3.2.1. Corrosion in H<sub>2</sub>SO<sub>4</sub> medium:**

#### **3.2.1.1. Anodic Polarization studies:**

Results of potentiodynamic polarization studies, carried out on all the alloys in H<sub>2</sub>SO<sub>4</sub> media are presented in Figures 3.10-3.14 and Table 3.5. There is an increase in  $E_{\text{corr}}$  value with concentration of H<sub>2</sub>SO<sub>4</sub> in Fe-0.5C, Fe-5Cu-0.5C, and ASP 30 steels. With increase in concentration of H<sub>2</sub>SO<sub>4</sub>, increase in  $I_{\text{corr}}$  value was obtained for ASP 23 and ASP 30. All other alloys did not show any particular trend.

Figure 3.10 shows some typical anodic polarization curves for Fe-0.5C steel, where the plots for 0.1N and 5N show active and passive regions. Figure 3.11 shows the anodic polarization curves for Fe-5Cu-0.5C steel, where no clear passive regions were obtained. For ASP 23 there is a distinct passive region for 1N (Figure 3.12) and for ASP 30 a passive region (Figure 3.13) in 0.1N solution. The anodic polarization curves for Ferro-TiC (Figure 3.14) show no clear passive region, the curves correspond to 0.1N and 1N solutions are similar. For the sake of convenience, corrosion rates of all the alloys with respect to H<sub>2</sub>SO<sub>4</sub> concentration are plotted in Figure 3.15, from the data given in Table 3.5. A comparison of both Fe-0.5C and Fe-5Cu-0.5C, and also ASP 23 and ASP 30 show similar behaviour. The trend is similar to the variation of  $I_{\text{corr}}$  value with the H<sub>2</sub>SO<sub>4</sub> concentration.

#### **3.2.1.2. Weight Loss Experiment:**

Figure 3.16 (a) shows the plot of wt. loss per unit area vs. exposure time for ASP 23 and ASP 30 steels subjected to 1N H<sub>2</sub>SO<sub>4</sub>. There is an increase in wt. loss with time. The corrosion rates with respect to time are also plotted in Figure 3.16 (b). ASP 23 shows a greater corrosion rate than ASP 30 at each

interval of time. After an exposure period of 360 hrs, the corrosion rate does not vary significantly.

### **3.2.1.3. X-ray diffraction studies:**

The lattice parameters for the TiC matrix for Ferro-TiC and base element iron for all the alloys in as-received and corroded conditions are given in Table 3.7.

### **3.2.1.4. Optical and SEM studies:**

The optical micrographs of the as-polished surface for Ferro-TiC and as-etched surfaces for all other alloys are shown in Figure 3.17. Both ASP 23 and ASP 30 show fine grain structures. The SEM micrographs of the corroded surfaces of all the alloys are shown in Figure 3.18. The surfaces of Fe-5Cu-0.5C and ASP 23 are attacked to a greater extent in comparison with Fe-0.5C and ASP 30.

## **3.2.2. Corrosion in 0.6N NaCl:**

### **3.2.2.1. Anodic Polarization studies:**

Results of potentiodynamic anodic polarization studies, carried out on these alloys in 0.6N NaCl solution are presented in Figure 3.19- 20 and Table 3.8. The curves show active and passive, and regions. The trend in corrosion rate variation is as follows:

$$\text{Fe-5Cu-0.5C} > \text{Fe-0.5C} > \text{Ferro-TiC} > \text{ASP 23} > \text{ASP 30}$$

### **3.2.2.2. X-ray diffraction studies:**

The lattice parameters for the TiC matrix for Ferro-TiC and base element iron for all the alloys in as-received and corroded conditions are given in Table 3.7.

### 3.2.2.3. Optical and SEM studies:

The SEM micrographs of the corroded surfaces of these alloys at different magnifications are shown in Figure 3.21. The micrographs for Fe-5Cu-0.5C show greater corrosion attack as compared to Fe-0.5C. The surfaces of ASP 23 and ASP 30 steels are not much affected.

## 3.3. Superalloys:

### 3.3.1. Corrosion in $H_2SO_4$ medium:

#### 3.3.1.1. Anodic Polarization studies:

Results of potentiodynamic polarization studies, carried out on both the superalloys in  $H_2SO_4$  media are presented in Figures 3.22 - 3.23 and Table 3.9. With increase in concentration of  $H_2SO_4$ , the first increase in  $E_{corr}$  value corresponds to 2N, followed by a second increase at 5N in case of MA 956, and a decrease at 5N in case of MA 754. With increase in concentration of  $H_2SO_4$ , increase in  $I_{corr}$  value corresponds to 2N, followed by further decrease in case of MA 956 and a second increase at 5N for MA 754.

Figure 3.22 also shows some typical anodic polarization curves of MA 956 in various  $H_2SO_4$  concentrations. Curves for 0.1N shows active, passive, and transpassive regions. The additional feature of curves for 1N and 5N are pre-passive region and secondary passive region respectively. Figure 3.23 shows the anodic polarization curves for MA 754. Curves for 0.1N shows active, passive, and transpassive regions. The additional feature of curves for 1N and 5N is the pre-passive region. For the sake of convenience, corrosion rates of both the alloys with respect to  $H_2SO_4$  concentration are plotted in Figure 3.24 from the data given in Table 3.9. A comparison of the two superalloys does not convey any clear cut relationship. The trend is similar to the variation of  $I_{corr}$  value with the  $H_2SO_4$  concentration.

### **3.3.1.2. Weight Loss Experiment:**

No wt. loss was obtained for both the superalloys even after 600 hrs of exposure, showing good corrosion resistance offered by both the superalloys.

### **3.3.1.3. X-ray diffraction studies:**

The lattice parameters for the base elements, i.e. iron and nickel of as-received and corroded surfaces of both the alloys are given in Table 3.10.

### **3.3.1.4. SEM studies:**

The SEM micrographs of the corroded surfaces of both the alloys are shown in Figure 3.25. The corroded surfaces correspond to 2N H<sub>2</sub>SO<sub>4</sub>. The surface of Fe-base superalloy MA 956 is more affected compared to Ni-base superalloy MA 754.

## **3.3.2. Corrosion in 0.6N NaCl:**

### **3.3.2.1. Anodic Polarization studies:**

Results of potentiodynamic anodic polarization studies, carried out on these alloys in 0.6N NaCl solution are presented in Figure 3.26 and Table 3.11. The curve for MA 754 shows clearly the active, passive, and transpassive regions. The corrosion rate for MA 956 is greater than that of MA 754. The former shows pitting corrosion to a greater extent.

### **3.3.2.2. X-ray diffraction studies:**

The lattice parameters for the base elements, i.e. iron and nickel of as-received and corroded surfaces of both the alloys are given in Table 3.10.

### **3.3.2.3. SEM studies:**

The SEM micrographs of the corroded surfaces of both the alloys are shown in Figure 3.27. In case of Fe-base superalloy MA 956, corrosion pits on the surface are formed.

### **3.4. Boride based cermets:**

#### **3.4.1. Corrosion in H<sub>2</sub>SO<sub>4</sub> medium:**

##### **3.4.1.1. Anodic Polarization studies:**

Results of potentiodynamic polarization studies, carried out on both the cermets (sintered in hydrogen and vacuum) in H<sub>2</sub>SO<sub>4</sub> media are presented in Figures 3.28 - 3.29 and Table 3.12. Increase in both  $E_{\text{corr}}$  and  $I_{\text{corr}}$  values correspond to 1N H<sub>2</sub>SO<sub>4</sub> in case of cermet sintered in hydrogen. The sharp increase in both  $E_{\text{corr}}$  and  $I_{\text{corr}}$  values was observed in the case of cermet sintered in vacuum. Figure 3.28 shows the anodic polarization curves for the cermet sintered in hydrogen, where the plots for 1N and 3N show close similarity in the behaviour. Similar is the case for 0.1N and 1N for cermets sintered in vacuum (Figure 3.29). For sake of convenience corrosion rates for both the cermets with respect to H<sub>2</sub>SO<sub>4</sub> concentration are plotted in Figure 3.30, from the data given in Table 3.12. The trend is similar to the variation of  $I_{\text{corr}}$  value with the H<sub>2</sub>SO<sub>4</sub> concentration.

##### **3.4.1.2. X-ray diffraction studies:**

X-ray study was able to detect the phases Mo<sub>2</sub>FeB<sub>2</sub>, Fe<sub>2</sub>B and Fe. The lattice parameter variations for the hard phase Mo<sub>2</sub>FeB<sub>2</sub> are given in Table 3.13. From this it is evident that the boride based cermet sintered in hydrogen is having relatively high lattice distortion as compared to the cermet sintered in vacuum.

##### **3.4.1.3. Optical and SEM studies:**

The optical micrograph of etched surface of the cermet is shown in Figure 3.31. The SEM micrographs of the corroded surfaces of the cermets tested in 5N H<sub>2</sub>SO<sub>4</sub> are shown in Figure 3.32. The surface of the cermet

sintered in hydrogen is attacked to a greater extent'as compared to the cermet sintered in vacuum.

### **3.4.2. Corrosion in 0.6N NaCl:**

Results of potentiodynamic anodic polarization studies, carried out on these cermets in 0.6N NaCl solution are presented in Figure 3.33 and Table 3.14. Both the curves show active and passive regions. The corrosion rate of cermet sintered in hydrogen is higher as compared to the cermet sintered in vacuum.

Table 3.1 Anodic polarization characteristics of Al- and Cu- based alloys in  $H_2SO_4$  medium.

Alloy	Concentration of $H_2SO_4$	$E_{corr}$ (mV)	$I_{corr}$ ( $\mu A/cm^2$ )	Corrosion rate	
				mpy	mmpy
RS 7091 aluminium	0.1N	-415.5	10.02	4.525	0.114
	1N	-428.8	20.95	9.460	0.240
	2N	-512.8	57.75	26.08	0.662
	3N	-520.8	31.73	14.33	0.363
	5N	-496.7	32.96	14.88	0.378
DISPAL	0.1N	-462.0	8.731	3.801	0.0965
	1N	17.18	66.23	28.84	0.7324
	2N	-523.9	30.86	13.44	0.341
	3N	-638.8	95.54	41.60	1.057
	5N	-651.3	233.1	101.5	2.577
ODS copper	0.1N	-29.81	36.83	16.80	0.426
	1N	-55.58	84.00	38.33	0.9735
	2N	-3.703	168.2	76.75	1.949
	3N	-70.68	5.926	2.704	0.068
	5N	52.96	34.15	15.58	0.395



Table 3.2 Results of wt. loss experiment for Al- and Cu- based alloys.

Alloy	Exposure Time (hr)	Wt. loss/area (mgs/sq.in)	Corrosion Rate (mpy)
RS 7091 aluminium	120	92.03	145.75
	240	204.65	162.05
	360	332.88	175.7
	600	545.07	172.6
DISPAL	120	39.71	66.44
	240	89.99	75.27
	360	162.96	90.87
	600	325.76	109
ODS copper	120	11.32	5.62
	240	26.47	6.57
	360	40.19	6.65
	600	151.2	15.02

Table 3.3 Lattice parameter (nm) variation of the matrix element of as-received and corroded ferrous alloys in different media.

Alloy	As-received condition	Corroded condition	
		5N H <sub>2</sub> SO <sub>4</sub>	0.6N NaCl
RS091 aluminium	0.4050	0.4064	0.4041
DISPAL	0.4048	0.4051	0.4049
ODS copper	0.3615	0.3611	0.3610

Table 3.4 Anodic polarization characteristics of Al- and Cu- based alloys in 0.6N NaCl solution.

Alloy	E <sub>corr</sub> (mV)	I <sub>corr</sub> ( $\mu$ A/cm <sup>2</sup> )	Corrosion rate	
			mpy	mmpy
RS 7091 aluminium	-826.9	3.796	1.557	0.039
DISPAL	-707.8	23.35	10.17	0.258
ODS copper	-247.0	11.61	5.298	0.135

Table 3.5 Anodic polarization characteristics of ferrous alloys in H<sub>2</sub>SO<sub>4</sub> medium.

Alloy	Concentration of H <sub>2</sub> SO <sub>4</sub>	E <sub>corr</sub> (mV)	I <sub>corr</sub> (μA/cm <sup>2</sup> )	Corrosion rate	
				mpy	mmpy
Fe-0.5C	0.1N	-511.6	3629	1993	50.63
	1N	-477.5	9907	5441	92.21
	2N	-467.6	2935	1581	40.17
	3N	-440.2	7325	4023	102.2
	5N	-437.2	3985	2189	55.59
Fe-5Cu-0.5C	0.1N	-492.9	6658	3621	91.96
	1N	-456.6	15670	8522	216.5
	2N	-448.4	5220	2839	72.10
	3N	-439.6	6852	3726	94.64
	5N	-425.1	4602	2503	63.57
ASP 23	0.1N	-515.3	39.89	15.14	0.382
	1N	-469.4	1007	382.0	9.704
	2N	-462.7	1502	570.0	14.48
	3N	-437.9	1677	634.4	16.17
	5N	-441.9	2076	788.1	20.02
ASP 30	0.1N	-456.7	70.01	23.86	0.606
	1N	-426.7	231.6	78.94	2.005
	2N	-420.9	311.5	106.2	2.697
	3N	-414.7	382.6	123.2	3.129
	5N	-409.9	410.7	140.0	3.556
Ferro-TiC	0.1N	-514.0	103.8	43.92	1.116
	1N	-443.9	15.65	8.735	0.221
	2N	-434.8	19420	8390	213.3
	3N	-439.9	8379	3622	92.0
	5N	-429.1	4381	1889	47.97

Table 3.6 Results of wt. loss experiment for Tool Steels.

Alloy	Exposure Time (hr)	Wt. loss/area (mgs/sq.in)	Corrosion Rate (mpy)
ASP 23	120	927.39	483.24
	240	1351.18	352.03
	360	1777.89	308.80
	600	3184.95	331.92
ASP 30	120	909.56	469.0
	240	1315.83	339.25
	360	1766.46	303.59
	600	2763.42	284.98

Table 3.7 Lattice parameter (nm) variation of the matrix element of as-received and corroded ferrous alloys in different media.

Alloy	As-received condition	Corroded condition	
		5N H <sub>2</sub> SO <sub>4</sub>	0.6N NaCl
Fe-0.5C	0.2870	0.2866	0.2867
Fe-5Cu-0.5C	0.2876	0.2873	0.2872
ASP 23	0.2870	0.2866	0.2864
ASP 30	0.2883	0.2796	0.2899
Ferro-TiC	0.2887	0.4307 (FeO)	0.4321 (FeO)
	(Ferrous matrix)	0.4310 (TiO)	0.4306 (TiO)
	0.4325 (TiC)		

Table 3.8 Anodic polarization characteristics of ferrous alloys in 0.6N NaCl solution.

Alloy	$E_{\text{corr}}$ (mV)	$I_{\text{corr}}$ ( $\mu\text{A}/\text{cm}^2$ )	Corrosion rate	
			mpy	mmpy
Fe-0.5C	-494.0	43.05	23.65	0.600
Fe-5Cu-0.5C	-541.5	86.28	46.92	1.192
ASP 23	-574.3	7.595	2.883	0.073
ASP 30	-552.1	5.890	2.008	0.051
Ferro-TiC	-512.9	24.76	10.70	0.271

Table 3.9 Anodic polarization characteristics of the superalloys in H<sub>2</sub>SO<sub>4</sub> medium.

Alloy	Concentration of H <sub>2</sub> SO <sub>4</sub>	E <sub>corr</sub> (mV)	I <sub>corr</sub> (μA/cm <sup>2</sup> )	Corrosion rate	
				mpy	mmpy
Fe-base superalloy MA 956	0.1N	-61.08	2.301	1.104	0.028
	1N	-94.92	0.5972	0.286	0.0072
	2N	57.25	21.84	7.186	0.182
	3N	7.875	1.265	0.606	0.015
	5N	30.80	0.757	0.363	0.0092
Ni-base superalloy MA 754	0.1N	-85.68	2.420	1.069	0.027
	1N	-119.7	1.698	0.749	0.019
	2N	-46.45	1.946	0.858	0.021
	3N	58.73	0.234	0.103	0.0026
	5N	-221.3	1.341	0.591	0.015

Table 3.10 Lattice parameter (nm) variation of the matrix element of as-received and corroded superalloys in different media.

Alloy	As-received condition	Corroded condition	
		2N H <sub>2</sub> SO <sub>4</sub>	0.6N NaCl
Fe-base superalloy matrix	0.2890	0.2883	0.3171
Ni-base superalloy matrix	0.3558	0.3550	0.3558

Table 3.11 Anodic polarization characteristics of the superalloys in 0.6N NaCl solution.

Alloy	E <sub>corr</sub> (mV)	I <sub>corr</sub> (μA/cm <sup>2</sup> )	Corrosion rate	
			mpy	mmpy
Fe-base superalloy MA 956	-219.9	0.468	0.248	0.0058
Ni-base superalloy MA 754	-341.5	0.308	0.135	0.0034

Table 3.12 Anodic polarization characteristics of ternary boride based cermet in H<sub>2</sub>SO<sub>4</sub> medium.

Sintering atmosphere	Concentration of H <sub>2</sub> SO <sub>4</sub>	E <sub>corr</sub> (mV)	I <sub>corr</sub> (μA/cm <sup>2</sup> )	Corrosion rate	
				mpy	mmpy
Hydrogen	0.1N	-354.6	74.27	42.50	1.079
	1N	-287.2	181.8	104.1	2.643
	3N	-286.0	61.20	35.02	0.889
Vacuum	0.1N	-26.64	0.702	0.302	0.0076
	1N	33.00	4.295	1.848	0.046
	3N	74.26	7.744	3.333	0.084

Table 3.13 Lattice parameter (nm) of ternary boride in as-sintered and corroded conditions in 5N H<sub>2</sub>SO<sub>4</sub>.

Sintering atmosphere	As-sintered condition		Corroded condition	
	a	c	a	c
Hydrogen	0.5677	0.3127	0.5633	0.3116
Vacuum	0.5677	0.3127	0.5705	0.3119



Table 3.14 Anodic polarization characteristics of ternary boride based cermet  
in 0.6N NaCl solution.

Sintering atmosphere	$E_{\text{corr}}$ (mV)	$I_{\text{corr}}$ ( $\mu\text{A}/\text{cm}^2$ )	Corrosion Rate	
			mpy	mmpy
Hydrogen	-416.0	16.47	9.427	0.239
Vacuum	-191.9	1.533	0.659	0.016

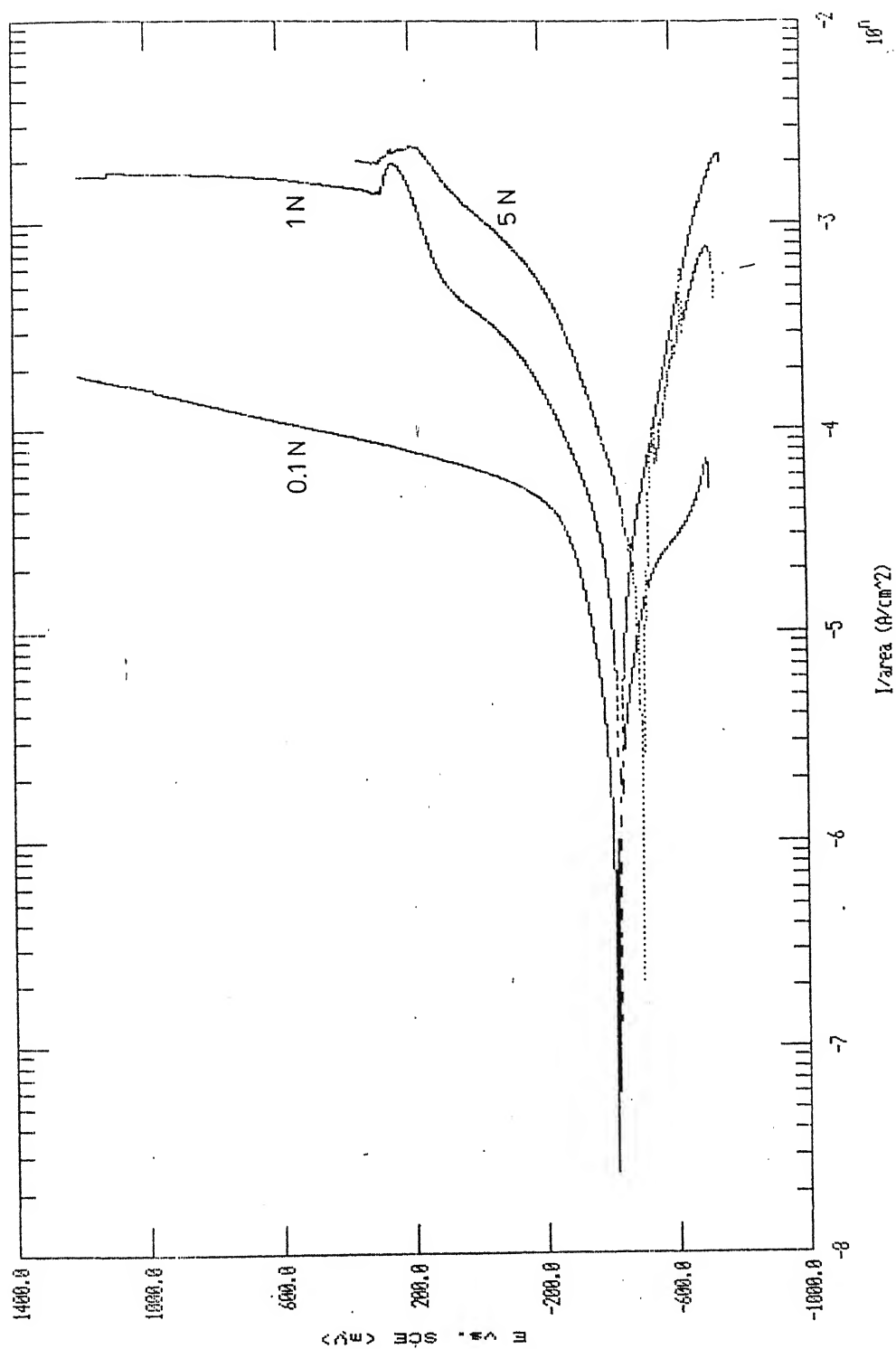


Figure 3.1 Some typical anodic polarization curves of RS 7091 aluminium alloy in  $\text{H}_2\text{SO}_4$  of various concentrations.

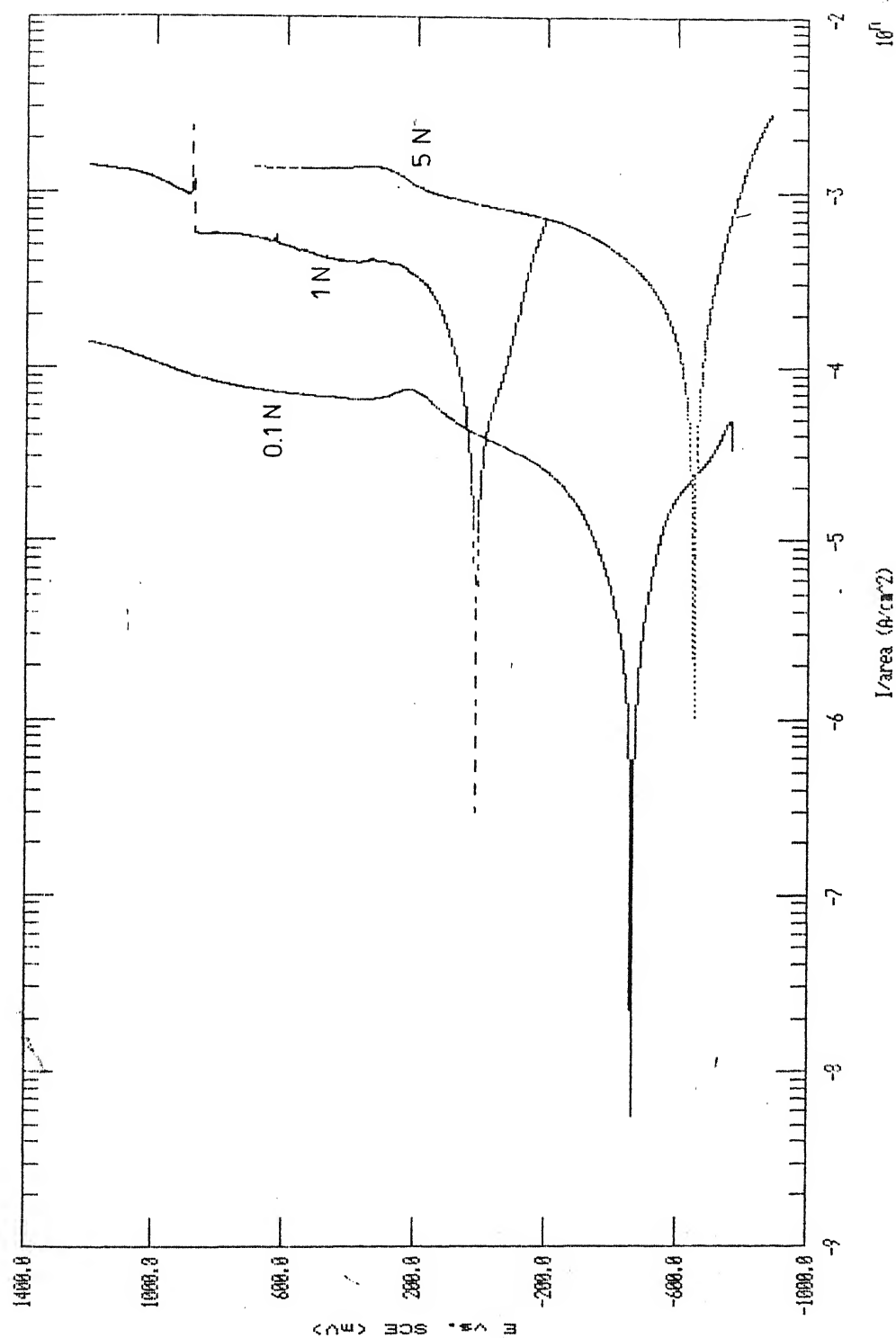


Figure 3.2 Some typical anodic polarization curves of DISPAL in  $\text{H}_2\text{SO}_4$  of various concentrations.

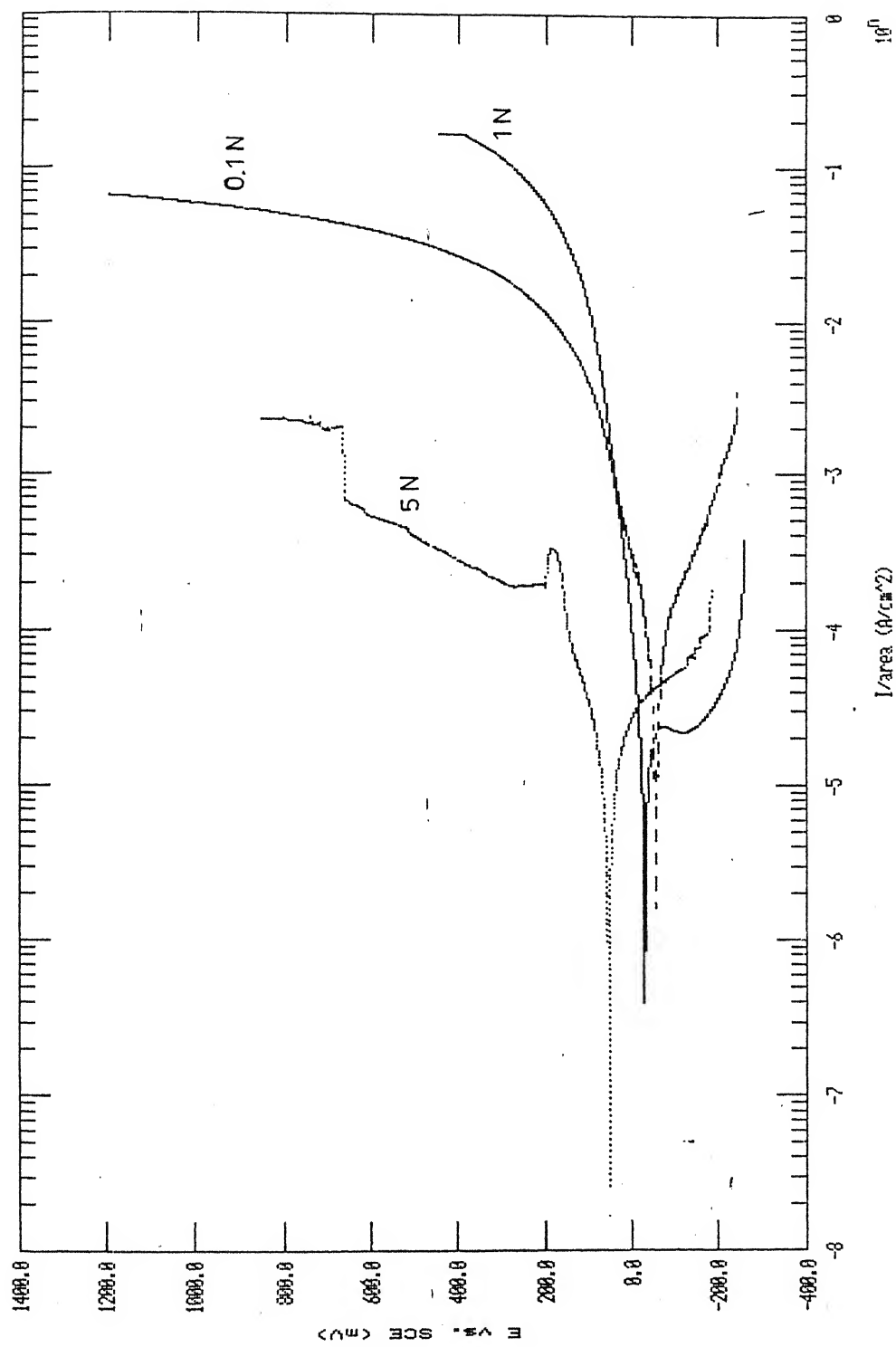


Figure 3.3 Some typical anodic polarization curves of ODS copper in  $\text{H}_2\text{SO}_4$  of various concentrations.

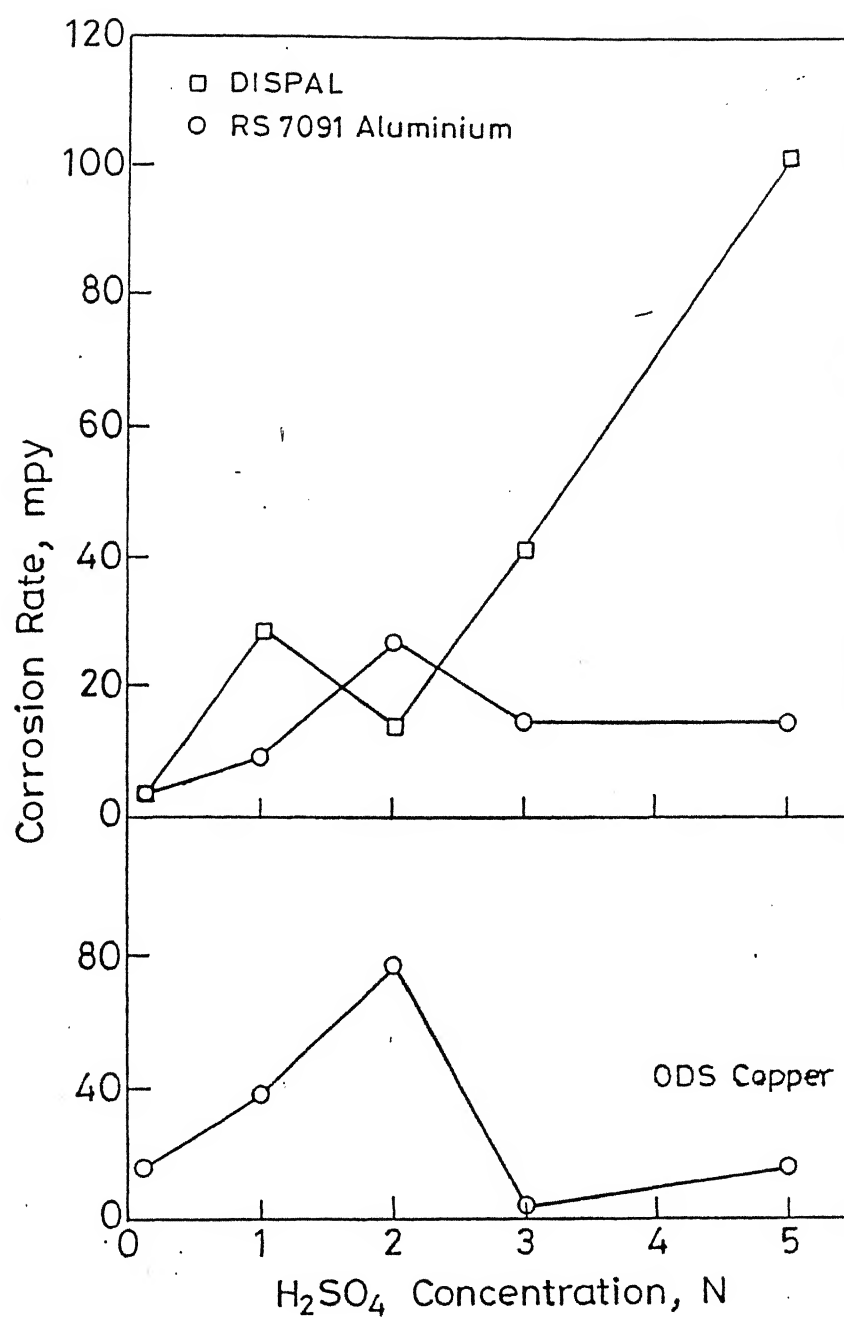


Figure 3.4 Corrosion rate variation of RS 7091 aluminium, DISPAL and ODS copper alloys with respect to  $H_2SO_4$  concentration.

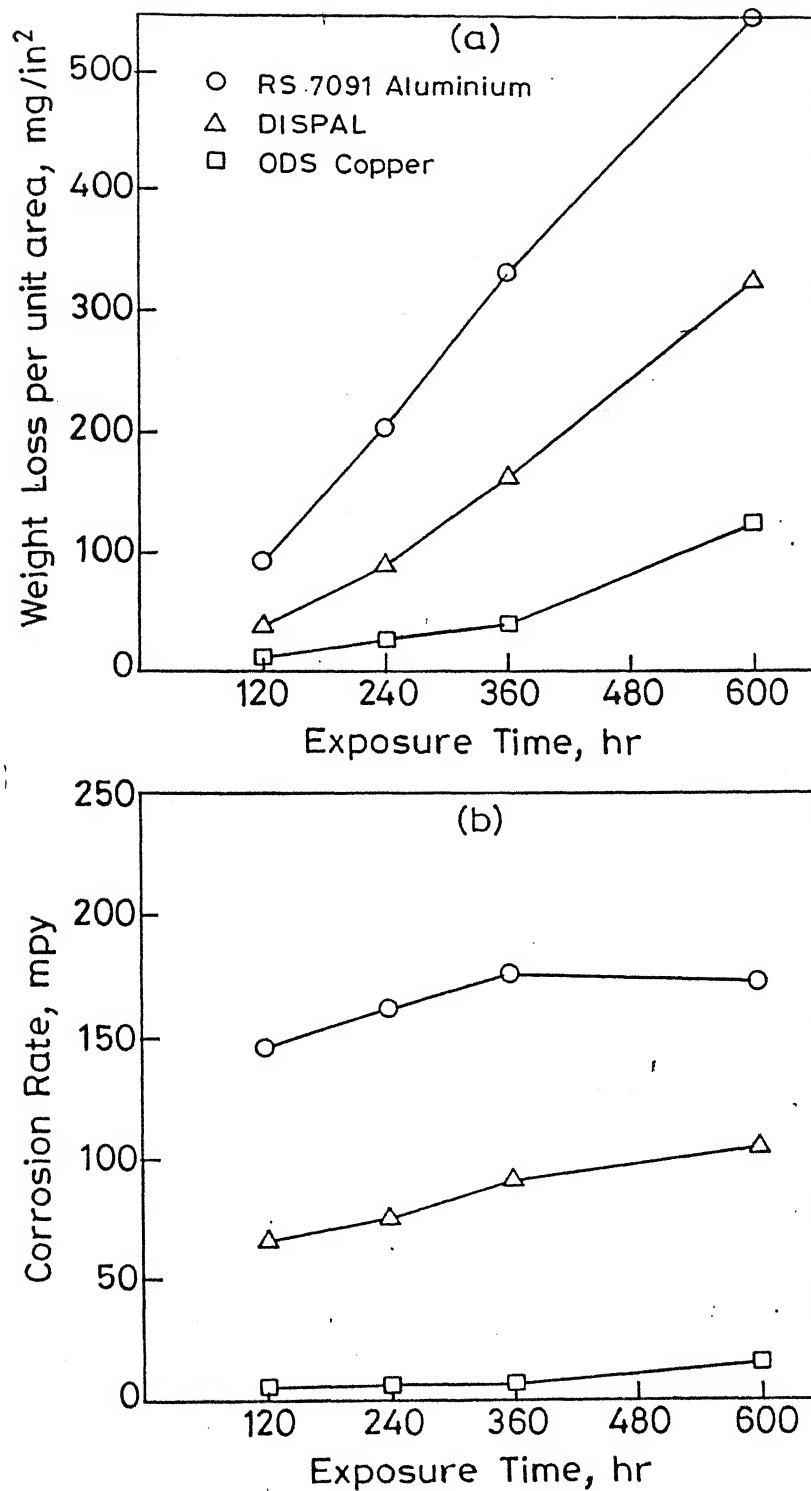


Figure 3.5 Plots obtained for RS 7091 aluminium, DISPAL and ODS copper alloys from wt. loss experiment:

- (a) wt. loss per unit area vs. exposure time
- (b) Corrosion rate vs. exposure time

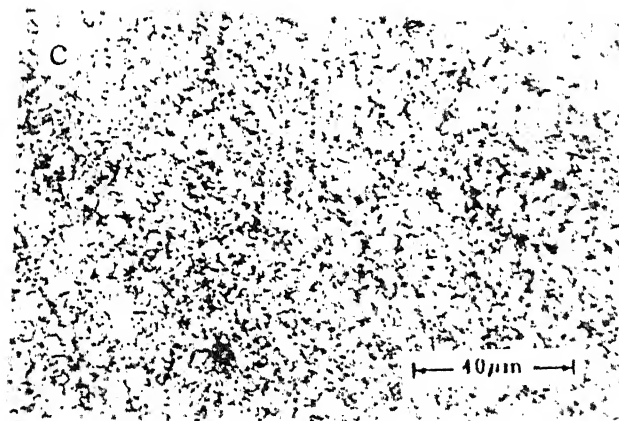
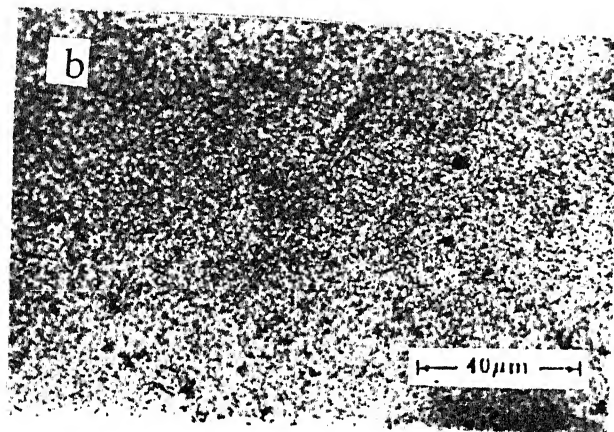


Figure 3.6 Optical micrographs of the as-received alloys:

(a) RS 7091 aluminium (b) DISPAL (c) ODS copper

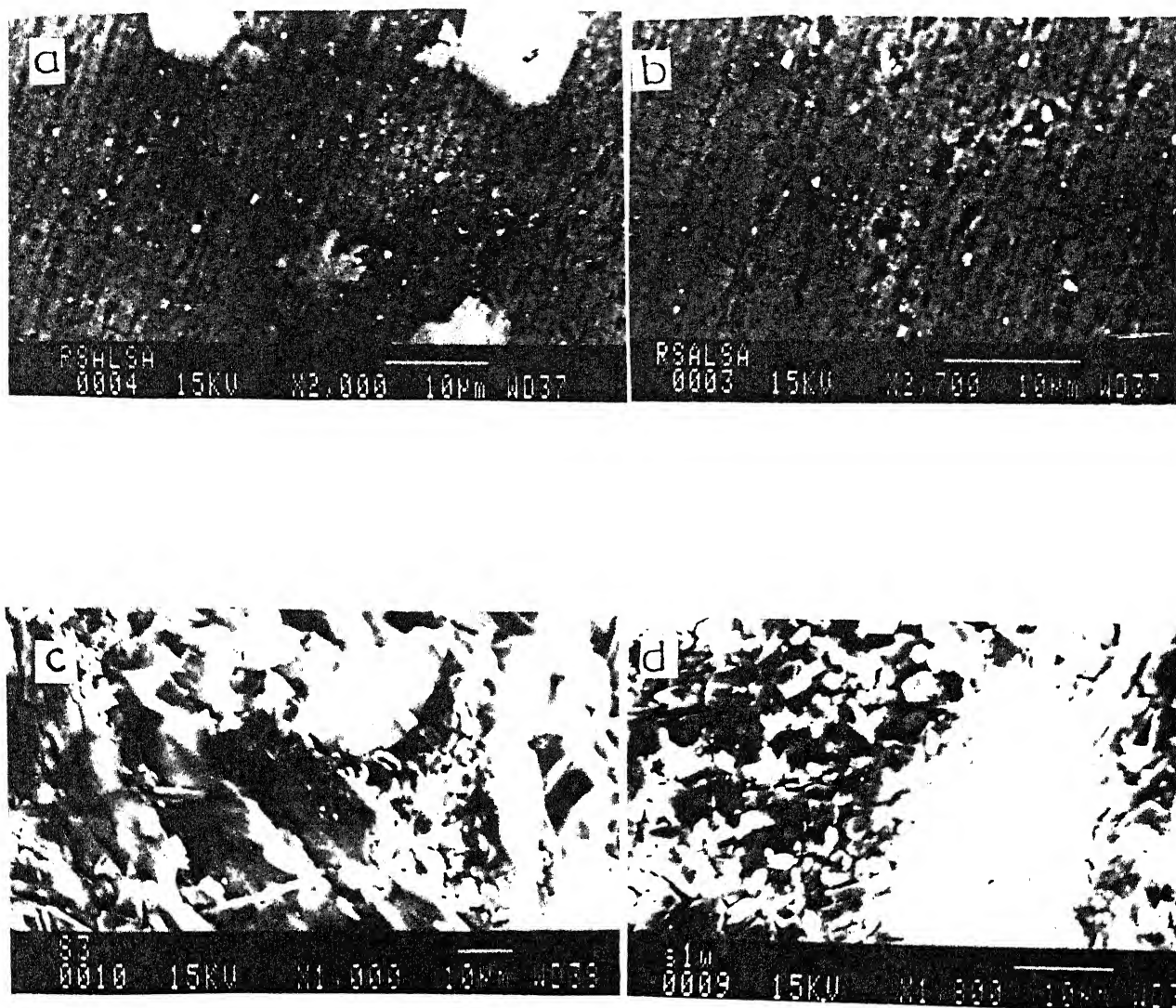


Figure 3.7 SEM micrographs of the corroded surfaces of different alloys tested in 2N  $\text{H}_2\text{SO}_4$ :

- (a)– (b) RS 7091 aluminium alloy at different magnifications
- (c) DISPAL (d) ODS copper



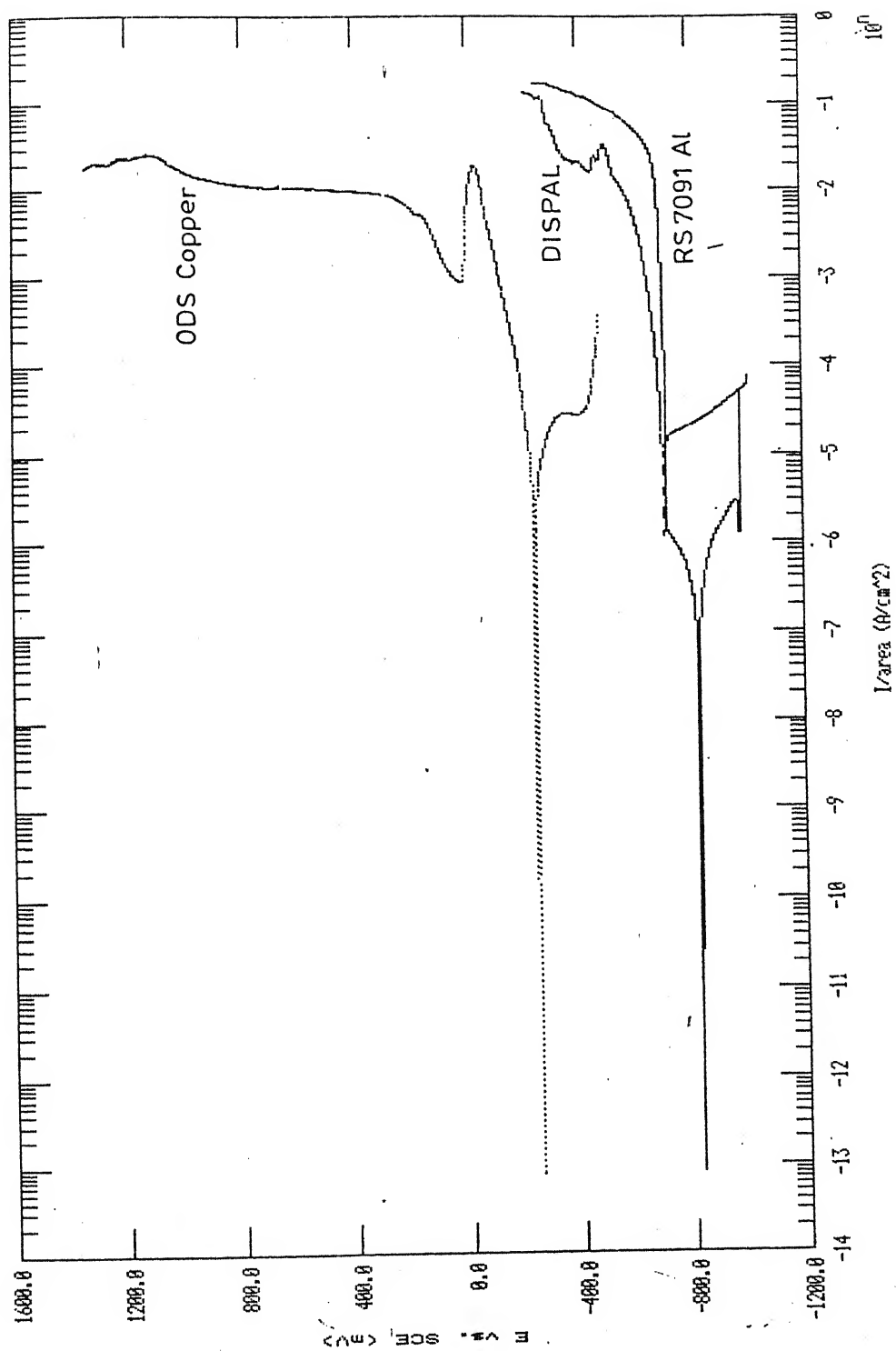


Figure 3.8 Anodic polarization curves of RS 7091 aluminium, DISPAL and ODS copper alloys in 0.6N NaCl solution.

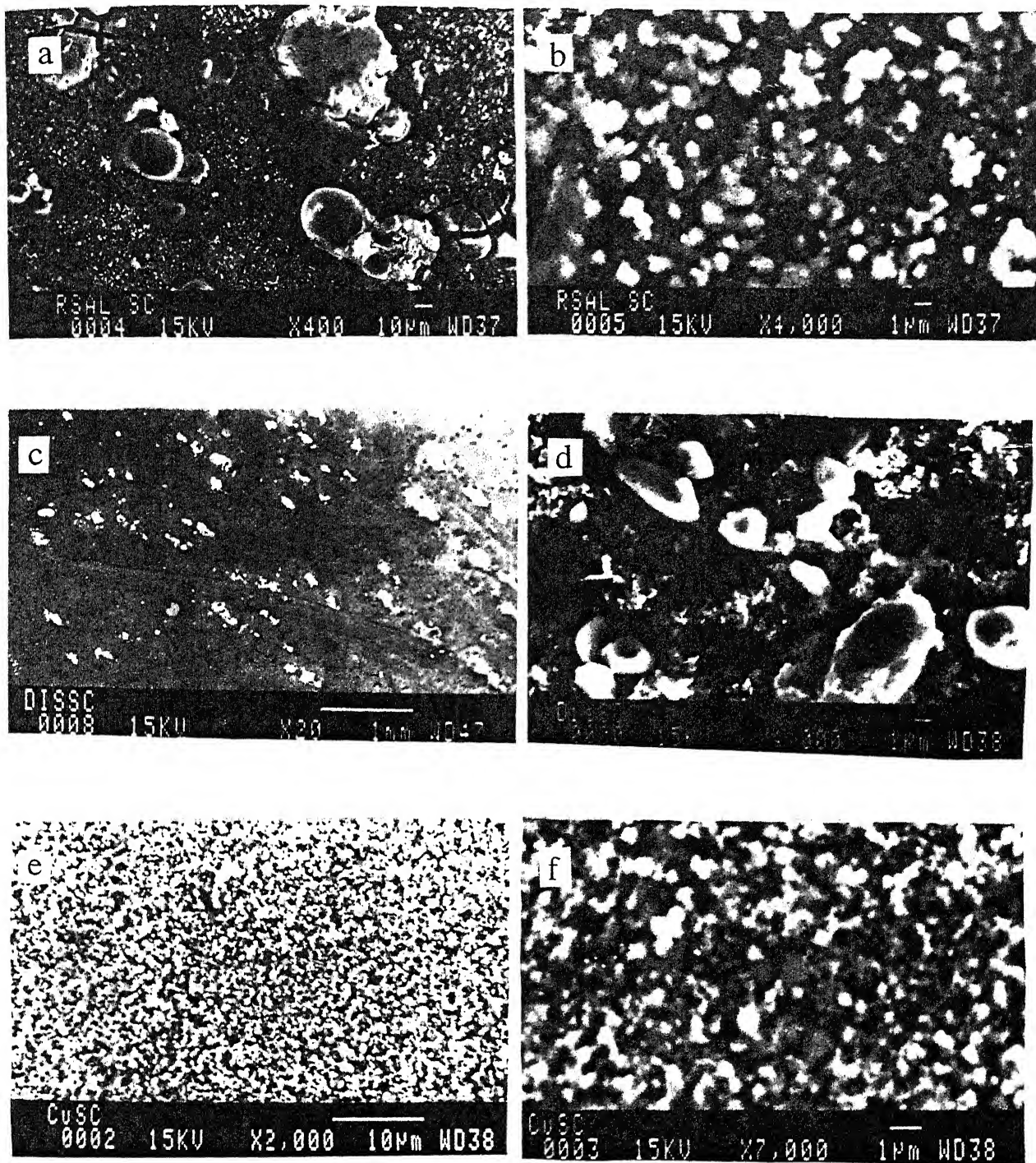


Figure 3.9 SEM micrographs of the corroded surfaces of alloys tested in 0.6N NaCl solution:

- (a) – (b) RS 7091 aluminium at different magnifications
- (c) – (d) DISPAL at different magnifications
- (e) – (f) ODS copper at different magnifications

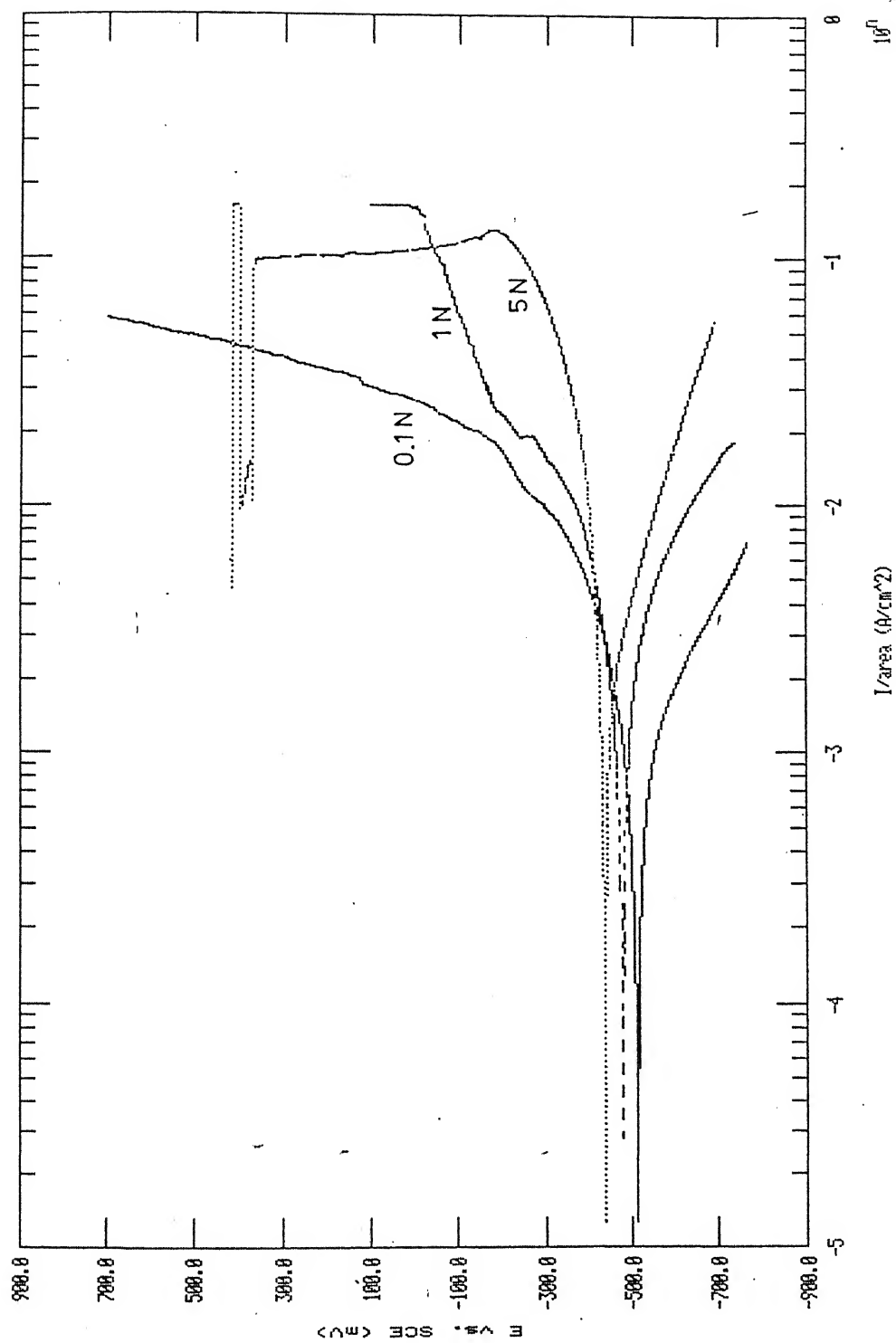


Figure 3.10 Some typical anodic polarization curves of Fe-0.5C steel in  $H_2SO_4$  of various concentrations.

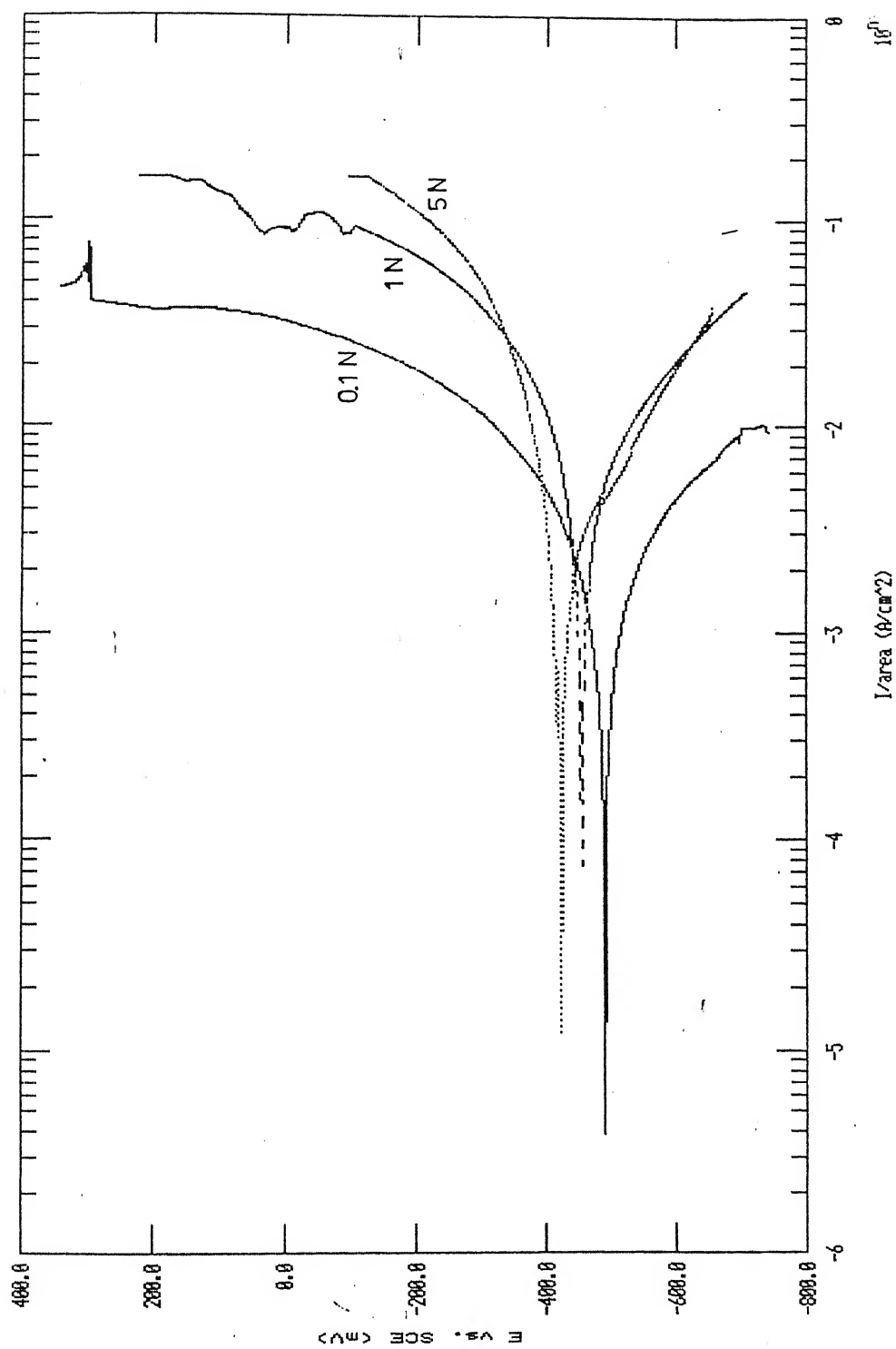


Figure 3.11 Some typical anodic polarization curves of Fe-5Cu-0.5C steel in  $\text{H}_2\text{SO}_4$  of various concentrations.

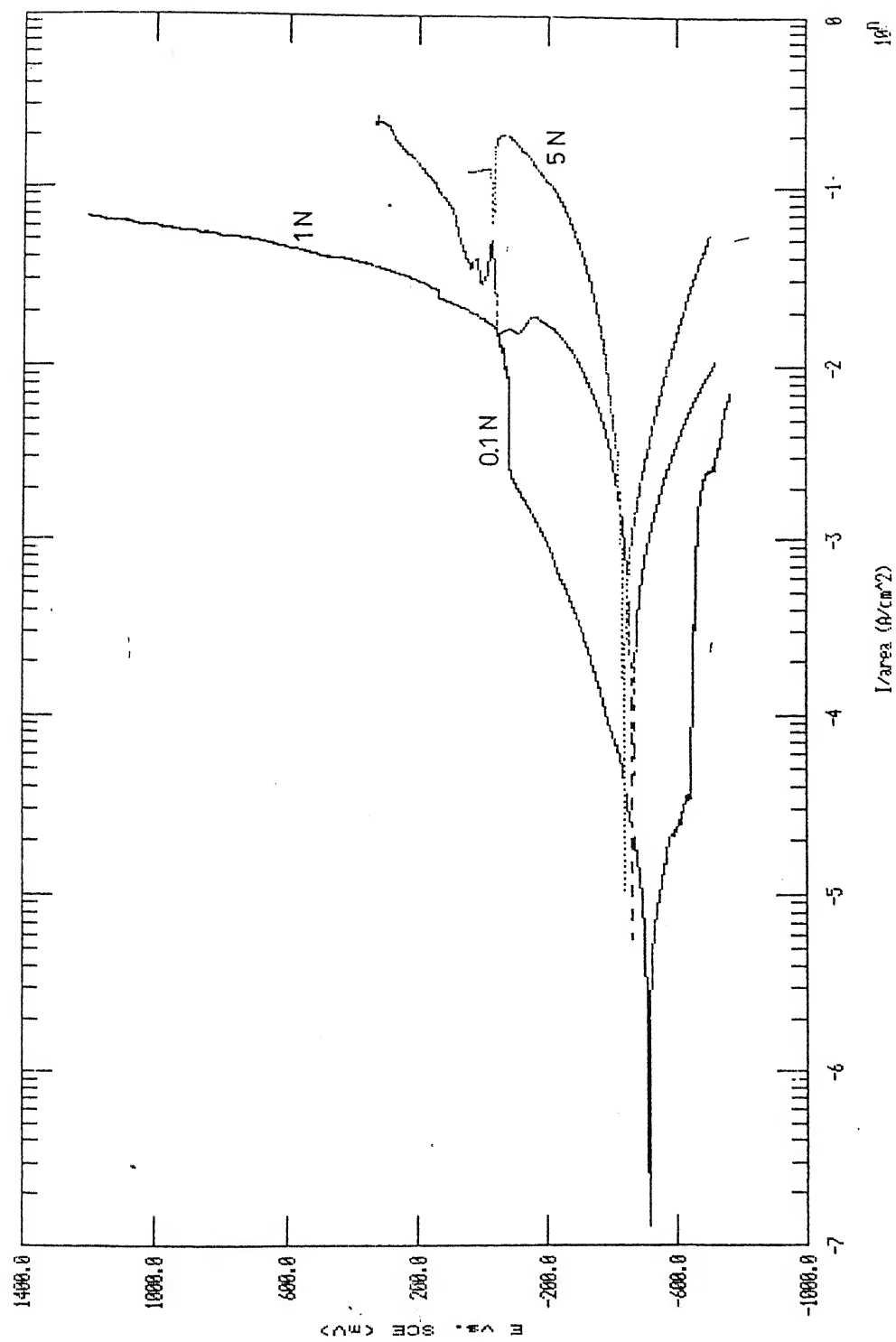


Figure 3.12 Some typical anodic polarization curves of ASP 23 tool steel in  $\text{H}_2\text{SO}_4$  of various concentrations.

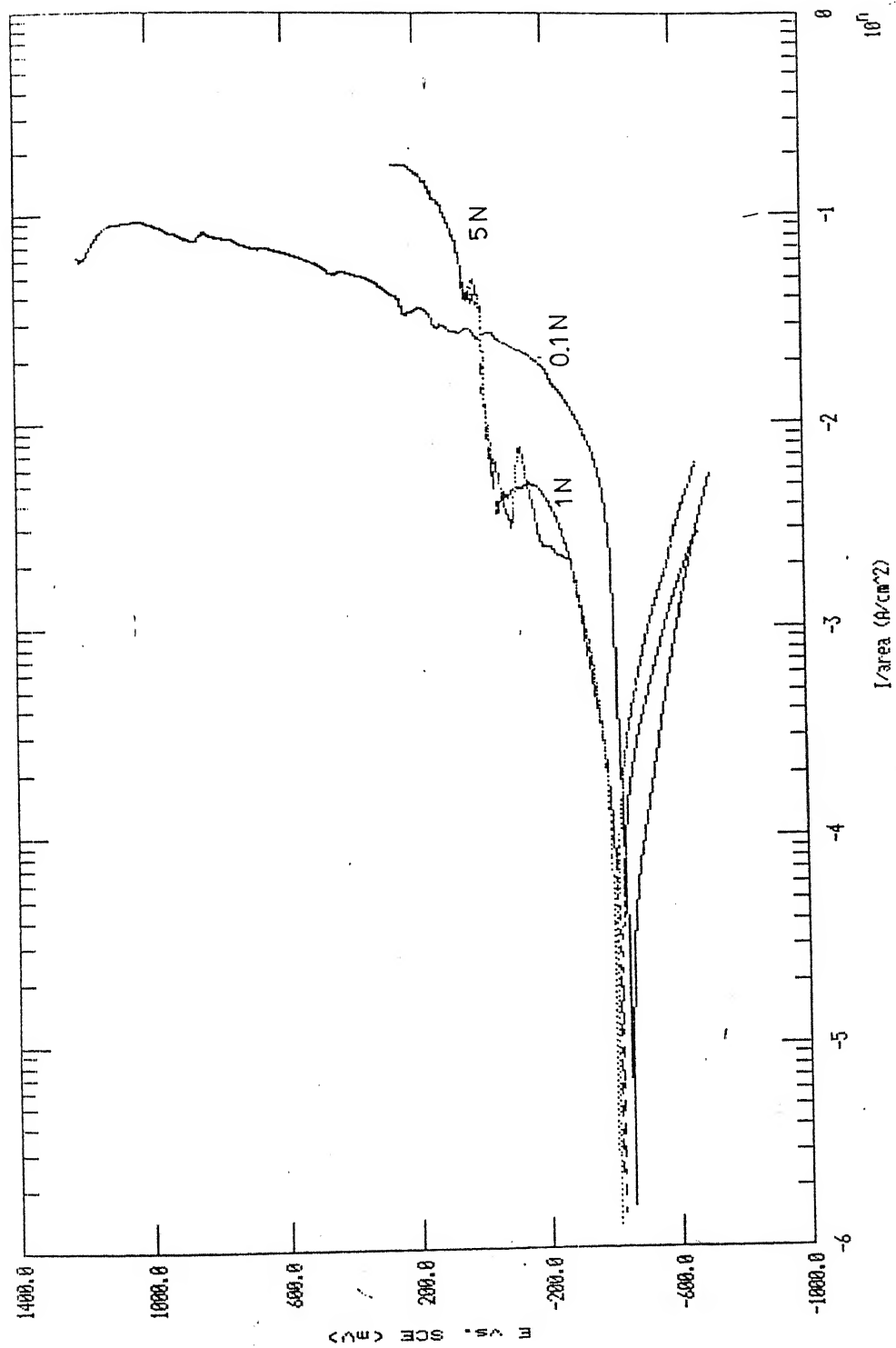


Figure 3.13 Some typical anodic polarization curves of ASP 30 tool steel in  $\text{H}_2\text{SO}_4$  of various concentrations.

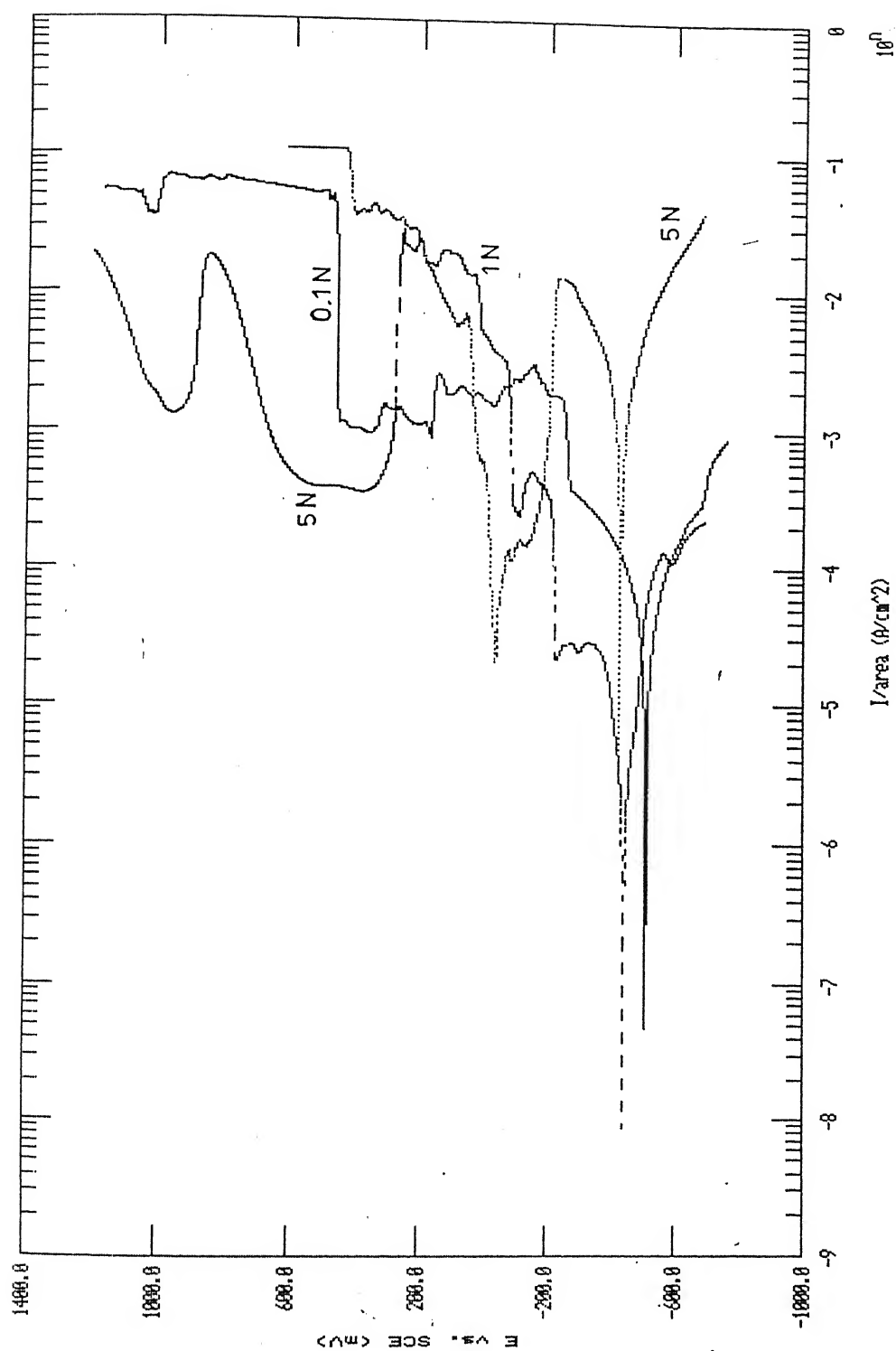


Figure 3.14 Some typical anodic polarization curves of Ferro-TiC in  $\text{H}_2\text{SO}_4$  of various concentrations.

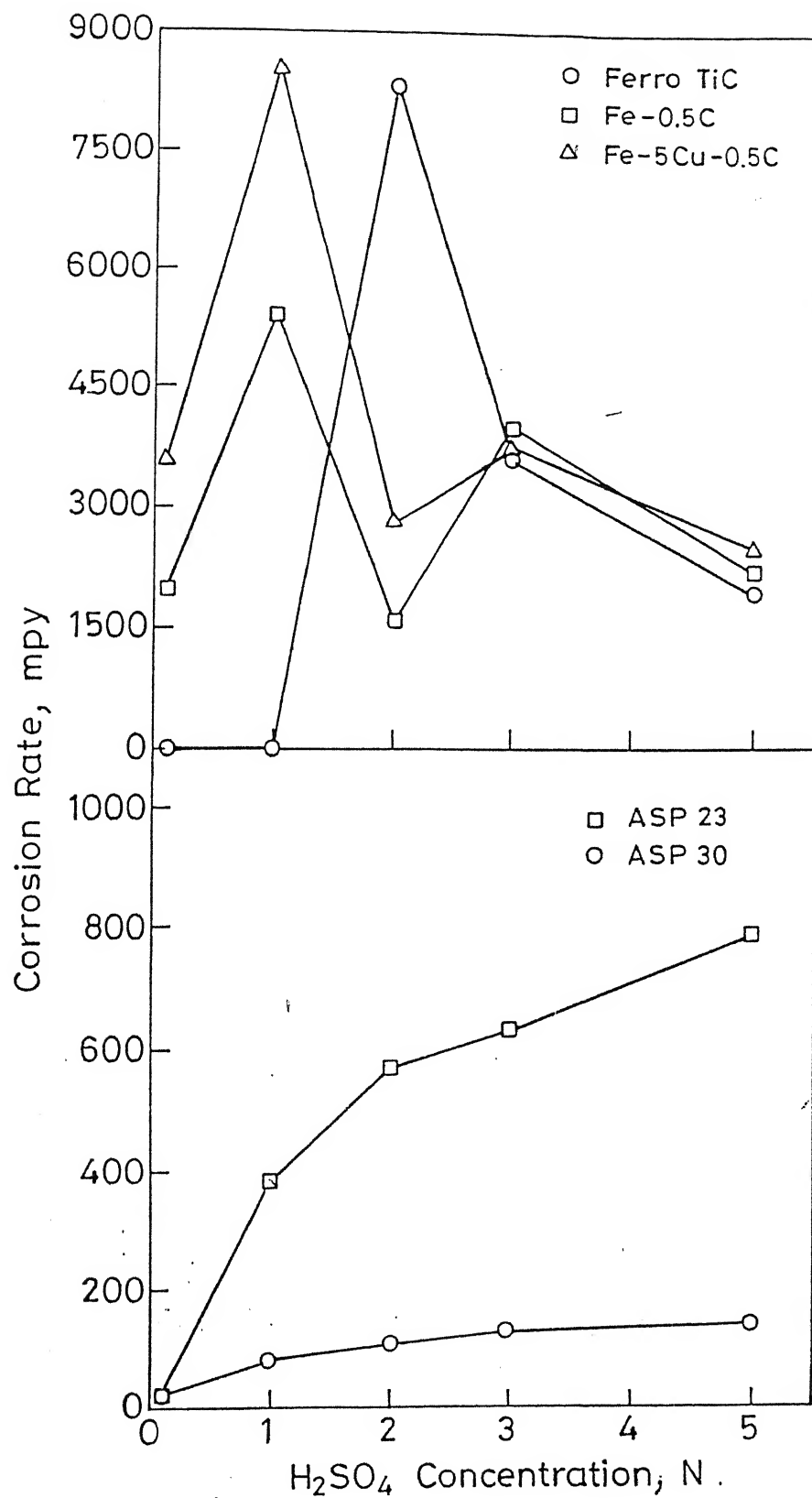


Figure 3.15 Corrosion rate variation of different ferrous alloys with respect to  $H_2SO_4$  concentration.



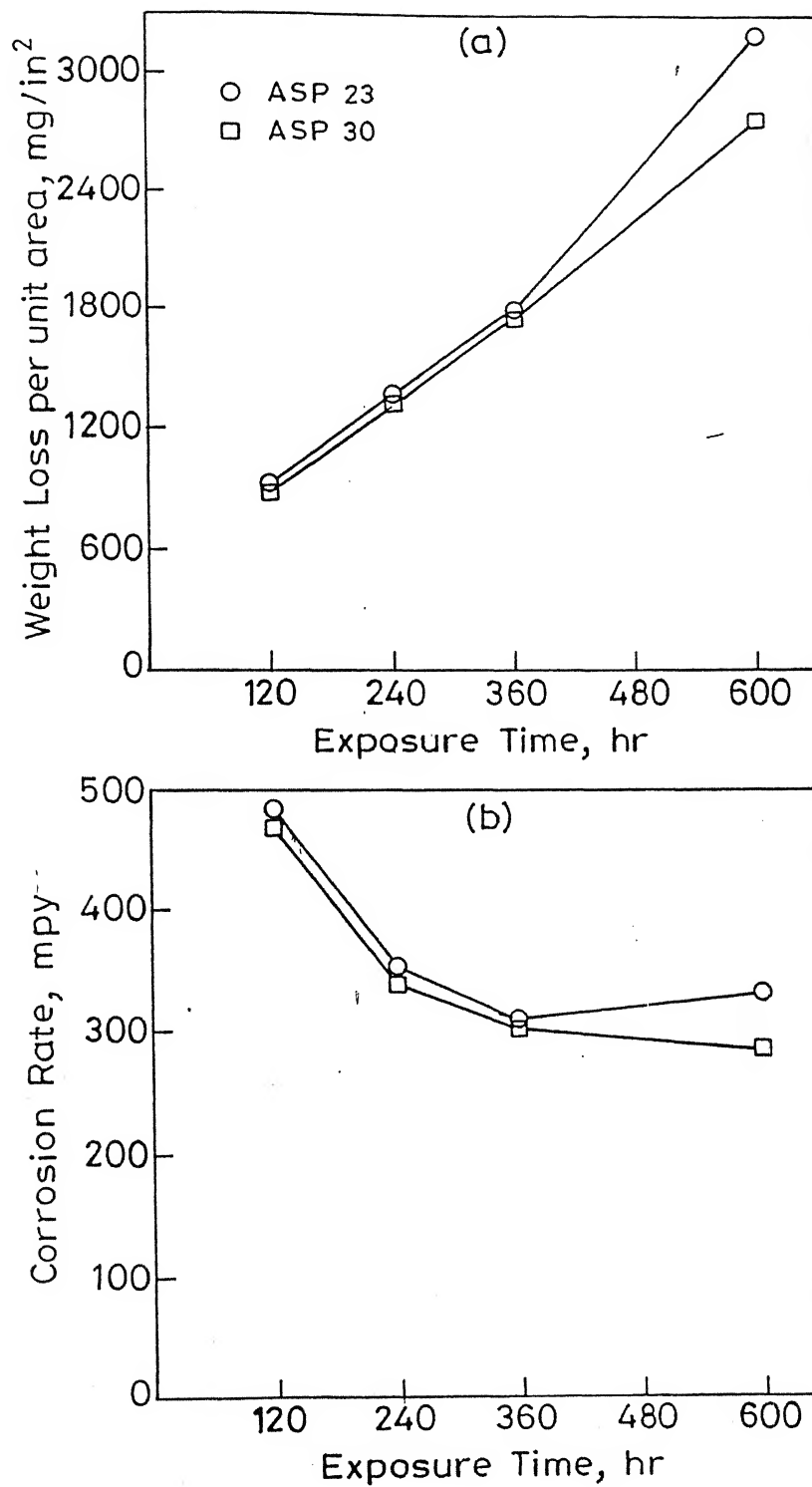


Figure 3.16 Plots obtained for ASP 23 and ASP 30 tool steels from wt. loss experiment:

- (a) wt. loss per unit area vs. exposure time
- (b) Corrosion rate vs. exposure time

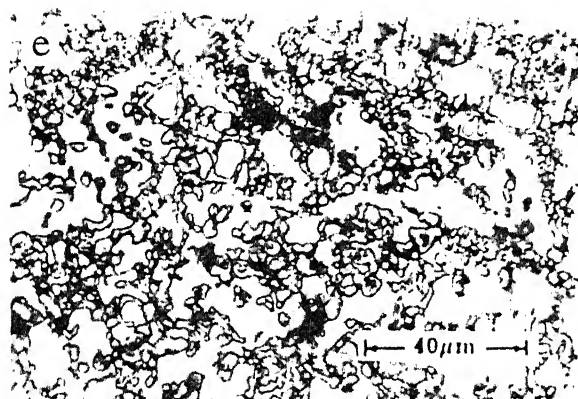
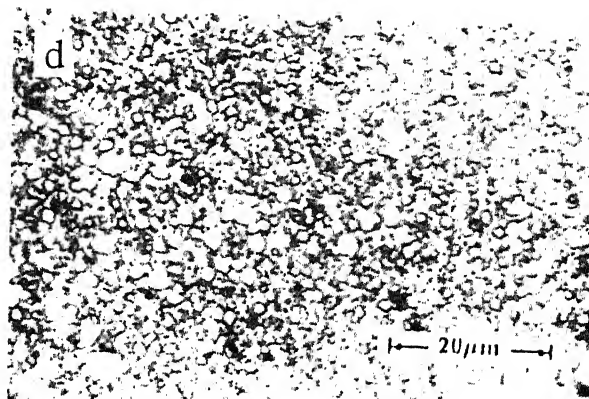
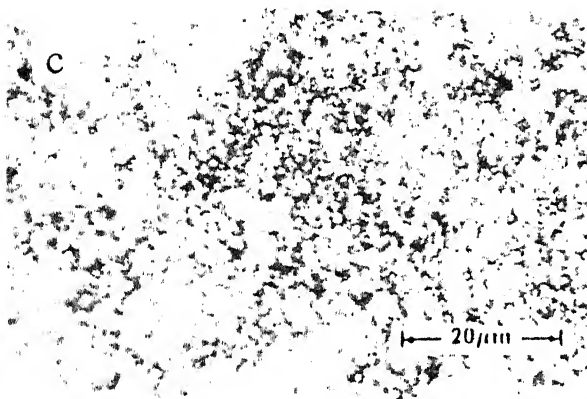
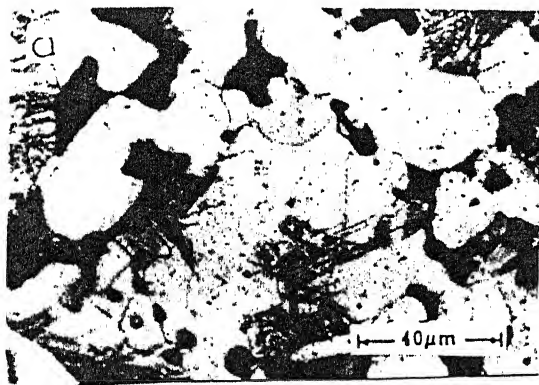


Figure 3.17 Optical micrographs of the as-received ferrous alloys:

- |             |                 |            |
|-------------|-----------------|------------|
| (a) Fe-0.5C | (b) Fe-5Cu-0.5C | (c) ASP 23 |
| (d) ASP 30  | (e) Ferro-TiC   |            |

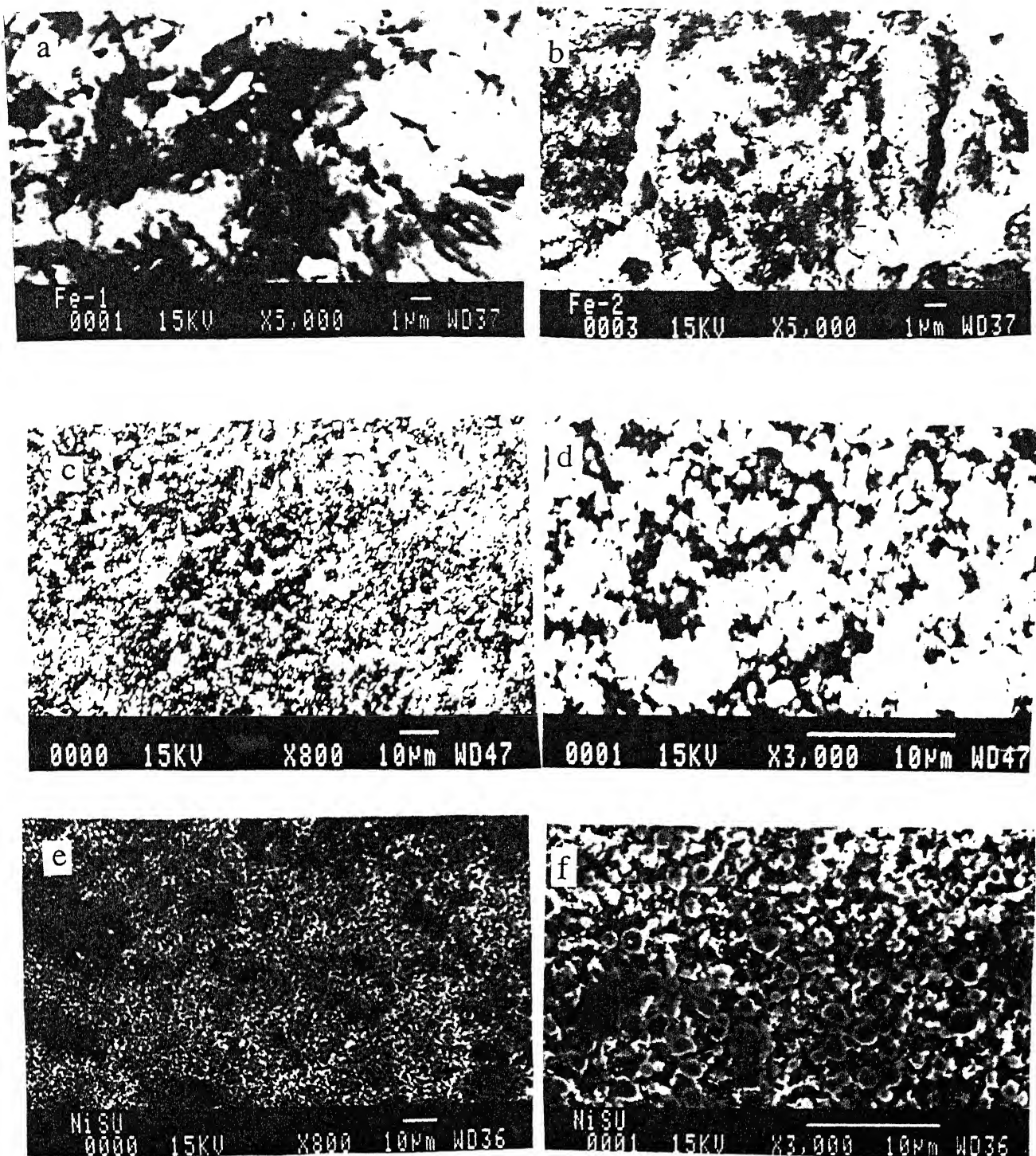


Figure 3.18 SEM micrographs of the corroded surfaces of ferrous alloys tested in 5N  $\text{H}_2\text{SO}_4$ :

- (a) Fe-0.5C                      (b) Fe-5Cu-0.5C
- (c) – (d) ASP 23 at different magnifications
- (e) – (f) ASP 30 at different magnifications

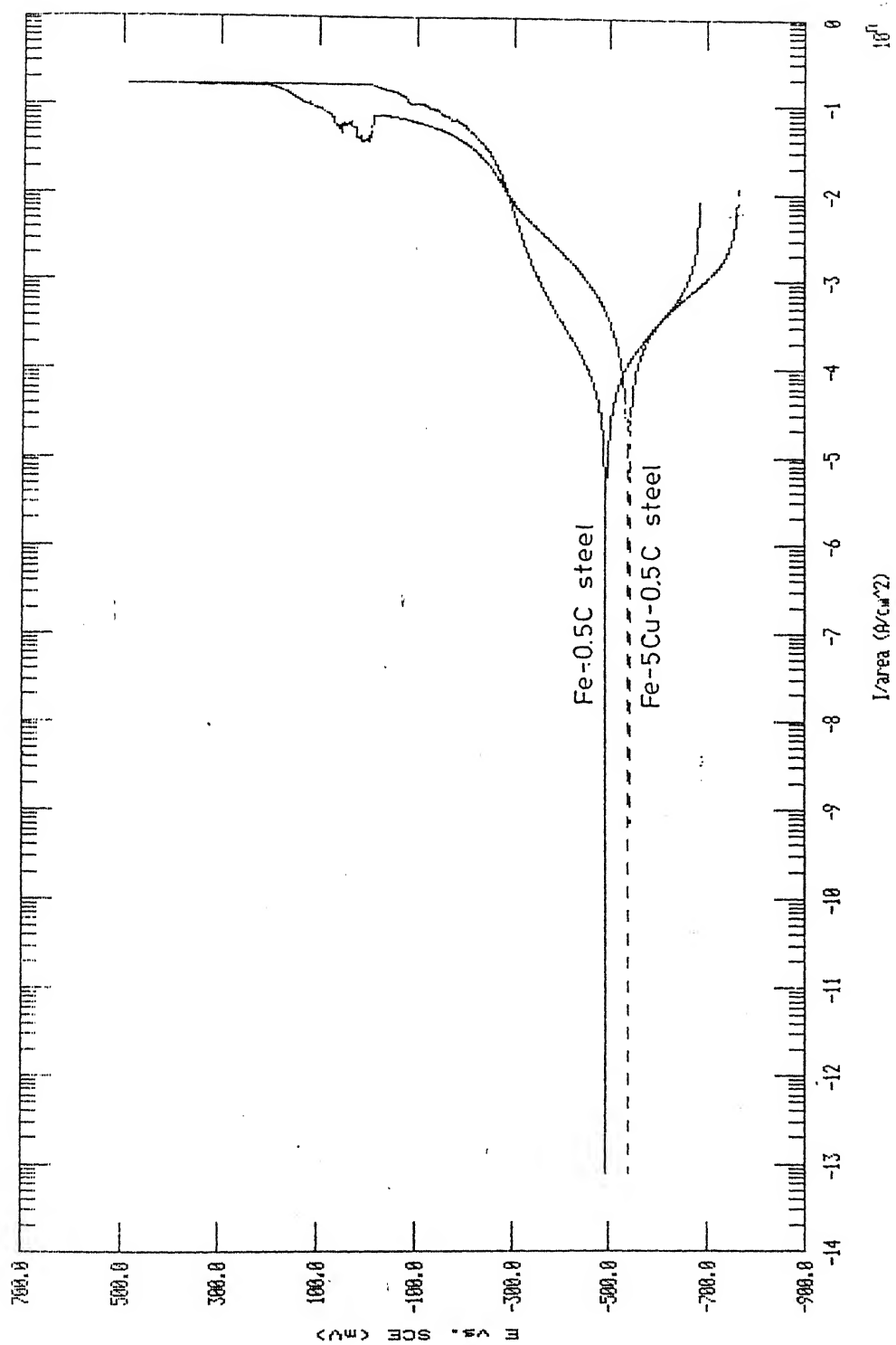


Figure 3.19 Anodic polarization curves of Fe-0.5C and Fe-5Cu-0.5C steels in 0.6N NaCl solution.

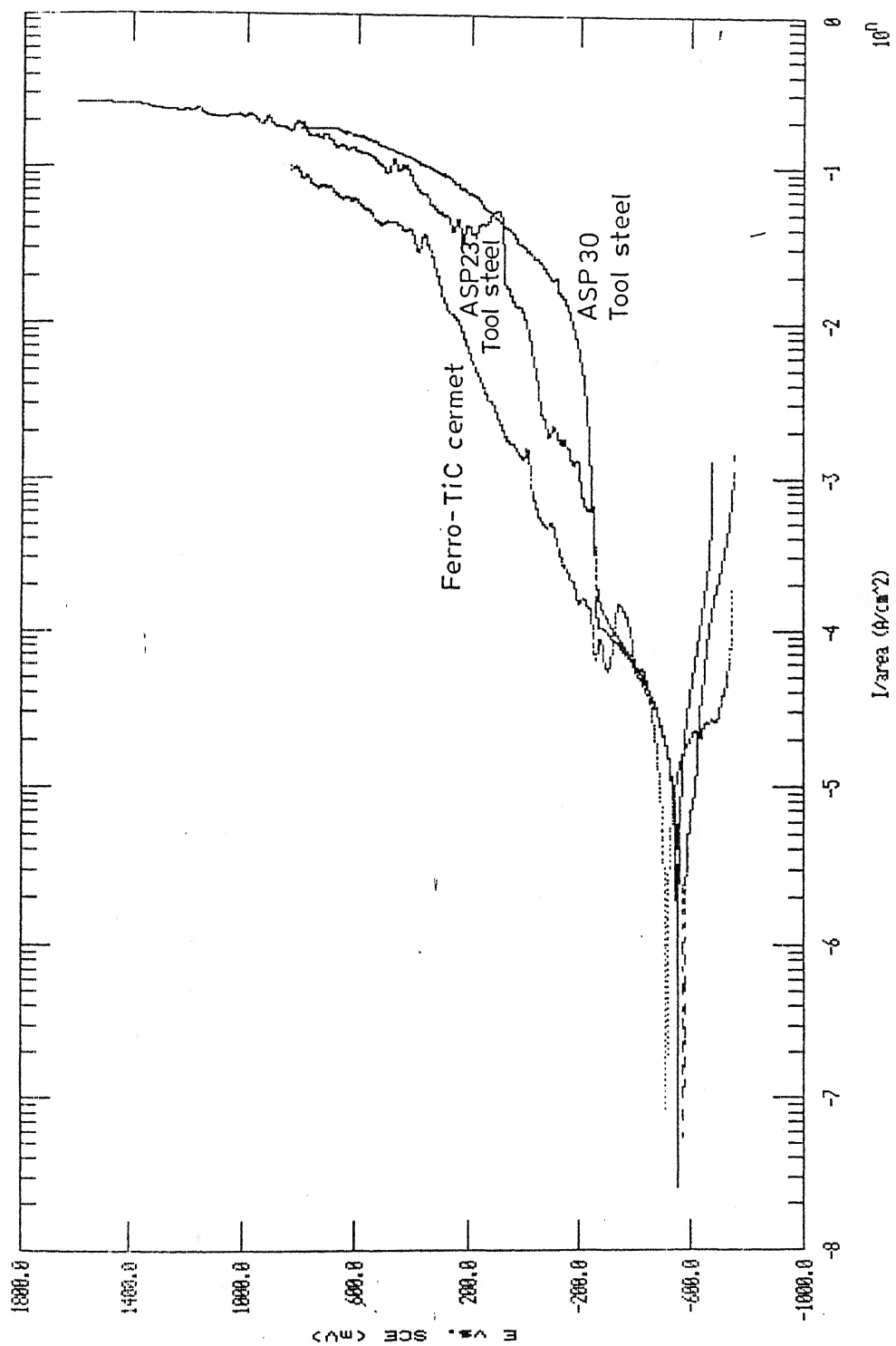


Figure 3.20 Anodic polarization curves of ASP 23 and ASP 30 tool steels along with Ferro-TiC in 0.6N NaCl solution.

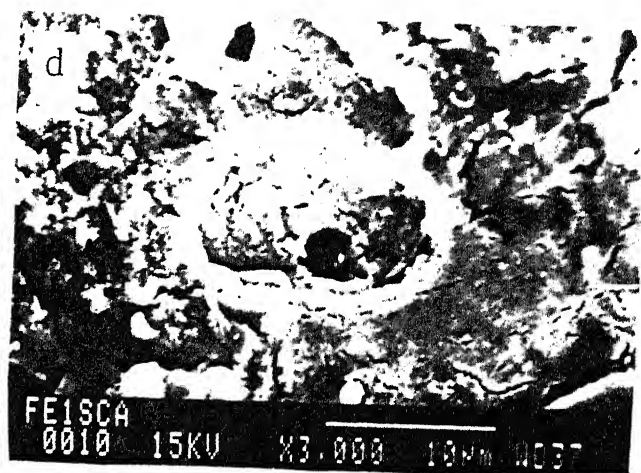
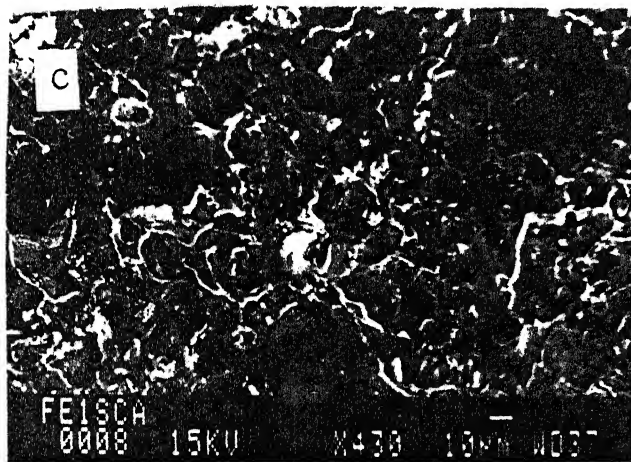
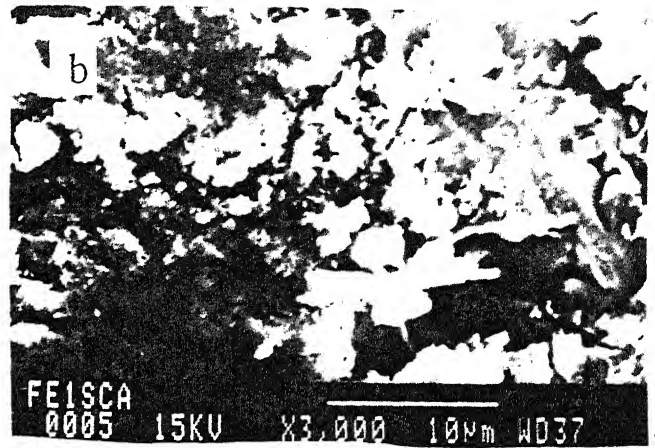
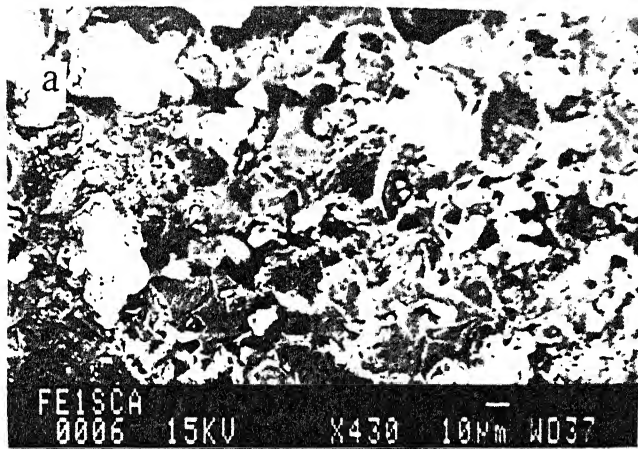


Figure 3.21 (cont...)

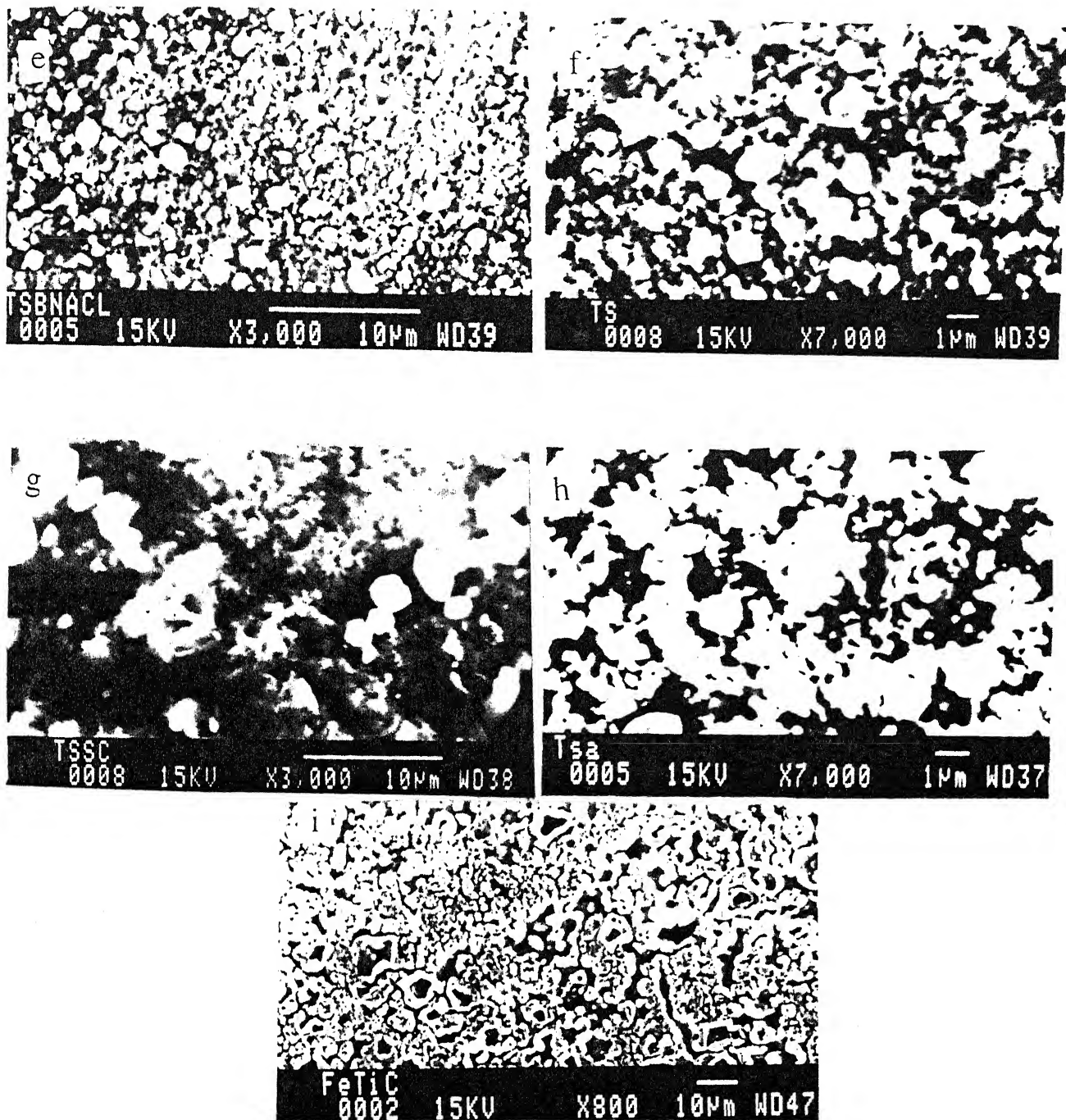


Figure 3.21 SEM micrographs of the corroded surfaces of various alloys tested in 0.6N NaCl solution:

- (a) – (b) Fe-0.5C at different magnifications
- (c) – (d) Fe-5Cu-0.5C at different magnifications
- (e) – (f) ASP 23 at different magnifications
- (g) – (h) ASP 30 at different magnifications
- (i) Ferro-TiC



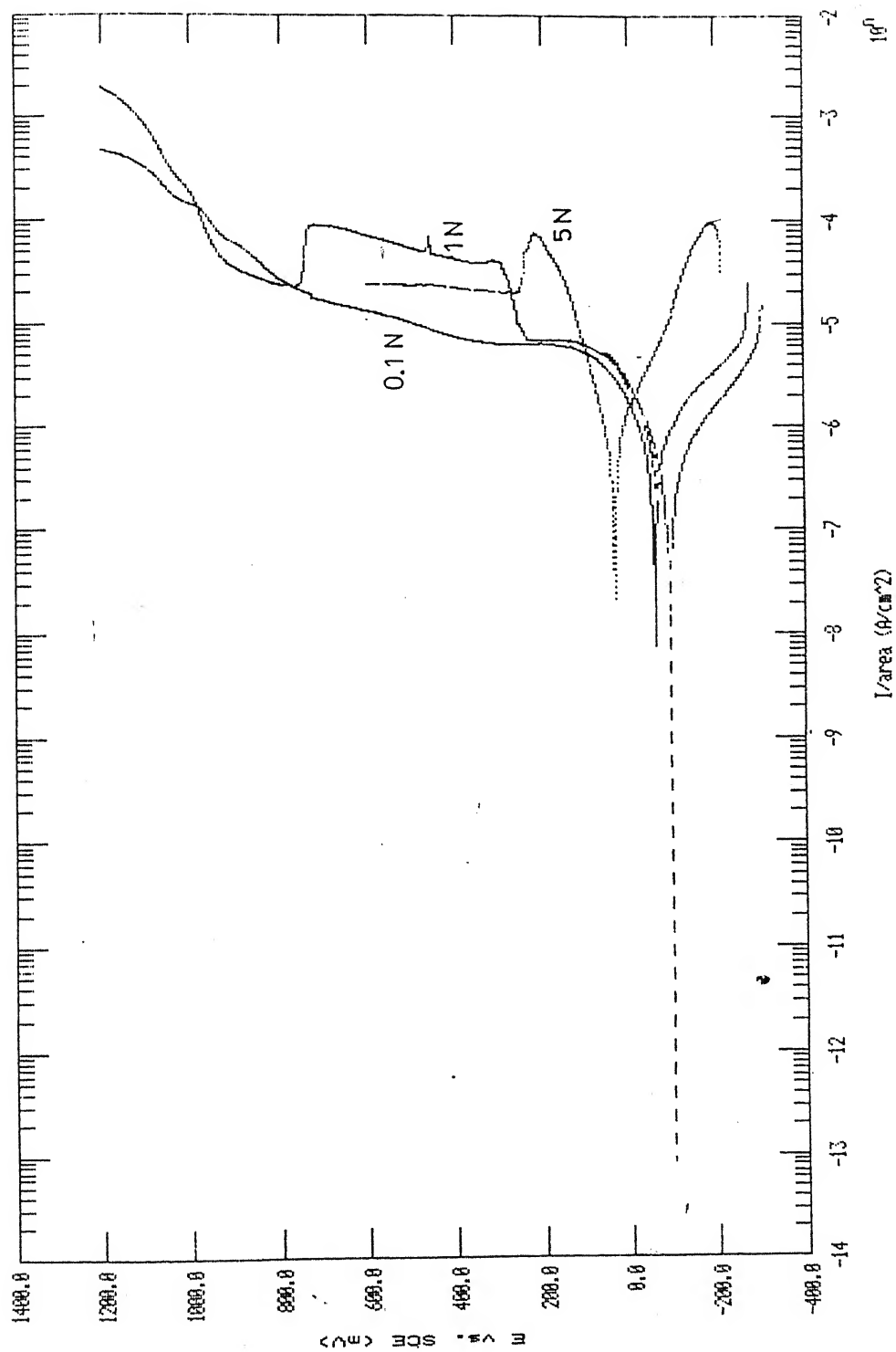


Figure 3.22 Some typical anodic polarization curves of Fe-base superalloy MA 956 in  $\text{H}_2\text{SO}_4$  of various concentrations.



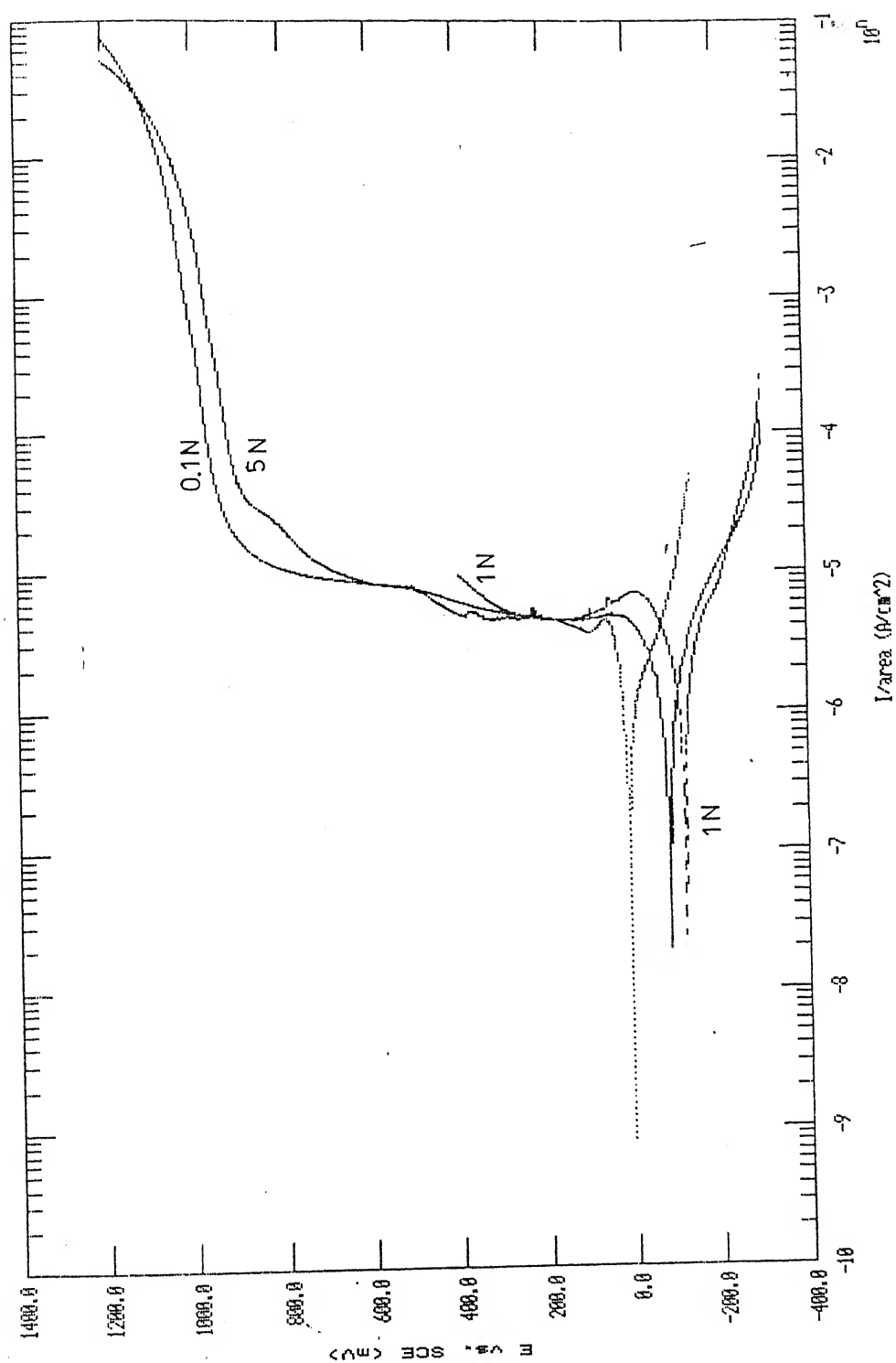


Figure 3.23 Some typical anodic polarization curves of Ni-base superalloy MA 754 in  $\text{H}_2\text{SO}_4$  of various concentrations.

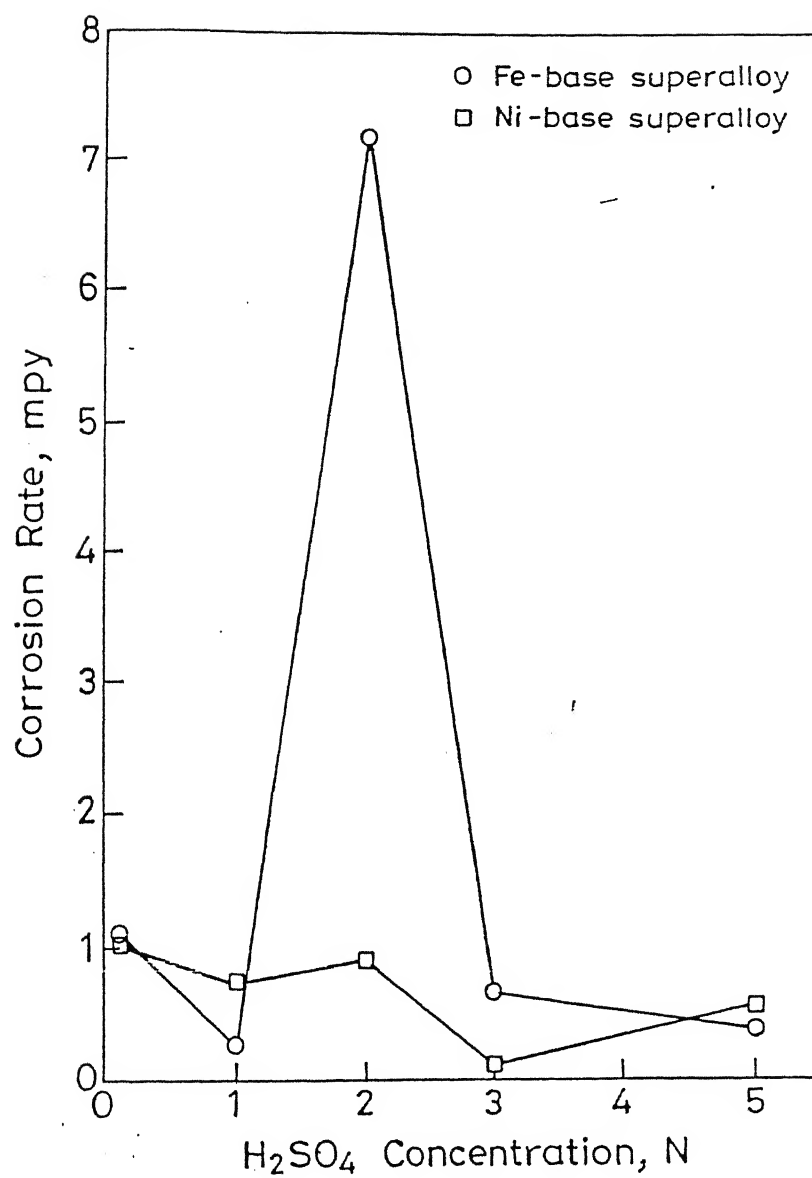


Figure 3.24 Corrosion rate variation of Fe- and Ni- base superalloys with respect to H<sub>2</sub>SO<sub>4</sub> concentration.

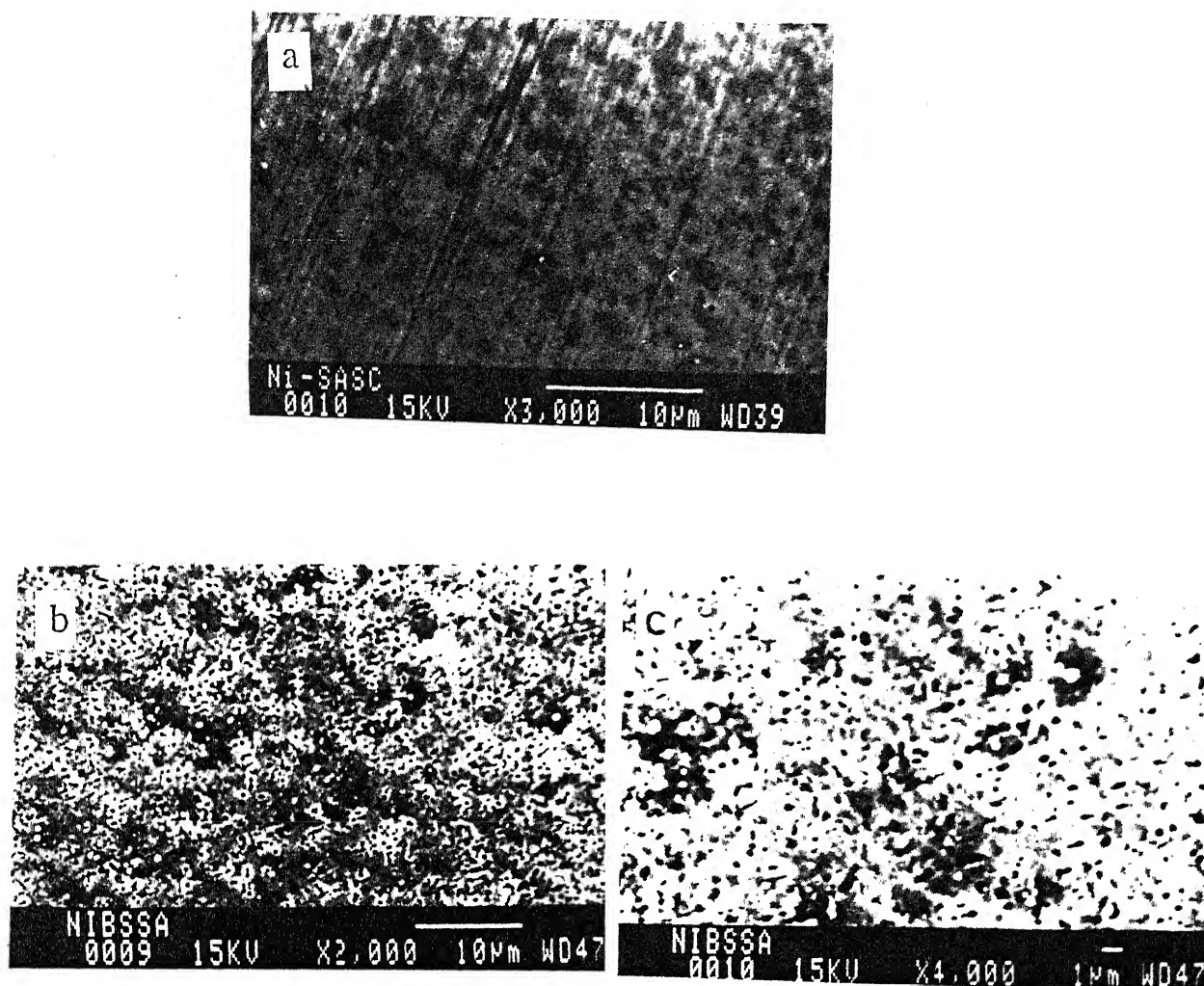


Figure 3.25 SEM micrographs of the corroded surfaces of both the superalloys tested in 2N  $\text{H}_2\text{SO}_4$ :

- (a) Fe-base superalloy MA956
- (b) – (c) Ni-base superalloy MA 754 at different magnifications

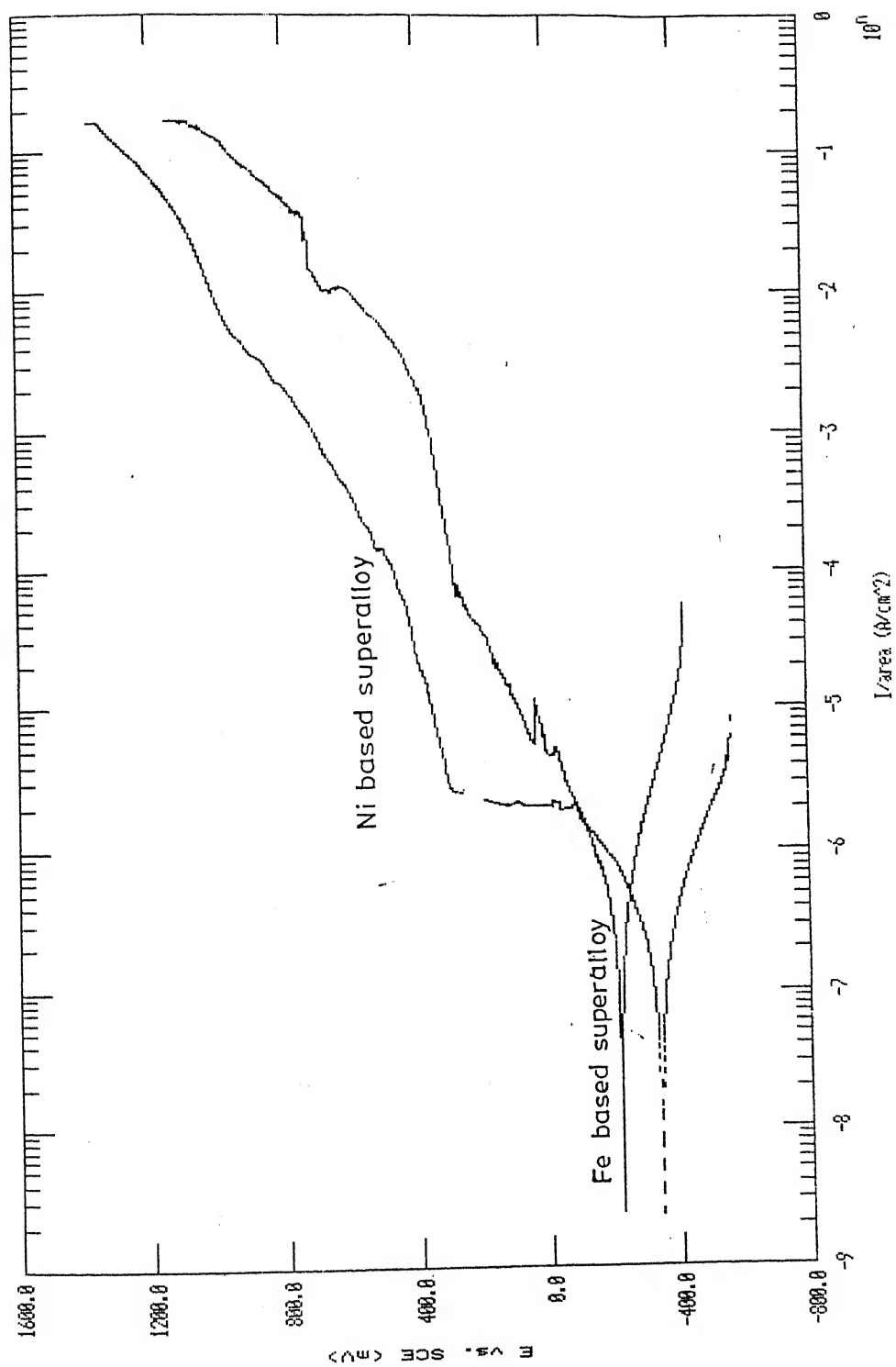


Figure 3.26 Anodic polarization curves of Fe- and Ni- base superalloys in 0.6N NaCl solution.

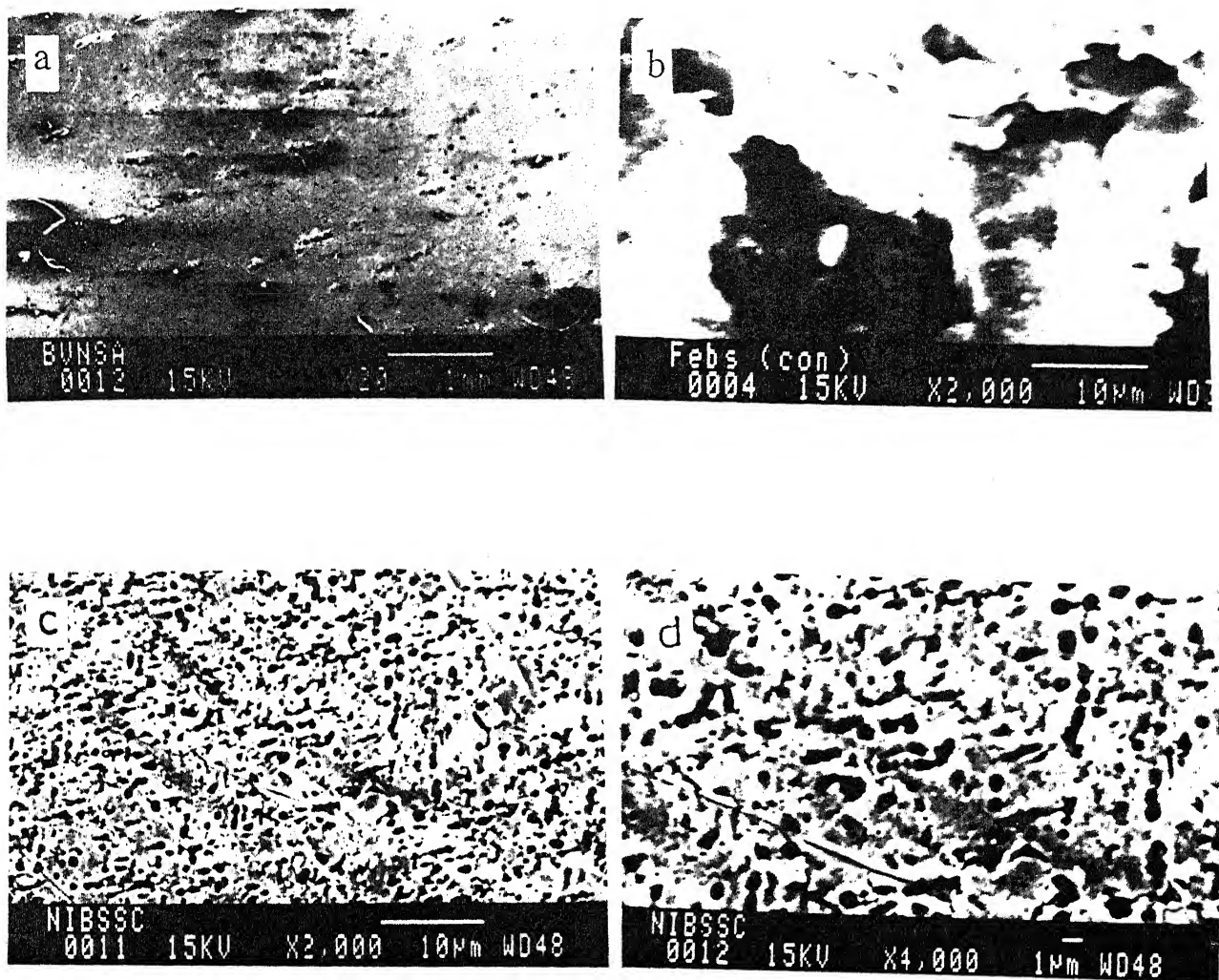


Figure 3.27 SEM micrographs of the corroded surfaces of both the superalloys tested in 0.6N NaCl solution:

- (a) –(b) Fe-base superalloy at different magnifications
- (c) –(d) Ni-base superalloy at different magnifications

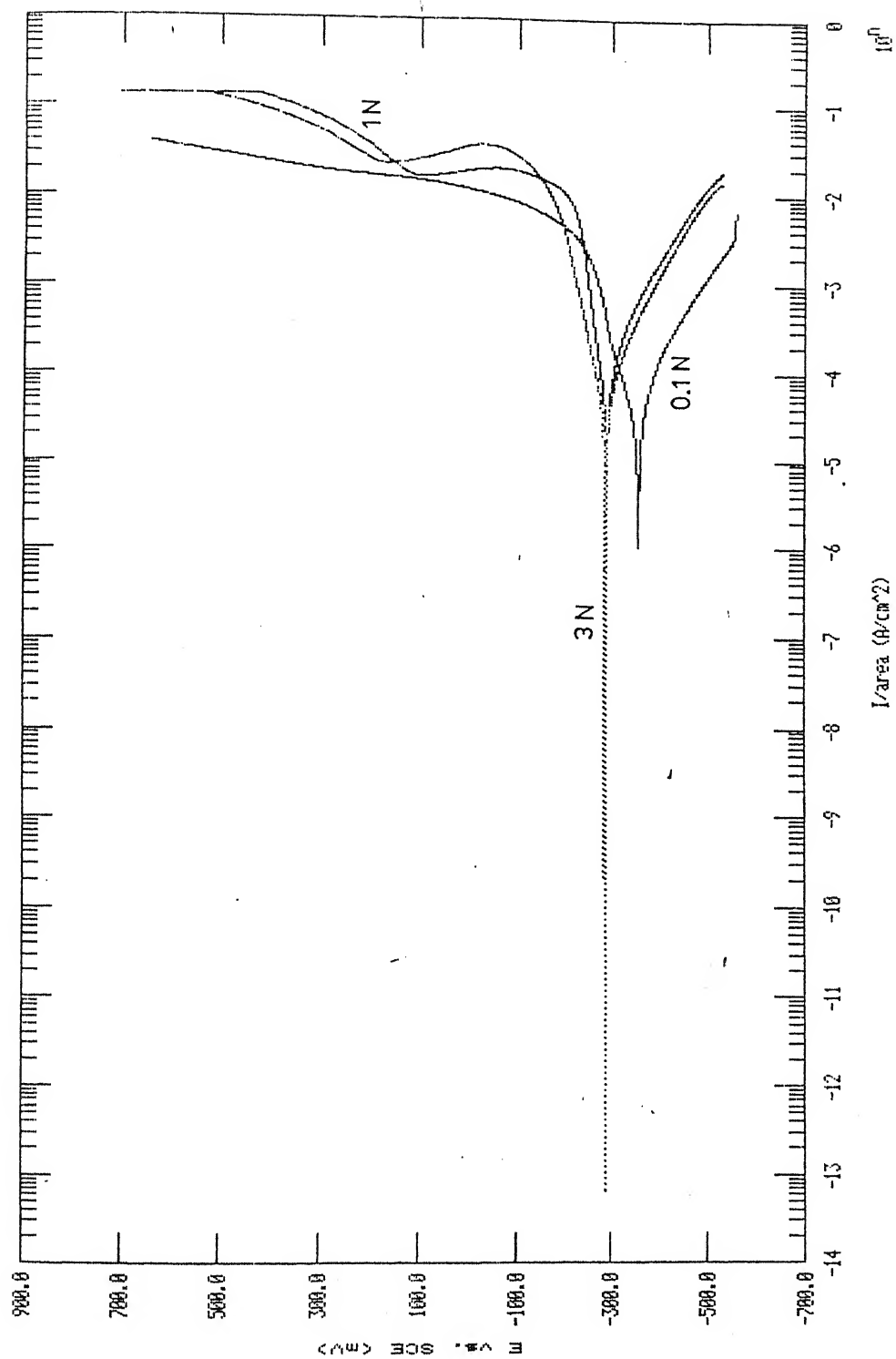


Figure 3.28 Anodic polarization curves for hydrogen sintered boride based cermet corresponding to different  $\text{H}_2\text{SO}_4$  concentrations.

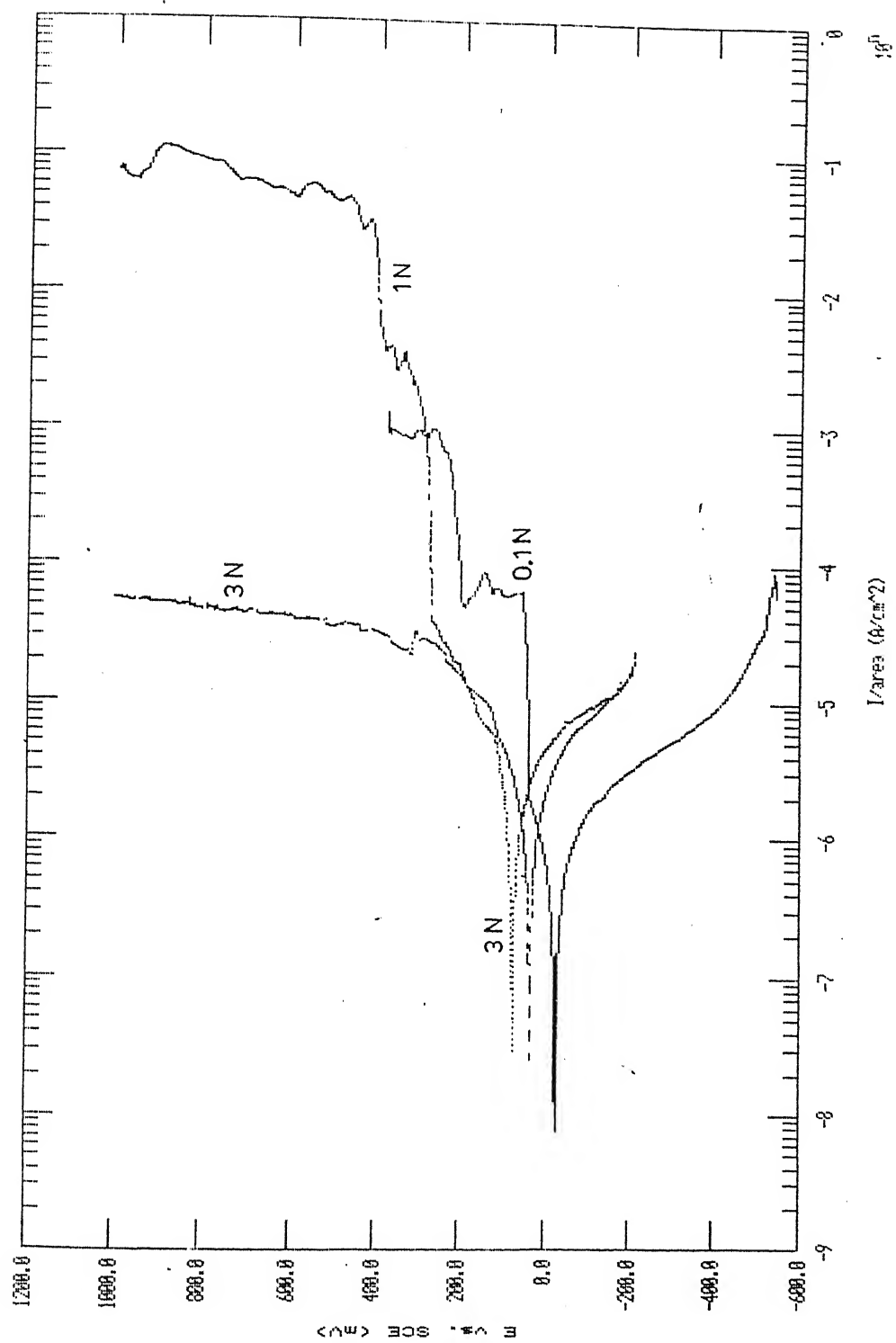


Figure 3.29 Anodic polarization curves for vacuum sintered boride based cermet corresponding to different  $\text{H}_2\text{SO}_4$  concentrations.

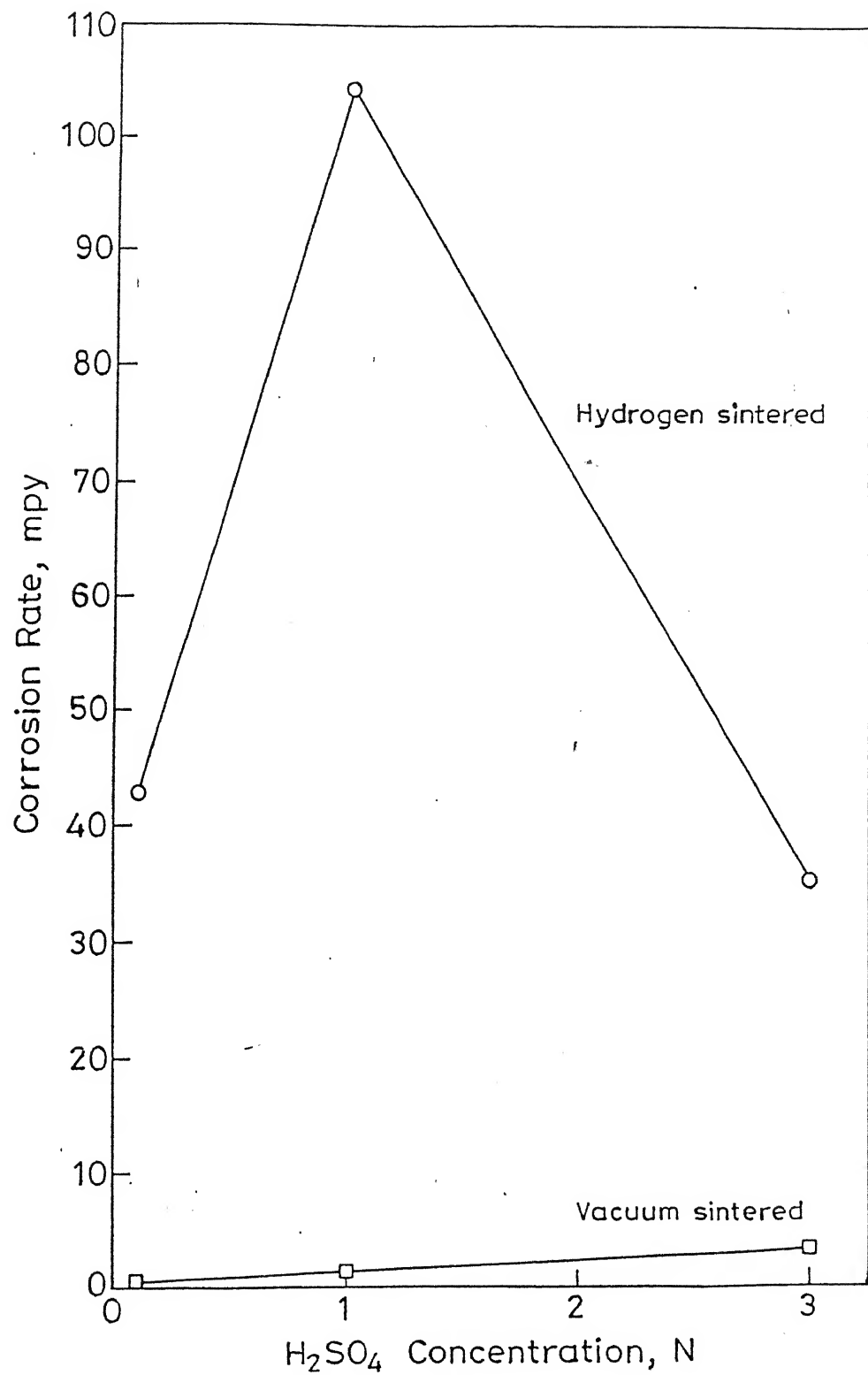


Figure 3.30 Corrosion rate variation of boride based cermets (sintered in hydrogen and vacuum respectively) with respect to  $H_2SO_4$  concentration.



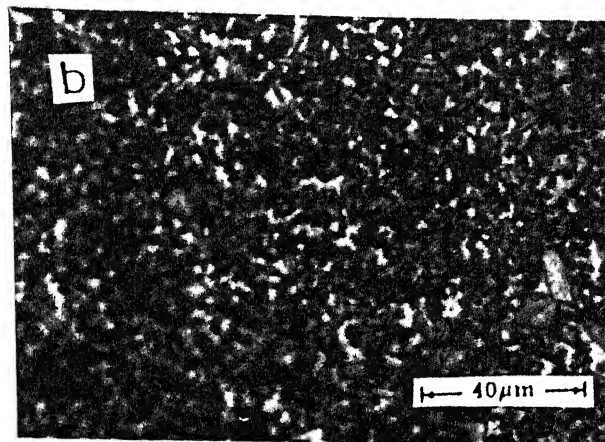
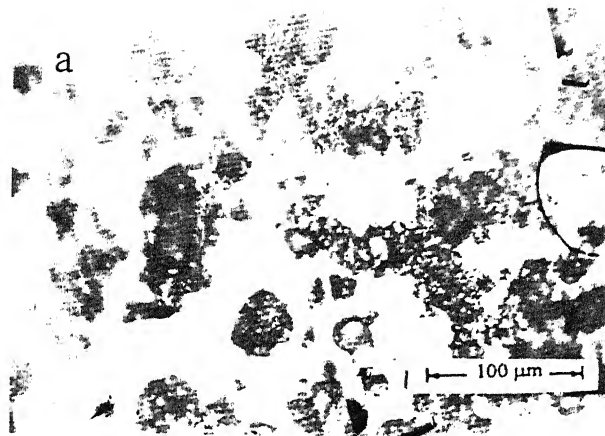


Figure 3.31 Optical micrographs of boride based cermets:

- (a) sintered in hydrogen (as-polished)
- (b) sintered in vacuum (as-etched)

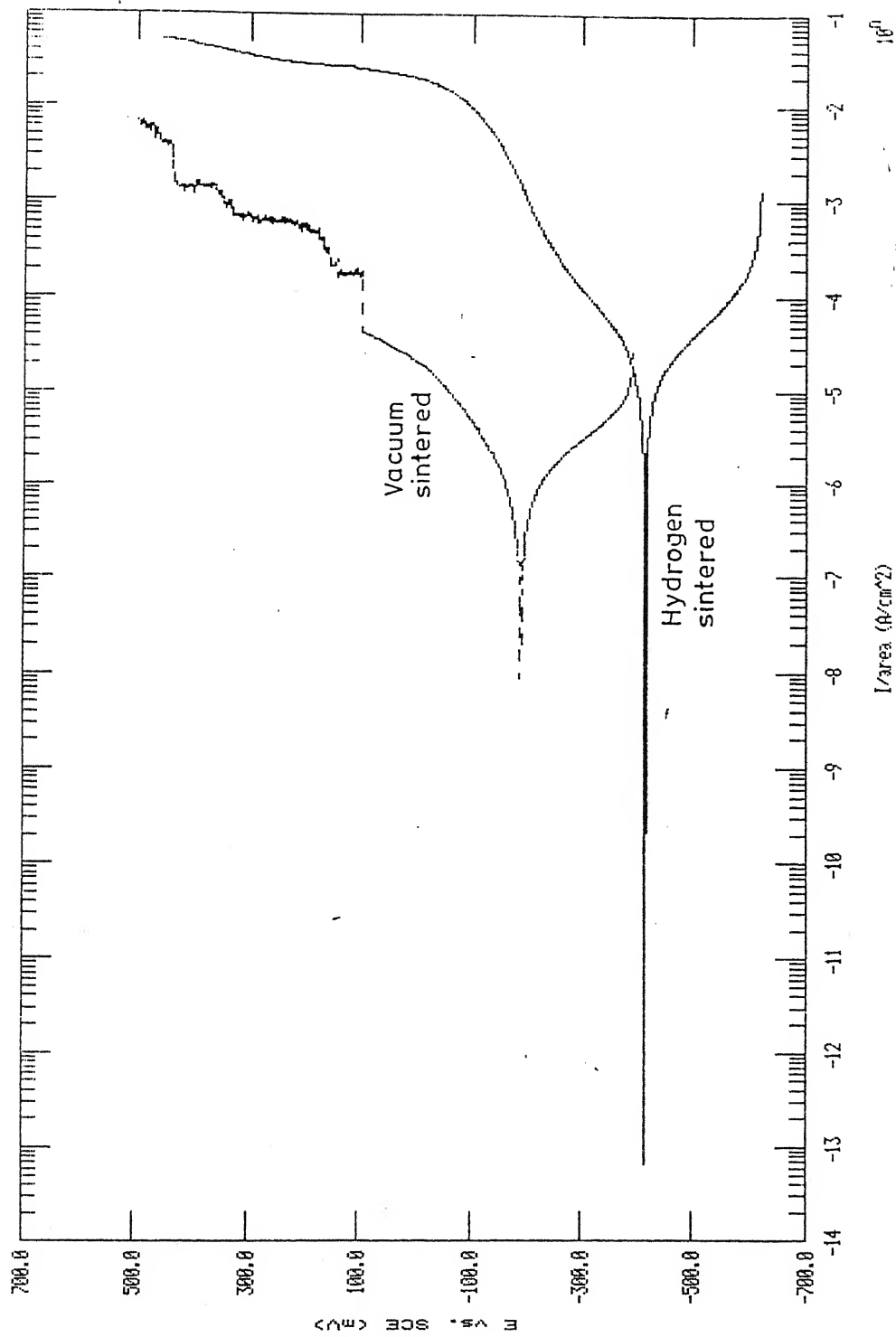


Figure 3.32 Anodic polarization of boride based cermets (sintered in hydrogen and vacuum respectively) in 0.6N NaCl solution.

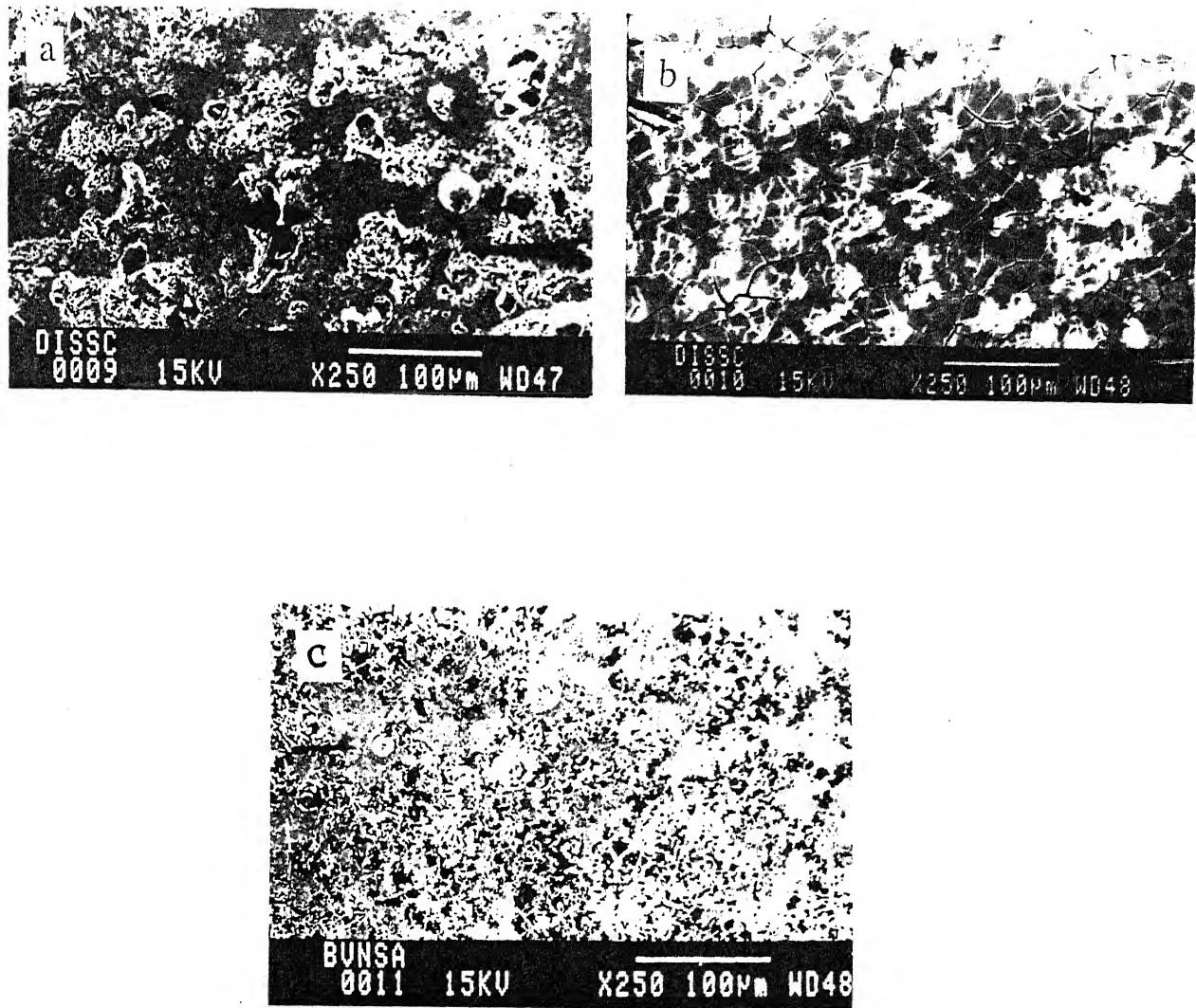


Figure 3.33 SEM micrographs of corroded surfaces of cermets sintered in different atmospheres:

(a)–(b) Hydrogen

(c) Vacuum

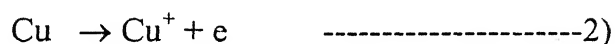
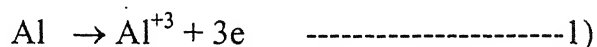
## Chapter – 4

### Discussion

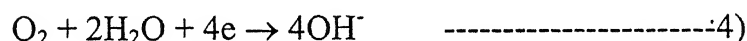
#### 4.1. Corrosion in H<sub>2</sub>SO<sub>4</sub> medium:

##### 4.1.1. Al- and Cu- based alloys:

The anodic reactions for aluminium and copper in H<sub>2</sub>SO<sub>4</sub> solution are:



However, cathodic reactions differ in each case. Reduction of oxygen to form hydroxide ions is the predominant cathodic reaction for copper and its alloys.



As the hydrogen ion is active, sulphate ion does not participate in the electrochemical reaction.

Literature [8] reports a linear behaviour in the wt. loss vs. H<sub>2</sub>SO<sub>4</sub> concentration for commercially purity aluminium within the concentration range of 40% (0 – 15N). However in the present case no linear curve was obtained within that concentration range. A comparison of two plots obtained for RS aluminium and DISPAL reveals that in most cases DISPAL shows

greater corrosion rates. This may be attributed to the alloying elements present in RS aluminium, which may modify the behaviour of the oxide. Also in all the selected concentrations the extended passive region is being maintained by RS aluminium. In the case of ODS copper, the corrosion rate is found to increase with concentration, but after 2N there is a decrease in the value. This may be due to the stability of the passive oxide layer formed on the surface.

The reason for obtaining the opposite trend in corrosion rate in 1(N) H<sub>2</sub>SO<sub>4</sub>, from wt. loss experiment is not clear.

#### 4.1.2. Ferrous alloys and Ferro-TiC:

The anodic reaction for all the alloys in H<sub>2</sub>SO<sub>4</sub> solution is



In most of the cases, iron goes into solution as divalent iron which is oxidized to the trivalent state by atmospheric oxygen. Hydrogen evolution (given in equation 3) is the cathodic reaction.

Literature [19] reports a linear behaviour in corrosion rate vs. H<sub>2</sub>SO<sub>4</sub> concentration of iron within the concentration range of 25% (0 – 9.5N). Similar results were obtained for ASP 30 and ASP 23 steels. The curves for the rest of the alloys are found to show irregular trends. The effect on corrosion rate with respect to H<sub>2</sub>SO<sub>4</sub> concentration does not follow a uniform pattern – first because of ionization effects in the aqueous solution and second, because of changes that occur in the characteristics of any film of the corrosion products that may be present on the alloy surfaces.

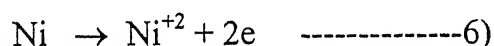
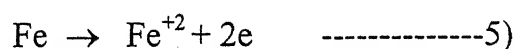
Literatures [20,21] report the beneficial effect of Cu in reducing the corrosion rates of steels in H<sub>2</sub>SO<sub>4</sub>. However, the present investigation shows

that Fe-5Cu-0.5C steel is less corrosion resistant as compared to Fe-0.5C. This may be due to the more heterogeneous microstructure for the former (Figure 3.17(b)). In addition, the lattice distortion with dissolution of Cu in the ferrous matrix also is responsible for more corrosion. As far as porosity in these steels is concerned, the values are more or less equal for both the steels (Table 2.2). This confirms that the present change in corrosion behaviour is not dictated by the variation in porosities. 8.5 wt. % of Co in ASP-30 steel appears to be responsible for more corrosion resistance compared to ASP 23.

In case of Ferro-TiC cermet, there is much irregularity in the corrosion rate variation. The abnormal value at 2N is not clear. However, the higher corrosion rates obtained may be attributed to a greater attack of the solution on the binder phase, i.e. steel.

### 4.1.3. Superalloys:

The anodic reactions involving iron and nickel in H<sub>2</sub>SO<sub>4</sub> solution are:



The cathodic reaction in both the cases is the hydrogen ion reduction (equation 3). The effect of increasing the concentration of H<sub>2</sub>SO<sub>4</sub> on corrosion rate does not follow a uniform pattern, first because of ionization effects in the aqueous solution and second, because of changes that occur in characteristics of corrosion products film present on the surface of the metal. Literature [19] reports a linear behaviour in corrosion rate vs. H<sub>2</sub>SO<sub>4</sub> concentration of iron within the concentration range of 25% (0 – 9.5N). However in the present case

no such linear curve within that range was obtained. The plot obtained for MA 754 was also non-linear.

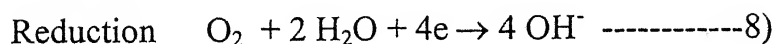
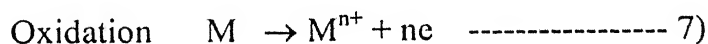
Chromium improves the passivity of both the alloys, which is quite evident from Figure 3.22 and 3.23. Transpassive regions are clearly seen in the curves obtained for nickel- base superalloy. In case of iron-base superalloy, the presence of pre-passive state in 5N H<sub>2</sub>SO<sub>4</sub> solution is supported by the results of Modi [35].

#### 4.1.4. Boride based cermets:

The reason for a sudden decrease in corrosion rate values in case of 3N H<sub>2</sub>SO<sub>4</sub> solution for cermet sintered in hydrogen is not clear. Higher corrosion rate for the cermet sintered in hydrogen as compared to the cermet sintered in vacuum is predominantly due to the higher porosity present in the former. The presence of porosity drifts the corrosion potential value to more active region, thus favouring severe attack by the corrosion medium.

#### 4.2. Corrosion in 0.6N NaCl solution:

The basic mechanism of the corrosion process which takes place on the metal/alloy surface in aerated seawater, can be illustrated by the following reactions:



The detailed mechanism of crevice corrosion and pitting corrosion is given elsewhere [ 31].

### 4.2.1. Al- and Cu- based alloys:

Yoshika *et al.* [14] found that the extension of the solid solubility through rapid solidification is beneficial in improving the pitting corrosion resistance of aluminium, which is being reflected in the present case.

The present results show a greater corrosion rate for DISPAL as compared to RS aluminium. This is in good agreement with the results obtained by Shaw [15]. In fact, the high corrosion rate of DISPAL combined with active pitting makes it undesirable, when used in salt environments.

An essential feature of the behaviour of copper and its alloys in marine environments is the development of a protective film of cuprous oxide. In seawater, copper alloys behave differently from that of aluminium. The lesser corrosion rate of ODS copper as compared to DISPAL is due to the extended passivity in the former case, which is evident from anodic polarization curves (Figure 3.8). It is also note worthy that the dispersoid size here is much more finer than in case of ODS copper. In addition the volume fraction s of dispersoids are more in case of DISPAL. However the greater corrosion rate of ODS copper as compared to RS aluminium is related to the fact that it is a two phase composite, while RS aluminium has rather small volume fraction of precipitates.

### 4.2.2. Ferrous alloys and Ferro-TiC:

Relatively very high values of corrosion rates for Fe-0.5C and Fe-5Cu-0.5C steels are attributed to the porosity level present in them. In the presence of aggressive  $\text{Cl}^-$  ions, there is a breakdown of the passive film that is formed on the surface. This is evident from Figure 3.19 and 3.20. ASP 23 and ASP 30 steels owe their corrosion resistance to the maintenance of the passive film.



The higher corrosion rate of Ferro-TiC is obviously due to the greater attack of the binder phase by NaCl solution.

#### **4.2.3. Superalloys:**

Pitting corrosion occurs usually on those metals and alloys which show active to passive transition characteristics. In other words, metals which owe their corrosion resistance to the presence of thin and passive surface films may be susceptible to pitting attack when the surface film breaks down locally and does not reform. In a chloride environment nickel is less susceptible for pitting than iron [24]. From Fig-4 this feature is confirmed. A corrosion pit is a unique type of anodic reaction and the pits cathodically protect the rest of the alloy surface.

#### **4.2.4. Boride based cermets:**

Like  $H_2SO_4$  solution, the greater corrosion attack in NaCl solution for cermet sintered in hydrogen as compared to one sintered in vacuum is attributed to the porosity present in the former. Due to this the corrosion potential falls in the active region.

## Chapter – 5

### Conclusions

Following conclusions can be drawn from the present investigation.

1. Rapidly solidified 7091 powder metallurgy aluminium alloy is superior to Dispersion strengthened aluminium alloy with respect to corrosion resistance in  $\text{H}_2\text{SO}_4$  and NaCl media.
2. Dispersion strengthened copper is more corrosion resistant than Dispersion strengthened aluminium in  $\text{H}_2\text{SO}_4$  (only for concentrations  $> 2\text{N}$ ) and  $0.6\text{N}$  NaCl solutions.
3. The extension of the solid solubility through rapid solidification is beneficial in improving the pitting corrosion resistance of aluminium.
4. Porosity plays a vital role in determining the corrosion behaviour of sintered alloys.
5. Both  $\text{H}_2\text{SO}_4$  and NaCl media more rapidly attack Fe-5Cu-0.5C sintered steel than Fe-0.5C steel. This is due to the more heterogeneous microstructure in the former.
6. ASP 30 tool steel is more corrosion resistant as compared to ASP 23 tool steel in both  $\text{H}_2\text{SO}_4$  and NaCl media.

7. The sudden increase in corrosion rate of Ferro-TiC after certain  $\text{H}_2\text{SO}_4$  concentration may be attributed to the binder phase.
8. In the case of 0.6N NaCl solution, Ferro-TiC is in between low alloy steel and tool steel in its corrosion behaviour.
9. In general, the superalloys investigated have good corrosion resistance in both  $\text{H}_2\text{SO}_4$  and NaCl solutions.
10. No regular trend in the behaviour of corrosion rate with respect to concentration of  $\text{H}_2\text{SO}_4$  is obtained, particularly for iron-base superalloy, MA 956.
11. Nickel-base superalloy MA 754 is more corrosion resistant than Iron-base superalloy MA 956 in 0.6N NaCl solution.
12. The ternary Molybdenum based cermet sintered in hydrogen is found to be more prone to corrosion attack by  $\text{H}_2\text{SO}_4$  and NaCl media as compared to the vacuum sintered cermet.

## References

1. E.F. Bradley, "Superalloys; A Technical Guide", ASM International<sup>TM</sup>, Materials Park, Ohio, USA, 1988, p. 143.
2. G. S. Upadhyaya, "Sintered Metallic and Ceramic Materials – Preparations, Properties, and Applications", John Wiley and Sons Ltd., Chichester, UK, 1999.
3. Model 352 SoftCorr<sup>TM</sup> II, Corrosion Measurement & Analysis Software, User's Guide, EG & G Instruments Corporation, Princeton, USA, 1991, p. 118.
4. J.R. Davis (Sr. Editor), "Laboratory Testing", in "Corrosion Handbook", 9<sup>th</sup> ed., ASM International, Materials Park, Ohio, USA, vol-13, 1987, p. 213.
5. G. Jangg, F. Kutner and G. Korb, "Dispersion hardening of aluminium with  $Al_4C_3$ ", Powder Metallurgy International, vol-9, No.1, 1977, p. 24-26.
6. P.K. Samal and A.V. Nadkarni, "Recent advances in dispersion strengthened copper base materials", in Modern Developments in Powder Metallurgy, vol-16, Metal Powder Industries Federation and American Powder Metallurgy Institute, Princeton, New Jersey, 1984, p. 341-360.
7. A.V. Nadkarni, E. Klar and W.M. Shafer, "A new dispersion strengthened copper", Met. Eng. Q., August 1976, p. 10.
8. L.L. Shreir, "Aluminium and Aluminium alloys", in "Corrosion", vol-1, 2<sup>nd</sup> ed., The Butterworth Group, London, 1976, p. 4:24.
9. A.P. Haarr, "Development of Aluminium Base Alloys", 3<sup>rd</sup> annual Report, No. 13-64-AP59S, Contract DA-36-034-ORD-3559RD, October 1994.

10. J.P. Lyle and W.S. Cebulak, "Powder Metallurgy Approach for control of microstructure and Properties in High Strength Aluminium alloys", Met- Trans., 6A, 1975, p. 685.
11. J.P. Lyle and W.S. Cebulak, in "Proceedings of 18<sup>th</sup> Sagamore Army Materials and Research Conference on P/M for High Performance", Eds. J. Burke and V. Weiss, Syracuse University press, Syracuse, NY, 1972, p. 231.
12. J.P. Lyle and V. Weiss, Met. Eng. Q., 14, 1974, p. 52.
13. W.L. Otto, "Metallurgical factors controlling structure in high strength P/M products", Final Technical Report AFML-TR-76-60, Contract F33615-74-C-5077, May 1974.
14. H. Yoshioka, S. Yoshida, A. Kawashima, K. Asami and K. Hashimoto, "The Pitting Corrosion Behavior of Rapidly Solidified Aluminium Alloys", Corros. Sci. 26, 1986, p. 795.
15. W.J.D. Shaw, "Surface corrosion comparisons of some Aluminium alloys in 3.5% NaCl solution", in "Corrosion, microstructure, & metallography", Proceedings of the Sixteenth Annual Technical Meeting of International Metallographic Society, Edited by Derak O. Northwood, William E. White and George F. Vandervoort, The International Metallographic Society, Columbus, and American Society for Materials, Materials Park, Ohio, USA, 1985, p. 245.
16. K. Majima, and H. Mitani, "Sintering mechanism in mixed powder compacts of the Fe-Cu-C Ternary system", Transactions JIM, 18, 1977, p. 663.
17. Ranjan, "Effect of copper and VCN addition on sintering of low alloy steel", M.Tech. Thesis, Indian Institute of Technology, Kanpur, May, 2000.
18. P. Hellman, H. Larker, J.B. Pfeffer and I. Stromblad, "The ASEA-Stora process", in Modern Developments in Powder Metallurgy, vol-4, Plenum Press, New York, 1970, p. 573-582.

19. R. Ward, "Corrosion failures", in Metals Handbook, "Failure analysis and prevention", vol-10, 8<sup>th</sup> Edn., ASM International, Materials Park, Ohio, USA, 1975, p. 168.
20. H. Endo and S. Morioka, "Dissolution Phenomenon of Copper containing Steels in Aqueous Sulfuric acid solutions of various concentrations", paper presented at the third symposium, Japanese Metal Association, April 1938.
21. E. Williams and M.E. Komp, Corrosion, vol-21 (No-1), Jan 1965, p. 9-14.
22. J. Nutting, S. Ubhi and T.A. Hughes, in "Frontiers of High Temperature Materials", Ed. J.S. Benjamin, Inco MAP, New York, 1981, p. 33.
23. J.S. Benjamin, "Dispersion Strengthened Superalloys by Mechanical Alloying", Met-Trans., vol-1, 1970, p. 2943.
24. J.B. Lumsden, "Localized corrosion", in "Corrosion of Nickel-base alloys", Conference proceedings of the International Conference on Corrosion of Nickel-base Alloys, 23-25 October 1984, Cincinnati, Ohio, American Society for Metals, 1985, p. 183.
25. K. Takagi, Proceedings P/M 94, vol.1, Les Editions de Physique, Les Ulis, France, 1994, p. 227.
26. Dhaval Rao, "Sinter Bonding of Mo<sub>2</sub>FeB<sub>2</sub> Based Cermet onto Steel Substrate and Sintering of Boride Cermet-SiC Fiber Composites", M.Tech. Thesis, Indian Institute of Technology, Kanpur, India, May, 2000.
27. K. Takagi, M. Komai, T. Ide, T. Watanabe, and Y. Kondo, "Effect of Ni on the mechanical properties of Fe, Mo, Boride hard alloys", International Journal of Powder Metallurgy, 23, No-3, 1987, p. 157.
28. M. Komai, K. Takagi, T. Watanabe, and Y. Kondo, "Corrosion behavior of sintered Mo<sub>2</sub>FeB<sub>2</sub> base hard alloys", Material Research Society International Meeting on Advanced Materials, vol- 4, Materials Research Society, Pittsburgh, 1989, p. 475-479.

29. K. Takagi, M. Komai, T. Ide, T. Watanabe, and Y. Kondo, "Effects of Mo and Cr contents on the properties and phase formation of Iron Molybdenum Boride Base Hard Alloys", Powder Metallurgy International, 19, No-5, 1987, p. 30.
30. R.M. German, " Powder Metallurgy Science", 2<sup>nd</sup> ed., MPIF, Princeton, New Jersey, USA, 1994, p. 385.
31. M.G. Fontana, " Corrosion Engineering", 3<sup>rd</sup> ed., Mc Graw-Hill, New York, 1986.
32. K. Takagi, S. Ohira, T. Ide, T. Watanabe, and Y. Kondo, "New multiple boride based hard alloys", Modern Developments in Powder Metallurgy, vol. 16, Edited by E.N. Aqua and C.I. Whitman, Metal Powder Industry Federation, Princeton, 1985, p. 153-166.
33. B. D. Cullity, "Elements of X-ray diffraction", 2<sup>nd</sup> edition, Addison-Wesley Publishing, inc, Massachusetts, 1978.
34. M. Singh, " TiB<sub>2</sub> based sintered porous cermets", M.Tech. Thesis, Indian Institute of Technology, Kanpur, May, 1999.
35. O.P. Modi, "Potentiodynamic Study of Chromium-Molybdenum Ferritic Steels in Sulphuric acid and Seawater", M.Tech. Thesis, Indian Institute of Technology, Kanpur, August, 1983.

A-133079

A-133079  
Date Slip

The book is to be returned on  
the date last stamped.




A133079